Monitoring and Predicting Railway Subsidence Using InSAR and Time Series Prediction Techniques

ZIYI YANG

A thesis submitted to

The University of Birmingham

for the degree of

DOCTOR OF PHILOSOPHY

School of Civil Engineering

College of Engineering and Physical Sciences

The University of Birmingham, UK

March 2015

Abstract

Improvements in railway capabilities have resulted in heavier axle loads and higher speed operations. Both of these factors increase the dynamic loads on the track. As a result, railway subsidence has become a threat to good railway performance and safe railway operation. Poor infrastructure performance requires more maintenance work, and therefore the life cycle costs of the railway will increase. In order to ensure good performance and reduce life cycle costs, railway subsidence should be monitored and predicted. The author of this thesis provides an approach for railway performance assessment through the monitoring of railway subsidence and prediction of railway subsidence based on a time series of Synthetic Aperture Radar (SAR) images.

The railway is a long and relatively narrow infrastructure, which subsides continuously over a long time period. As a result, larger image coverage and long time monitoring periods are two key requirements for railway subsidence monitoring. In addition, railway subsidence monitoring should also consider the repeatability, precision and efficiency of the monitoring method, as well as labour costs. The Interferometric Synthetic Aperture Radar (InSAR) technique, which is able to monitor railway subsidence over a large area and long time period, was selected for railway subsidence monitoring by the author. In order to obtain a more reliable railway subsidence measurement result, and extension of InSAR, PS-InSAR (Permanent Scatterer InSAR), was used for the research, since it is capable of supporting a time series analysis of ground deformation. In addition to railway subsidence monitoring, future trends of railway subsidence should also be predicted using subsidence prediction models. Railway deformation records obtained by PS-InSAR can be considered as a discrete time series. As a result, three time series prediction models have been investigated in this thesis for railway subsidence prediction, which are the traditional statistical ARMA model, a neural network model based on artificial intelligence and the grey model.

Case studies to monitor and predict the subsidence of ground under the High Speed One (HS1) route in Britain were carried out to assess the performance of the PS-InSAR method and the time series prediction models. A deformation profile of HS1

has been developed for the case study, based on deformation monitoring results obtained by PS-InSAR. The deformation profile demonstrates that no large scale subsidence has occurred on HS1 and the line is still stable after having been in operation for 10 years. However, some areas of HS1 show potential subsidence. For instance, the areas over the North Downs Tunnel and the line between Hockers Lane Overbridge and Water Lane Underbridge have subsided by up to 4.0 mm per year and 2.9 mm per year respectively. The stability of the ground under Ashford International Station was also assessed in this thesis. Based on the deformation monitoring records of HS1, railway subsidence prediction was carried out by the application of three main time series prediction models. The result of the railway prediction demonstrates that the neural network model has the best performance in predicting the subsidence of HS1.

Acknowledgements

Foremost, I would like to express my gratitude to my supervisors, Prof. Felix Schmid and Prof. Clive Roberts for their patience, motivation, knowledge, support and encouragement in my PhD study. Without their supervision, I could not overcome difficulties in my research and thesis writing up.

Besides my supervisors, I am grateful to David Oldroyd for his support in my research, particularly in the information gathering for the case study. I also appreciate the help of Katherine Slater.

I would like to thank Prof. Andy Hooper from Leeds University for providing StaMPS software for my data processing, Delft University of Technology for providing precise radar orbit data, USGS for providing SRTM data and ESA for providing Envisat ASAR data.

Moreover, I appreciate the great support and encouragement from my husband Gang Hu and my parents during my studies at the University of Birmingham. In addition, I am grateful to all the people who helped me and encouraged me during my PhD at the University of Birmingham.

Table of Contents

Table of Contents ..... **v**
List of Figures ..... **ix**
List of Tables ..... **xi**
List of Abbreviations ..... **xii**
Chapter 1 Introduction **1**
1.1 Background 1
1.2 Objectives 3
1.3 Thesis Structure 4
Chapter 2 Review of Railway Subsidence Monitoring **7**
2.1 Introduction 7
2.2 Nature of Railway Infrastructure and Subsidence 7
2.3 Approaches for Railway Subsidence Monitoring 9
2.4 Development of InSAR 10
2.5 Acquisition of SAR Image 12
2.5.1 Designation of Radar Band 12
2.5.2 Image Acquisition Modes 14
2.5.3 Satellites for Image Acquisition 17
2.6 Applications of InSAR 18
2.6.1 Topography Mapping 18
2.6.2 DEM Generation 19
2.6.3 Ocean Currents Mapping 20
2.6.4 Landscape Deformation Measurement 20
2.7 Ground Deformation Monitoring by D-InSAR 21
2.7.1 Classifications of D-InSAR 22
2.7.2 Limitations of D-InSAR 23
2.8 Ground Deformation Monitoring by PS-InSAR 26
2.9 PS-InSAR in Railway Subsidence Monitoring 27
2.9.1 SNCF High Speed Rail Network 27
2.9.2 Jubilee Extension Line in London 27
2.9.3 Jinshan Railway in China 28

2.10 Summary 29
Chapter 3 Review of Railway Subsidence Prediction 31
3.1 Introduction 31
3.2 Time Series Prediction Model 31
3.2.1 Statistical Models 32
3.2.2 Artificial Neural Network 37
3.2.3 Grey Model 38
3.2.4 Comparisons between Time Series Prediction Models 39
3.3 Time Series Models in Subsidence Prediction 41
3.3.1 ARMA Models 41
3.3.2 Artificial Neural Network 41
3.3.3 Grey Theory based Prediction 43
3.4 Summary 44
Chapter 4 Railway Subsidence Monitoring with InSAR 45
4.1 Introduction 45
4.2 Real Aperture Radar 45
4.2.1 Principle of Real Aperture Radar Operation 45
4.2.2 Resolution of Radar Image 46
4.3 Synthetic Aperture Radar 50
4.4 DEM Generation by InSAR 51
4.4.1 Principle 52
4.4.2 Phase Difference 53
4.4.3 DEM generation 55
4.5 Ground Deformation Monitoring by D-InSAR 56
4.5.1 Principle 56
4.5.2 Conditions for a Robust Result 57
4.5.3 Procedure for Ground Deformation Monitoring 58
4.6 Ground Deformation Monitoring by PS-InSAR 66
4.6.1 Selection of Master Image 66
4.6.2 Interferogram Generation 67
4.6.3 Phase Noise Estimation 67
4.6.4 Selection of the Persistent Scatterer 69

4.6.5 Dem Error Correction and Phase Unwrapping 71
4.6.6 Phase Filtering for Spatially Correlated Error 72
4.6.7 Extraction of Ground Subsidence 73
4.7 Summary 73
Chapter 5 Railway Subsidence Prediction with Time Series Prediction Models 74
5.1 Introduction 74
5.2 Railway Subsidence Prediction Models 75
5.2.1 ARIMA (p,d,q) Model 75
5.2.2 Artificial Neural Network Model 80
5.2.3 Grey Model 85
5.3 Summary 88
Chapter 6 Railway Subsidence Monitoring Case Study 90
6.1 Introduction 90
6.2 Route Configuration 90
6.3 Data Collection 92
6.3.1 Data Availability 92
6.3.2 Data Ordering 94
6.4 Data Processing Tool 96
6.5 Railway Subsidence Monitoring Process 97
6.5.1 Data Pre-processing Process 98
6.5.2 D-InSAR Process 99
6.5.3 PS-InSAR Process 103
6.5.4 Railway Subsidence Monitoring Result 110
6.6 Summary 114
Chapter 7 Railway Subsidence Prediction Case Study 116
7.1 Introduction 116
7.2 Input Data 116
7.3 Equal Interval Subsidence Series Simulation 117
7.3.1 ARIMA Model 117
7.3.2 Neural Network Model 119
7.3.3 Grey Model 120

7.4 Unequal Interval Subsidence Series Simulation 120
7.5 Simulation Results 122
7.6 Summary 124
Chapter 8 Conclusions and Future Work 125
8.1 Main Achievements 125
8.2 Summary of Contents 126
8.3 Conclusions 127
8.3.1 Railway Subsidence Monitoring 127
8.3.2 Railway Subsidence Prediction 128
8.3.3 Case Study of Railway Performance Assessment 128
8.4 Future Work 129
8.4.1 SBAS-InSAR in Railway Subsidence Monitoring 129
8.4.2 Railway Safety Assessment 130
Reference 132
Appendix A Available Envisat Data Sets 147
Appendix B Deformation Velocities of the PS along HS1 149
Appendix C MATLAB Script for PS-InSAR Data Processing 156
Appendix D R Modules Script for Time Series Prediction 160

List of Figures

Figure 1.1: Overview of poor railway performance 2
Figure 2.1: Structure of conventional ballasted track 8
Figure 2.2: Example of load distribution in ballasted track 8
Figure 2.3: Airborne InSAR system (left) and spaceborne InSAR system (right) 11
Figure 2.4: Electromagnetic spectrum 13
Figure 2.5: Penetration ability of radar band 14
Figure 2.6: Geometry of cross-track interferometry 15
Figure 2.7: Geometry of along-track interferometry 16
Figure 2.8: Geometry of repeat-pass interferometry 17
Figure 2.9: SRTM coverage map 19
Figure 2.10: Ground subsidence velocity map of the Jubilee Extension Line in London 28
Figure 2.11: Land subsidence velocity map of Jingshan Railway in 2004 29
Figure 3.1: Level only time series 33
Figure 3.2: Structure of the neural network 38
Figure 4.1: Principle of radar imaging 46
Figure 4.2: Geometry of real aperture radar 48
Figure 4.3: Relationship between slant range resolution and ground range resolution 49
Figure 4.4: Principle of synthetic aperture radar 51
Figure 4.5: Geometry for DEM generation 52
Figure 4.6: Radar propagation path and phase of radar pulse 53
Figure 4.7: Coherent phase image of the mountain (left) and incoherent phase image of the mountain (right) 58
Figure 4.8: Ground deformation monitoring by two-pass D-InSAR 59
Figure 4.9: Geometry of flat earth effect 62
Figure 4.10: Geometry of the topography effect 64
Figure 4.11: Simulated phase for a pixel without PS (a) and a pixel with PS (b) 70
Figure 5.1: Significant positive autocorrelation (no cut off) 76
Figure 5.2: Significant negative autocorrelation 77
Figure 5.3: ACF plots do not cut off (upper); PACF plots cut off at p=4 (lower) 78

Figure 5.4: ACF plots cut off at q=3 (upper); PACF plots do not cut off (lower).....79
Figure 5.5: ANN model with multilayers 83
Figure 6.1: Route configuration of HS1 91
Figure 6.2: Annual average rainfall for the period 1961-1990 92
Figure 6.3: Location of the study railway route and Envisat ASAR data coverage 93
Figure 6.4: User interface of EOLI-SA.....94
Figure 6.5: Railway subsidence monitoring process by StaMPS 98
Figure 6.6: Cropped magnitude images of the master date 26/12/2008 (left) and slave date 01/30/2009 (right) 99
Figure 6.7: Temporal and perpendicular baselines of the image pairs 100
Figure 6.8: Simulated magnitude image of the DEM.....101
Figure 6.9: Flattened interferogram (left) and interferogram after topographic phase removal (right) 102
Figure 6.10: The 20 differential interferograms created in the D-InSAR process.....103
Figure 6.11: Unwrapped phase of each differential interferograms 104
Figure 6.12: Unwrapped phase of each differential interferograms after removing the second interferogram 105
Figure 6.13: Annual average deformation velocity map 106
Figure 6.14: Time series deformation analysis of selected PS1 107
Figure 6.15: Time series deformation analysis of selected PS2 108
Figure 6.16: Time series deformation analysis of PS3 108
Figure 6.17: Annual average deformation velocity map on Google Earth 109
Figure 6.18: Annual average deformation velocity of PS on Google Earth 110
Figure 6.19: Deformation profile of selected sections of HS1 111
Figure 7.1: ACF and PACF Plots 117
Figure 7.2: Actual subsidence vs. predicted subsidence in ARMA.....118
Figure 7.3: Actual subsidence vs. predicted subsidence in neural network.....119
Figure 7.4: Actual subsidence vs. predicted subsidence in grey model.....120
Figure 7.5: Unequal interval actual subsidence vs. unequal interval predicted subsidence 122

List of Tables

Table 2.1: Designation of radar bands 12
Table 6.1: Envisat ASAR data from ESA 96
Table 6.2: Function of each free software integrated in StaMPS 96
Table 6.3: Summary of the railway deformation in North Downs Tunnel area 112
Table 6.4: Summary of the railway deformation between Hockers Lane Overbridge and Water Lane Underbridge 112
Table 6.5: Summary of the railway deformation at Ashford International Station ... 113
Table 7.1: Time intervals 121
Table 7.2: Original subsidence data 121
Table 7.3: New subsidence data 121
Table 7.4: RMSE comparison for equal interval time series 122
Table 7.5: Subsidence prediction comparison 123
Table A. 1: Available Envisat ASAR image mode data sets 148
Table B. 1: Annual average deformation velocities of the PS along HS1 155

List of Abbreviations

ACF	Auto Correlation Function
ACVF	Auto Covariance Function
AGO	Accumulated Generating Operation
ANFIS	Adaptive Neural Fuzzy Inference System
ANN	Artificial Neural Network
AR	Auto-Regressive
ARIMA	Auto-Regressive Integrated Moving Average
ARMA	Auto-Regressive Moving Average
MRTA	Mass Rapid Transit Authority
CRTL	Channel Tunnel Rail Link
CSA	Canadian Space Agency
CEOS	Committee on Earth Observation Satellites
DEM	Committee on Earth Observation Satellites
D-InSAR	Differential Interferometric Synthetic Aperture Radar
EPB	Earth Pressure Balance
Envisat	Environmental Satellite
Envisat ASAR	Envisat Advanced Synthetic Aperture Radar
ESA	European Space Agency
GPS	Global Positioning System
HS1	High Speed One
IAGO	Inverse Accumulated Generating Operation
IDS	Ingegneria Dei Sistemi
InSAR	Interferometric Synthetic Aperture Radar

JAXA	Japan Aerospace Exploration Agency
LiDAR	Light Detection and Ranging
LOS	Line of Sight
MA	Moving Average
NASA	National Aeronautics and Space Administration
NIMA	National Imagery and Mapping Agency
PACF	Partial Auto Correlation Function
PS	Persistent Scatterer
PS-InSAR	Persistent Scatterer Interferometric Synthetic Aperture Radar
PSC	Persistent Scatterer Candidates
RAR	Real Aperture Radar
RMSE	Root Mean Square Error
SAR	Synthetic Aperture Radar
SBAS-InSAR	Small Baseline Subset Interferometric Synthetic Aperture Radar
SLC	Single Look Complex
SNAPHU	Statistical-Cost, Network-Flow Algorithm for Phase Unwrapping
SRTM	Shuttle Radar Topography Mission
StaMPS	Stanford Method for Persistent Scatterers
TRE	Tele-Rilevamento Europa
USGS	U.S. Geological Survey

Chapter 1 Introduction

1.1 Background

The rapid increase in the demand for transportation of people and goods requires that railways have better capability. As a result of the improving capability, heavier axle loads and higher speed lines are current trends of railway development. Heavier axle loads and higher speed operation are two important reasons for track geometry changes and railway subsidence. Railway subsidence refers to permanent settlement of the track and subgrade. In addition, some geotechnical defects, such as initial compaction of the ballast bed and poor drainage condition of railway subgrade (Coelho, et al., 2011) are also contributors to track geometry changes and railway subsidence.

Unstable track geometry and inadequate railway subgrade will induce a poor railway performance, which includes poor ride quality, uncomfortable train journey, potential for train derailments, train service delay and increased fuel consumption. Moreover, frequent and expensive railway maintenance work is required to ensure a good railway performance. As a result, the life cycle costs of the railway will increase. Figure 1.1 shows an overview of poor railway performance.

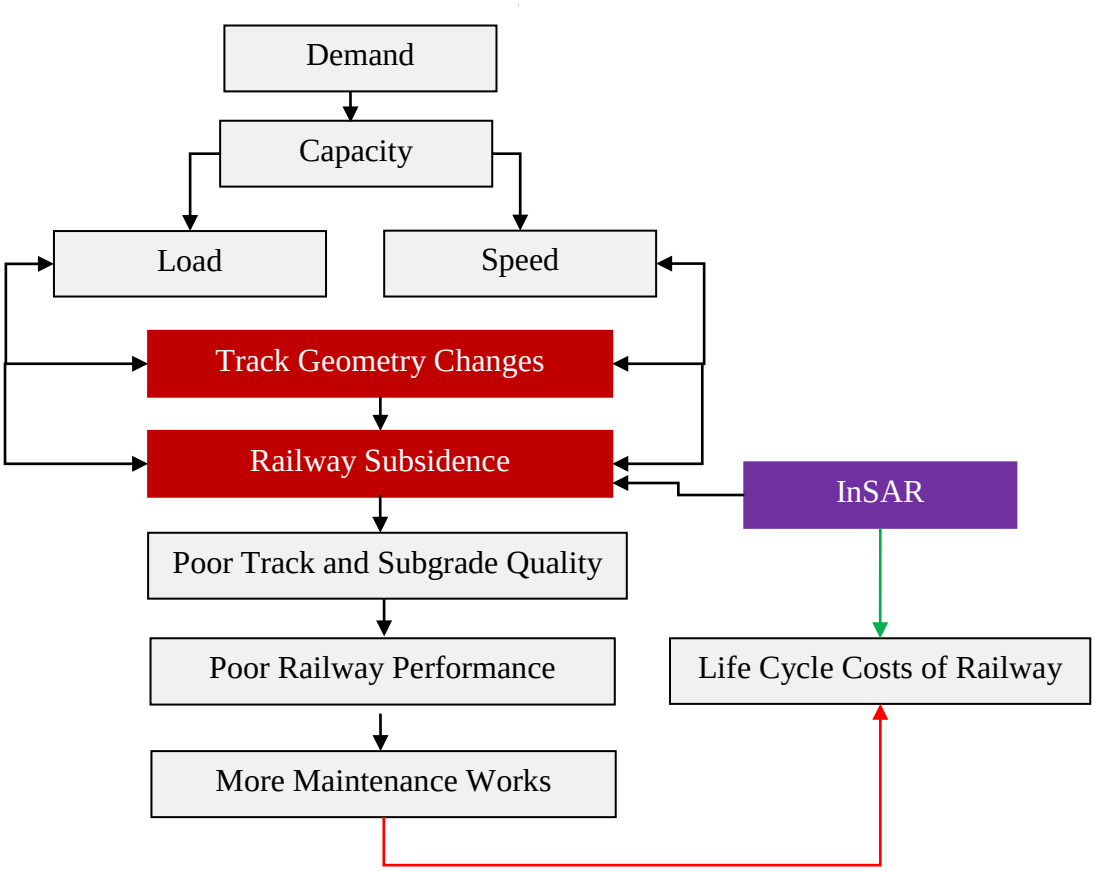

Figure 1.1: Overview of poor railway performance

In order to ensure good performance and reduce the life cycle costs of the railway, track geometry changes and railway subsidence should be monitored regularly. Track geometry changes can be measured by a track recording train or trolley based track measurement instrument. An approach for railway subsidence monitoring will be introduced in this thesis.

The railway is a linear construction and it subsides continuously over a long time period. Therefore, large coverage and a long time period are two important requirements for railway subsidence monitoring. In addition, repeatability, precision and efficiency of the monitoring approach, as well as labour costs should be considered. An Interferometric Synthetic Aperture Radar (InSAR) approach，which has the potential to measure ground deformation at millimetre level (Bamler & Hartl, 1998), is able to conduct railway subsidence monitoring over a large coverage and

long time period. As a result, InSAR is selected as an approach for railway subsidence monitoring.

In order to manage railway performance, railway subsidence prediction should be used alongside monitoring. Monitoring records of railway subsidence over a certain period can be considered as a typical discrete time series. Time series prediction models which are able to predict trends of railway subsidence based on historical subsidence monitoring records will be applied for railway subsidence prediction. In general, the main time series prediction models include statistical model auto-regressive moving average (ARMA), a neural network model based on artificial intelligence and a grey model which is capable of handling time series that have a limited number of observations with unknown parameters and inter-relationships.

By the application of railway subsidence monitoring and railway subsidence prediction, this thesis provides an approach for assessing railway performance.

1.2 Objectives

The author aims to introduce a method to monitor railway subsidence over a large coverage and long time periods and to predict subsidence of the railway based on historical monitoring records. Three objectives of this thesis are presented below.

(1) To provide an integrated approach for railway performance assessment

Based on the current trend of railway development, an overview of poor railway performance is indicated. In order to improve performance and reduce life cycle costs of the railway, an approach for assessing railway performance is introduced, which includes subsidence monitoring and prediction.

(2) To provide an approach to monitor railway subsidence

The InSAR technique, which is suitable for subsidence monitoring over a large coverage and long time period, is applied in this research. A case study which adopts InSAR in subsidence monitoring of the High Speed One (HS1) railway is conducted to assess the feasibility of InSAR in railway subsidence monitoring. Based on the InSAR results of this case study, the stability status of HS1 can be assessed and railway sections with potential subsidence can be indicated.

(3) To provide an approach to predict railway subsidence

InSAR results provide historical monitoring records of railway deformation, a railway subsidence prediction will be carried out based on the monitoring records. Time series prediction models will be reviewed and applied in this thesis. A comparison between the prediction results of railway subsidence obtained from different time series prediction models will be conducted and the model which is the most suitable for railway subsidence prediction will be identified.

1.3 Thesis Structure

This thesis contains eight chapters and the detailed thesis structure is given as follows.

(1) Chapter 1 introduces the research background. Based on the background, the 3 objectives of the thesis are presented. In addition, a thesis structure which generally introduces each chapter is presented.

(2) Chapter 2 reviews three approaches for railway subsidence monitoring and selects InSAR for this research. This chapter introduces the development of InSAR and its main applications in various research areas. InSAR is able to measure the topography of the study area while Differential InSAR (D-InSAR) works well in ground deformation monitoring. Due to the limitations of D-InSAR, Persistent Scatterer InSAR (PS-InSAR) is applied to obtain a more reliable ground deformation result. The successful applications of PS-InSAR in ground deformation monitoring ensure the feasibility of applying it in railway subsidence monitoring. Three applications of PS-InSAR in railway subsidence monitoring are also presented in this chapter.

(3) Chapter 3 reviews time series models for railway subsidence prediction. PS-InSAR is able to conduct a time series analysis of the stable Persistent Scatterers (PS) along the railway. As a result, historical deformation records obtained by PS-InSAR can be considered as the discrete time series. In order to predict subsidence trends of the railway in the future, chapter 3 presents three prediction models which are applicable for discrete time series, which are the traditional statistical model, a neural network model based on artificial intelligence and a grey model which is suitable for a system with partially known parameters. This chapter also reviews some practical applications of these three models in subsidence prediction.

(4) Chapter 4 describes the methodologies of InSAR applied in railway subsidence monitoring. In order to extract the real ground deformation which has occurred during a time period, a radar image pair captured before and after the ground deformation is required. Instead of traditional Real Aperture Radar (RAR), Synthetic Aperture Radar (SAR) with a shorter radar antenna is applied to capture radar images with good resolution and obtain a good ground deformation result. This chapter describes the principle of InSAR for the generation of Digital Elevation Model (DEM) and the principle of PS-InSAR for obtaining a reliable ground deformation result.

(5) Chapter 5 introduces the methods of time series prediction models in railway subsidence prediction. The traditional statistics prediction model auto-regressive integrated moving average (ARIMA) is introduced in this chapter, which includes the method applied in ARIMA and detailed procedures for utilising it in subsidence prediction. In addition, a neural network model based on artificial intelligence is reviewed. This chapter describes the construction of the multi-player neural network, functions for output generation and the detailed procedures for the learning algorithm gradient descent backpropagation. This chapter also presents working procedures for a grey model.

(6) Chapter 6 presents a case study, monitoring subsidence of HS1 by applying PS-InSAR. A 53 km railway route, from Southfleet Junction near Ebbsfleet International Station to Ashford International Station is configured in this chapter. Due to tunnelling work, geology and large rainfall on the selected route, it faces potential railway subsidence. This chapter also introduces procedures for the collection of the radar data used for PS-InSAR and the data processing tool for PS-InSAR. According to the data processing result, a time series analysis of selected PS along HS1 is conducted and the deformation profile of HS1 is created. The subsidence monitoring results indicate the subsidence status of HS1 and the railway sections of HS1 with potential subsidence risk in the future.

(7) Chapter 7 describes the applications of a time series prediction model for railway subsidence prediction based on deformation monitoring results obtained from PS-InSAR in chapter 6. Two simulations are conducted in this chapter, which are a simulation for equal interval time series and a simulation for unequal interval time

series. For the time series with equal intervals, ARIMA, a neural network model and a grey model are applied separately for the simulation. For the time series with unequal intervals, only the grey model is used as it is the only model of the three which is able to handle an unequal interval time series.

(8) Chapter 8 summarises the main contents presented in this thesis and provides conclusions for this research. In addition, future works for this research are also indicated.

(9) Appendix A shows a list of available Envisat ASAR data while Appendix B presents the summary of the railway deformation for the case study. In addition, Appendix C provides the scripts for PS-InSAR data processing of the case study described in chapter 6. Appendix D presents the scripts of ARIMA, the neural network model and grey model for the case study of railway subsidence prediction in chapter 7.

Chapter 2 Review of Railway Subsidence Monitoring

2.1 Introduction

Poor railway performance caused by heavier axle loads and higher speed lines induces a higher life cycle costs for the railway and safety problems in train operation. This chapter aims to introduce a method which can ensure good railway performance by monitoring railway subsidence over a large area and a long time period.

Firstly, the nature of railway infrastructure and subsidence is introduced. Secondly, three approaches for railway subsidence monitoring are reviewed. After comparing the pros and cons of these approaches, the Interferometric Synthetic Aperture Radar (InSAR) technique, which is able to monitor ground subsidence with millimetre precision over a large area and a long time period, is selected for railway subsidence monitoring in this research. Then, the development and main applications of InSAR in various research areas are reviewed. Ground subsidence monitoring is one of the most important applications of InSAR. Based on its principles, subsidence of the railway can be monitored. This chapter represents three successful applications of railway subsidence monitoring.

2.2 Nature of Railway Infrastructure and Subsidence

The quality of the railway infrastructure determines its affordable traffic. As two of the most important components of railway infrastructure, stable track and the track foundation ensure good quality of the railway infrastructure. Conventional ballasted track, which is the most widely used track, requires multiple layers of materials underneath the sleepers for support. Figure 2.1 illustrates the structure of conventional ballasted track (Vehicle /Track System Interface Committee, 2010). Track is comprised of flat bottom rails and sleepers while track foundation consists of ballast, sub-ballast, a protective layer and subgrade.

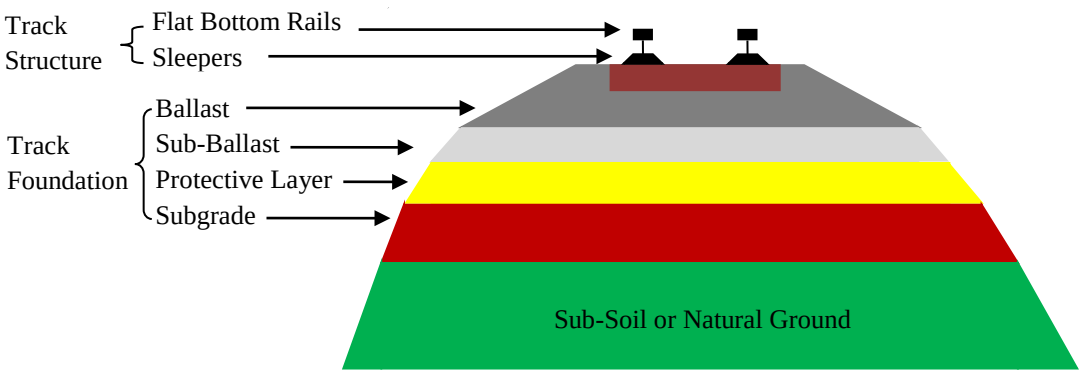

Figure 2.1: Structure of conventional ballasted track

The sleepers not only support the rails but also transfer dynamic loads into the ballast. Figure 2.2 shows an example of load distribution in ballasted track (Vehicle /Track System Interface Committee, 2010). A 350 kilonewton dynamic wheel force is applied on the rail and the other components of the ballasted track also bear the pressure distribution.

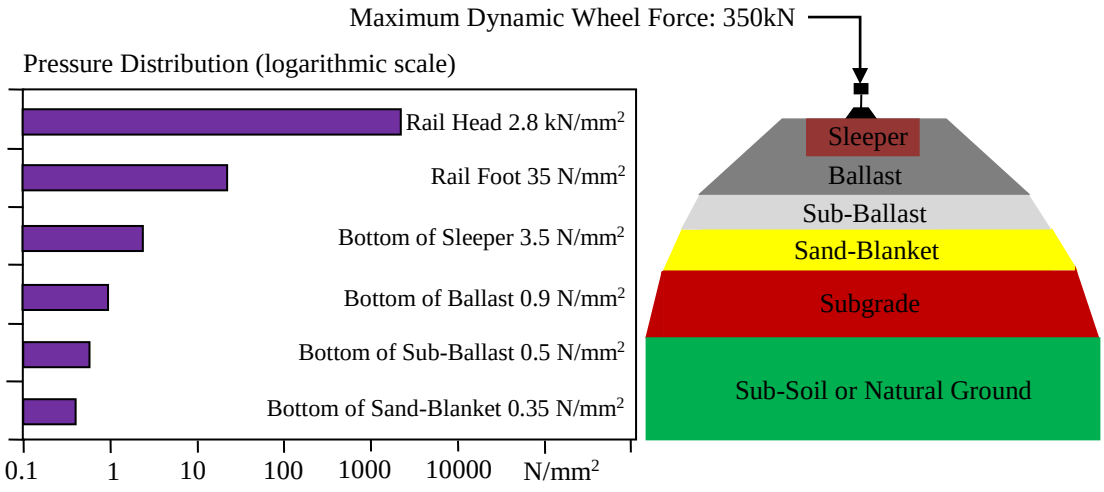

Figure 2.2: Example of load distribution in ballasted track

Due to the pressure loaded onto the ballasted track, settlement of the ballast may occur, which further results in the settlement of the subgrade and natural ground

underneath the subgrade. Except for the settlement of the subgrade and natural ground caused by pressure, some factors, such as drainage and a large volume of rainfall, can also lead to the settlement of the subgrade and natural ground, eventually causing railway subsidence.

2.3 Approaches for Railway Subsidence Monitoring

Subsidence of the railway can cause track deterioration and, in some areas, has become a threat to good railway performance. As a result, railway subsidence should be monitored regularly. Three approaches, namely levelling survey, Global Positioning System (GPS) and radar based systems, are mainly used for railway subsidence monitoring.

A levelling survey is the most precise approach in vertical ground deformation monitoring. Based on levelling data collected since 1935, Bell and his colleagues worked on the ground subsidence in Las Vegas Valley (Bell, et al., 2002). In addition, precise levelling data was applied to monitor the subsidence of the Taiwan High Speed Rail (Hwang, et al., 2008). Benchmarks in a levelling survey are discrete and their number is limited. As a result, it is difficult to depict ground deformation over a large coverage. In addition, frequent surveys increase costs due to the human resources required to carry them out. GPS performs well in horizontal ground deformation monitoring. However, for a precise result of vertical ground deformation, a long period of monitoring must be conducted. For instance, Hill and Blewittit demonstrated that a long time period (more than 5 years) of GPS monitoring can be applied to detect tectonic signals with a vertical rate greater than 0.3 mm per year in the Yucca Mountain area in Nevada (Hill & Blewitt, 2006). In addition, 16 GPS pillars were deployed along the Taiwan High Speed Rail for subsidence monitoring (Hwang, et al., 2008). GPS pillars are discrete and often sparse, with spacing from a few kilometres to a few hundred kilometres.

Radar based system for railway subsidence monitoring can be divided into track based system and satellite based system. Track based LiDAR (Light Detection and Ranging) can be used to map ground features and settlement. LiDAR technique is able to precisely locate the survey target on the ground by transmitting radar pulses and recording backscattered radar signal (Baran, 2009). Zetica applied LiDAR surveys on

rail infrastructure (Zetica, 2015) while Ingegneria Dei Sistemi (IDS) also provided supports on measuring railroad and mapping track structure based on LiDAR technique (Zarembski, et al., 2013). However, deviation of radar trajectories may lead to errors in LiDAR survey results.

Due to the fact that the railway is a long linear construction which subsides continuously over a long time period, both levelling survey and GPS approaches have limitations in monitoring railway subsidence. An approach which can cover a large area and allow a frequent monitoring in a long time period should be used to monitor railway subsidence. InSAR is a repeatable and continuous satellite based technique with good accuracy, wide coverage and stable radar trajectory. Additionally, it has the potential to measure ground surface deformation to millimetre precision over a period of days or years. As a result, satellite based InSAR technique is adopted to monitor railway subsidence in this research.

2.4 Development of InSAR

The development of InSAR can be traced to the late 1960s. In 1969, radar interferometry was first applied for probing the planet Venus. Radar with 3.8 cm wavelength on the Earth was used to map the surface reflectivity of Venus (Rogers & Ingalls, 1969). Similarly, radar interferometry was undertaken to map the topography of the Moon by Zisk in 1972 (Zisk, 1972).

InSAR was first proposed to use an airborne Synthetic Aperture Radar (SAR) system with a cross-track platform to obtain topography information of the Earth. A Digital Elevation Model (DEM) of the Earth was generated in1974 (Graham, 1974). In 1986, Zebker and Goldstein indicated the first practical result of InSAR. A cross-track airborne InSAR system was applied to generate a DEM of the Golden Gate Bridge area in San Francisco (Zebker & Goldstein, 1986). Later, Goldstein and Zebker described a new airborne InSAR system with an along-track platform in 1987 (Goldstein & Zebker, 1987). A map of ocean currents in San Francisco Bay was depicted by the along-track InSAR. Based on the SAR images captured by the Seasat mission with the repeat-pass platform, a DEM of the Cottonball Basin in Death Valley was generated by Goldstein and his colleagues in 1988, which was the first application of spaceborne InSAR (Goldstein, et al., 1988).

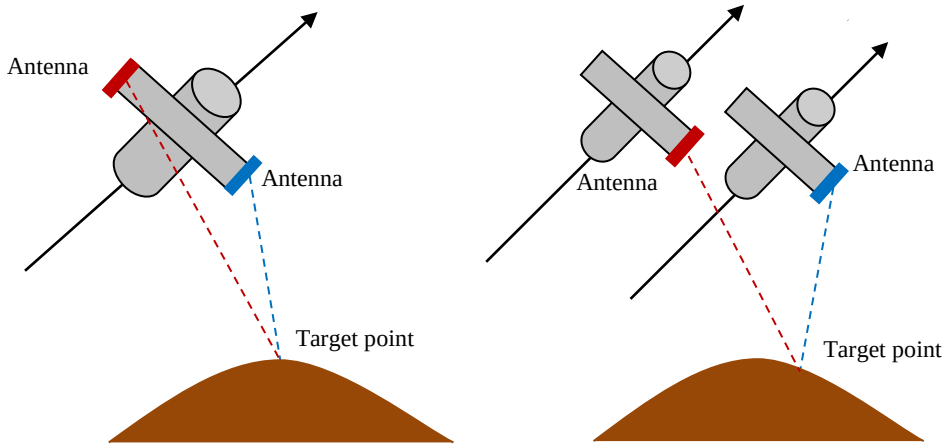

Figure 2.3: Airborne InSAR system (left) and spaceborne InSAR system (right)

In 1989, Gabriel first adopted InSAR to measure ground deformation (Gabriel, et al., 1989). However, as well as ground deformation information, topographic information was also represented in the InSAR results. In order to remove topographic information and obtain real ground surface deformation, Differential InSAR (D-InSAR) was applied to monitor ground deformation in the Imperial Valley region in California based on the Seasat SAR images (Gabriel, et al., 1989).

According to the number of SAR images required, D-InSAR is divided into two-pass D-InSAR, three-pass D-InSAR and four-pass D-InSAR. Three-pass D-InSAR was adopted in the first application of D-InSAR in 1989 (Gabriel, et al., 1989). Later, Zebker and his colleagues conducted three-pass D-InSAR to remove topographic information from the interferogram of the region of Alaska in 1994 (Zebker, et al., 1994). Similarly, four-pass D-InSAR was applied to measure the velocity of glacier movement in 1996 by Kwok and Fahnestock (Kwok & Fahnestock, 1996). In 1993, Massonnet and his colleagues utilised two-pass D-InSAR to remove topographic information from the deformation result of the Landers Earthquake in California. External DEM was selected as the reference in two-pass D-InSAR to remove topographic information (Massonnet, et al., 1993). Later, two-pass D-InSAR was

adopted by Cumming et al. in 1997 to monitor alpine glacier flow (Cumming, et al., 1997).

As an enhanced D-InSAR technique, Persistent Scatterer InSAR (PS-InSAR) was applied by Ferretti and his colleagues to mitigate the effects of temporal decorrelation of the interferograms and atmospheric delay in 2000 (Ferretti & Rocca, 2000). Since the first application of PS-InSAR in 2000, it has been widely adopted. Usai in 2001 (Usai, 2001), Kampes and Hanssen in 2004 (Kampes & Hanssen, 2004) utilised PS-InSAR in their research.

2.5 Acquisition of SAR Image

2.5.1 Designation of Radar Band

Beams of radar pulses are transmitted from a radar antenna to the ground and the ground is illuminated by the radar beams. Backscattered radar beams are recorded by the radar antenna, and a radar image, which represents the topography of the illuminated area, is generated.

In 1986, Trevett designated radar bands by wavelength and frequency of radar wave (Trevett, 1986). Table 2.1 indicates the designation of each radar band.

Radar Band	Wavelength (cm)	Frequency (MHz)
K_a	0.75-1.18	36500-40000
K	1.18-1.67	18000-26500
K_u	1.67-2.40	12500-18000
X	2.40-3.75	8000-12500
C	3.75-7.5	4000-8000
S	7.5-15	2000-4000
L	15-30	1000-2000
UHF	30-100	300-1000
P	77-136	220-390

Table 2.1: Designation of radar bands

Radar bands X, C and L are widely adopted in the SAR systems; their respective wavelengths are 3.1cm, 5.8cm and 23.5cm (Plaut, 1996). Based on the electromagnetic spectrum represented in Figure 2.3, a radar wave in a SAR system is classified as a microwave, which has wavelength range from 1 mm to 1 m.

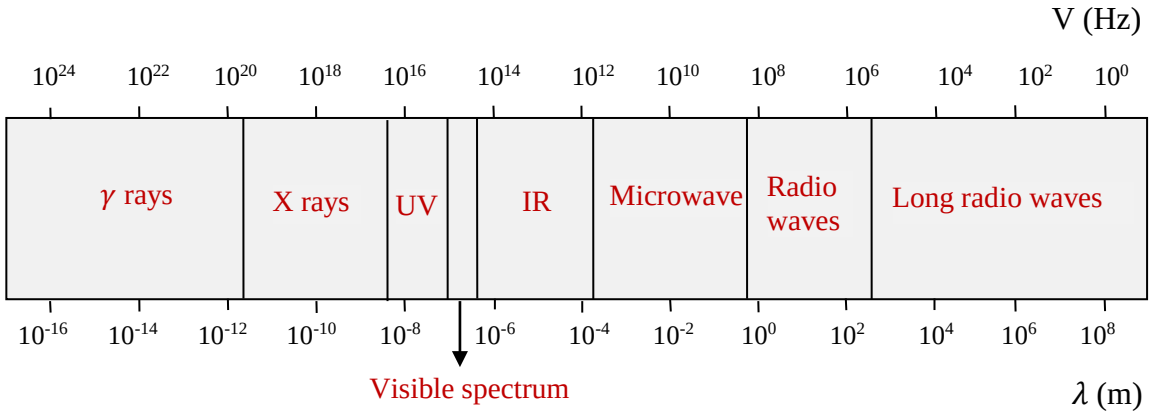

Figure 2.4: Electromagnetic spectrum

According to the characteristics of a microwave, it can penetrate cloud, atmosphere, fog, haze, rain and vegetation (Woodhouse, 2006). Therefore, using InSAR the results of ground deformation monitoring will not be affected by cloud cover or the weather. Jensen denoted that radar with a longer wavelength has a better ability for penetration and is good at volume scattering (Jensen, 2007). As shown in Figure 2.4 (Jensen, 2007), compared with X band radar pulses, which only penetrate the top of the tree, L band radar pulses can penetrate leaves and branches of the tree, and more radar pluses are backscattered. As a result, L band radar works well areas covered by the vegetation.

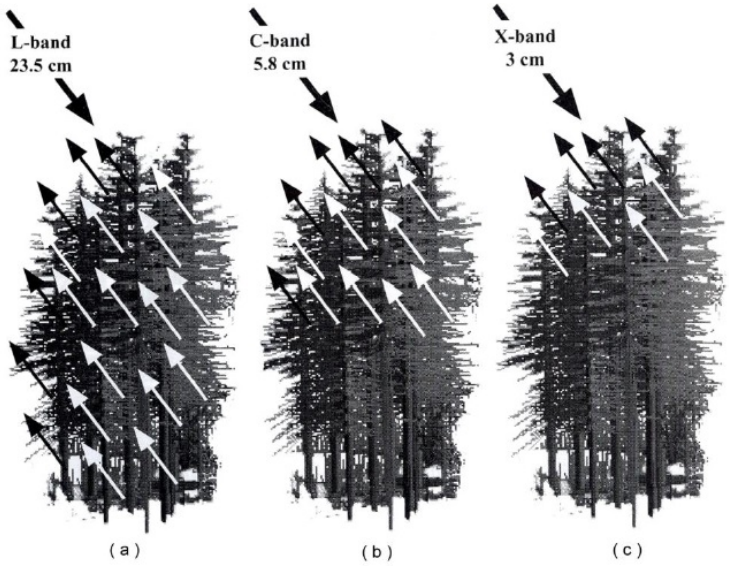

Figure 2.5: Penetration ability of radar band

As well as penetrability, reflectivity is another characteristic of the microwave radar. Jensen indicated that radar with a short wavelength is good at surface reflectivity and it can capture the high resolution SAR image in areas with more scatterers (Jensen, 2007).

2.5.2 Image Acquisition Modes

SAR images can be obtained by the airborne and spaceborne radar platforms, which are configured respectively as single-pass interferometry and repeat-pass interferometry. Single-pass interferometry can be further divided into cross-track interferometry and along-track interferometry according to the positional relationship between the radar antenna and the direction in which the radar is moving.

(1) Cross-track interferometry

Cross-track radar interferometry is carried out by a platform equipped with two airborne radar antennas whose baseline is perpendicular to the direction in which the radar is moving (Massonnet & Felgl, 1998). Baseline is the distance between orbital trajectories of the two radar antennas.

One radar antenna emits a radar pulse and receives radar echo, while the other radar antenna can only receive radar echo. Cross-track platform is able to capture a pair of

interferometric radar images when the airborne radar is passing over the target area (Matias, 2006). Figure 2.5 represents the geometry of cross-track interferometry.

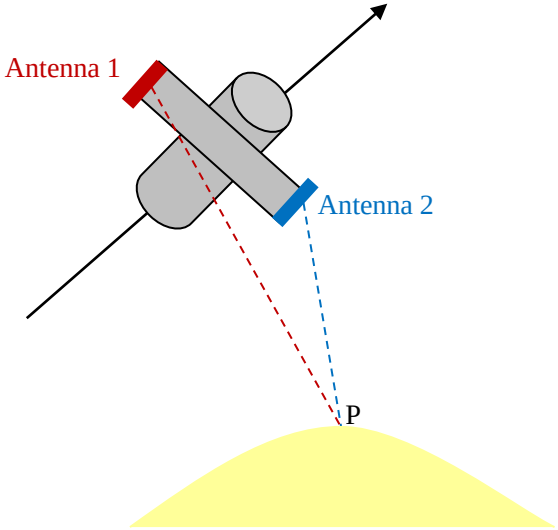

Figure 2.6: Geometry of cross-track interferometry

The phase difference between the radar echoes results from the different position of the antennas. In cross-track interferometry, the instantaneous position difference of the two antennas in respect to the scatterer on the ground is on the direction which is perpendicular to the direction of the radar moving. As a result, Cross-track interferometry is sensitive to changes in the topographic elevation (Romeiser, et al., 2007). Cross-track interferometry has been widely adopted in the DEM generation. However, errors caused by terrain slope and tilt of the aircraft are difficult to be removed from the the interferometric phase of the interferogram generated from the radar image pair.

(2) Along-track interferometry

Along-track radar interferometry is conducted by an aeroplane based platform with two radar antennas whose baseline are parallel to the moving direction of the radar (Hirsch, 2001). Similarly, one radar antenna transmits a radar pulse and receives the radar echo while the other antenna only receives the radar echo. Figure 2.6 represents the geometry of along-track interferometry.

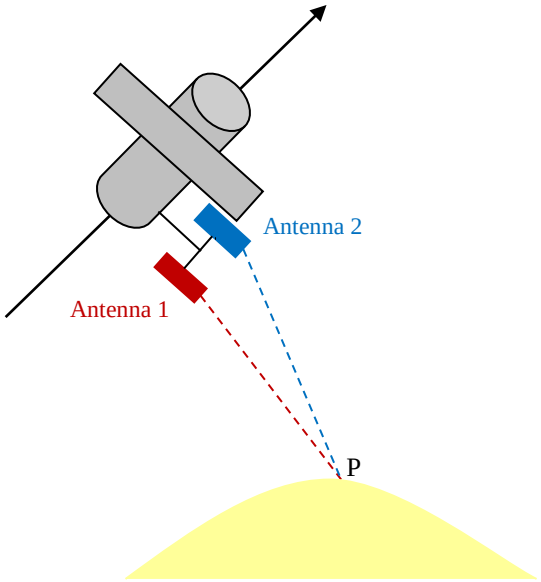

Figure 2.7: Geometry of along-track interferometry

When the airborne radar is passing over the target area, a pair of radar images is obtained by the two radar antennas. In along-track interferometry, the instantaneous position difference of the two antennas in respect to the scatterer on the ground is parallel to the direction in which the radar is moving. Accordingly, along-track interferometry is sensitive to deformation along the direction in which the radar is moving, and it has been widely applied in the movement monitoring of ocean currents (Hirsch, 2001).

(3) Repeat-pass interferometry

In order to monitor ground deformation, a pair of radar images captured at different times is required. However, two flight trajectories of the aircraft can not be guaranteed to be the same. Trajectory deviations of the aircraft will bring errors in the interferogram (Fornaro, 1999). As a result, a spaceborne radar platform with stationary orbit is adopted to capture a radar image pair for ground deformation monitoring.

Repeat-pass interferometry is undertaken on the spaceborne radar platform. Different to airborne radar, only one antenna is provided for each spaceborne radar. Two radars

with a single antenna on the parallel radar orbits are able to obtain a pair of radar images of the same target at different times (Hagberg, et al., 1995).

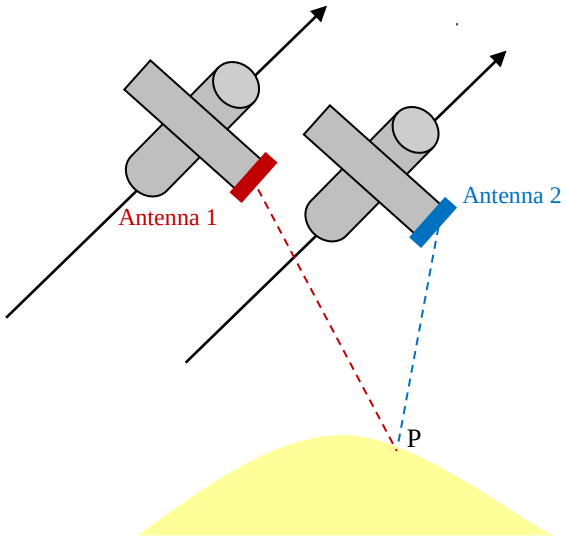

Figure 2.8: Geometry of repeat-pass interferometry

2.5.3 Satellites for Image Acquisition

Since the Jet Propulsion Laboratory in the U.S. launched the first satellite with a SAR system in June 1978, Seasat, it has been possible to capture SAR images by using spaceborne radar. The Seasat satellite was used to undertake remote sensing of the ocean on the Earth based on a SAR approach. Due to a short circuit of the electric power system, the useful life of this satellite ended 4 months after its launch (NASA, 2014). The launch of the satellite with a SAR system significantly speeded up the development of InSAR and broadened the scope of InSAR applications.

The European Space Agency (ESA) launched ERS-1 satellite in 1991, ERS-2 satellite in 1995 (ESA, 2014) and Envisat (Environmental Satellite) in 2002, whose image mode has the 30 m spatial resolution and the 100 km swath coverage (ASAR Instrument Functionality, 2014). JERS-1 and ALOS PALSAR were launched by the Japan Aerospace Exploration Agency (JAXA)[1] in 1992 and 2006 respectively (Japan Aerospace Exploration Agence, 2004) (Rosenqvist, et al., 2004).

[1] JAXA used to be National Space Development Agency of Japan (NASDA)

In addition, the Canadian Space Agency (CSA) launched its RADARSAT-1 in 1995 and RADARSAT-2 in 2007 (Hurley, 2010). RADARSAT-2 is able to capture SAR images with the spatial resolution up to 3 m. Since the launch of RADARSAT-2, more satellites with higher spatial resolution were applied in ground deformation monitoring. For instance, TerraSAR-X and COSMO SkyMED, which were both launched in 2007 and operated by the German Aerospace Centre (DLR[2]) and the Italian Space Agency (ASI) respectively, have spatial resolution up to 1 m (GEOIMAGE, 2012) (ISA, 2007).

Due to the high spatial resolution (up to 1 m) and a short revisit time (11 days), TerraSAR-X data has been widely adopted in ground deformation monitoring. Wegmuller and his colleagues conducted PS-InSAR based on TerraSAR-X data to monitor ground deformation (Wegmuller, et al., 2010).

Compared with the expensive high resolution TerraSAR-X data, Envisat data provided by ESA are free of charge for the academia. Osmanoğlu and his colleagues worked on subsidence monitoring for Mexico City by PS-InSAR using Envisat data (Osmanoğlu, et al., 2011). This thesis aims to identify railway sections with significant subsidence, which does not have a particularly high requirement for the spatial resolution. As a result, Envisat data are chosen for railway subsidence monitoring in this research.

2.6 Applications of InSAR

Since the first application of radar interferometry in 1969, InSAR has been widely applied. Applications of InSAR can be divided into four categories, which are topography mapping, DEM generation, ocean currents mapping and landscape characterization (Lu, et al., 2007).

2.6.1 Topography Mapping

The initial purpose of InSAR is to carry out topography mapping based on ground surface reflectivity. Radar interferometry was first applied to map the topography of

[2] Deutsches Zentrum für Luft- und Raumfahrt in German

the planet Venus in 1969 (Rogers & Ingalls, 1969) and later to the topography of the Moon, which was mapped by the same method in 1972 (Zisk, 1972).

2.6.2 DEM Generation

InSAR is able to monitor topography of the target area by a single-pass airborne radar platform and finally generate a DEM of this area. When the airborne radar is passing over the target area, a pair of radar images is captured by the two radar antennas at the same time. Therefore, there is no time interval between the two acquisitions of the images and external condition, such as vegetation change, do not affect the result of the DEM generation. Moreover, weather conditions will not affect the DEM generation by InSAR due to the good penetrability of radar wave. In addition, InSAR is able to generate a DEM of areas where traditional methods cannot gain access.

In 2000, National Aeronautics and Space Administration (NASA) and the National Imagery and Mapping Agency (NIMA) cooperated on a project which aimed to map the Earth in three dimensions. Shuttle Radar Topography Mission (SRTM) was developed by the single-pass airborne InSAR, and a world-wide DEM was generated (Bamler, et al., 2003).

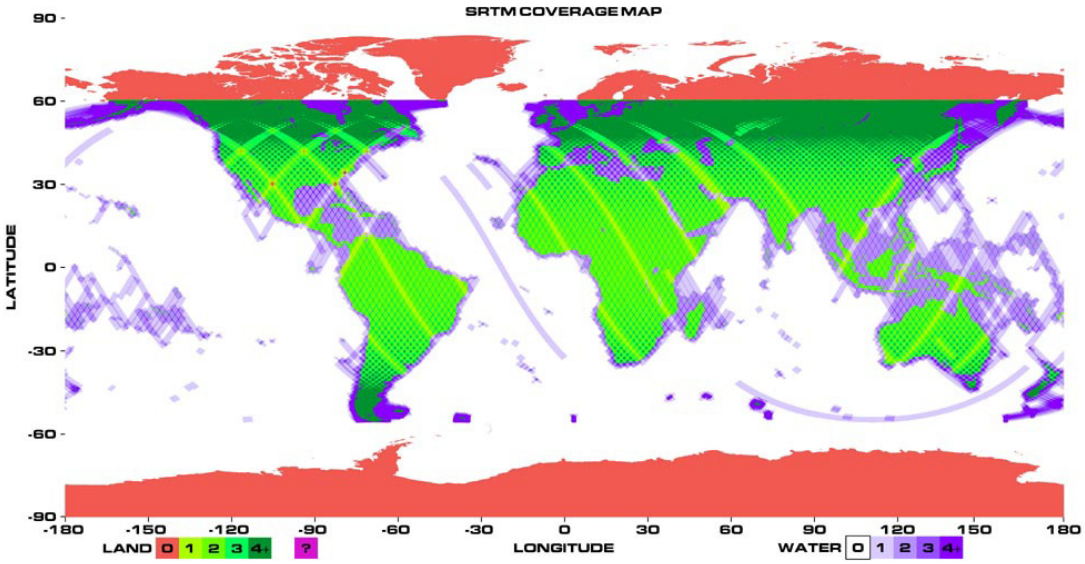

Figure 2.9: SRTM coverage map

The surface of the Earth between 60 degrees north latitude and 56 degrees south latitude was mapped by SRTM, and a DEM of the mapped area was generated (Van

Zyl, 2001). Jet Propulsion Laboratory stated that about 80% of the land surface on the Earth is covered by SRTM (Jet Propulsion Laboratory, 2005). As shown in Figure 2.8, the surface of the Earth which is not coloured red is covered by SRTM.

2.6.3 Ocean Currents Mapping

Ocean currents mapping is another important application of InSAR. Radar wave can go through atmosphere and cloud to the ocean surface. Ocean currents can be mapped due to variances in the roughness of the ocean surface (Mikhail, 2009).

The velocity of ocean currents was measured by Siegmund and his colleagues by hybrid along-track and cross-track InSAR in 2004 (Siegmund, et al., 2004). Baek and Shum measured ocean tidal heights by D-InSAR in 2011 (Baek & Shum, 2011). InSAR has also been applied to monitor the movement of coastline by extracting coastline from SAR images (Dellepiane, et al., 2004).

2.6.4 Landscape Deformation Measurement

In terms of monitoring landscape characterization, most researchers have focused on seismic deformation, subsidence and uplift of the volcano, glacier movement, and topography deformation.

(1) Seismic deformation

Ground deformation of the 1992 Landers earthquake was firstly mapped by InSAR in 1998 (Massonnet & Felgl, 1998). A pair of radar images which were captured before and after the earthquake was applied in the research. Later, InSAR was widely adopted in seismic deformation monitoring, such as the Antofagasta earthquake in Chile in 1995 (Pritchard, et al., 2002), the Hector Mine earthquake in California in 1999 (Simons, et al., 2002), the Wenchuan Earthquake in China in 2008 (Lin, et al., 2009), etc.

(2) Subsidence and uplift of the volcano

InSAR has been successfully applied in detecting the volcanic eruption. Subsidence and uplift detection of Alaskan volcanoes in 2002 (Lu, et al., 2002) and the Sierra Negra Volcano in 2006 (Yun, et al., 2006) were undertaken by InSAR.

(3) Glacier movement

Glacier movement monitoring is another important application of InSAR, which supports the research on global warming and sea level change. Surface deformation of the active alpine rock glaciers was monitored by Kenyi and Kaufmann in 2003 (Kenyi & Kaufmann, 2003). Later, Joughin and his colleagues measured the velocities of JakobshavnIsbræglaciersin Greenland and found large fluctuations (Joughin, et al., 2004).

(4) Topography deformation

Topography deformation includes landslides, ground deformation, etc. Hilley and his colleagues worked on the monitoring of slow-moving landslides using PS-InSAR and published a paper in 2004 (Hilley, et al., 2004).

Differing from ground deformation caused by the earthquakes and volcanic activity, ground subsidence caused by excessive exploitation of ground water, coal mining, oil mining and construction of infrastructure occurs slowly. The time period for ground deformation monitoring can be several years. As a result, temporal decorrelation should be considered. The hydrologic dynamics of the Sian Ka'an Wetlands in Mexico were monitored by Gondwe and his colleagues in 2010 (Gondwe, et al., 2010). Subsidence of the Samchukcoal field in Korea was measured by D-InSAR in 2008 (Baek, et al., 2008). In addition, PS-InSAR was applied to monitor ground subsidence of the Jingjin Railway in China (Ge, et al., 2008).

2.7 Ground Deformation Monitoring by D-InSAR

Due to the slow progression of ground deformation, there must be a time interval between the acquisitions of the two radar images required for ground deformation monitoring. Apart from the information on ground deformation, topographic information also has an impact on the ground deformation results derived from the interferogram. As a result, the topographic phase should be removed from the interferometric phase of the interferogram to obtain real ground deformation results (Adam, et al., 2003).

In order to remove the topographic phase and extract the ground deformation results, D-InSAR, which applies differential interferometry to one interferogram which only contains topographic information and the other one interferogram which contains not

only topographic information but also ground deformation information, is used in this research. D-InSAR is considered as the only approach to monitor ground deformation with large spatial and temporal scales to millimetre precision (Bamler & Hartl, 1998).

2.7.1 Classifications of D-InSAR

According to the number of radar images used in differential interferometry, D-InSAR can be divided into two-pass D-InSAR, three-pass D-InSAR and four-pass D-InSAR (Lubis, et al., 2011).

(1) Two-pass D-InSAR

Undulating terrain may reduce the accuracy of DEM generation by InSAR. As a result, external DEM should be adopted in D-InSAR to remove topographic information for an area with undulating terrain (Liao, et al., 2007). Two-pass D-InSAR is an approach to monitor ground deformation by applying differential interferogram to the two interferograms. The magnitude map simulated by external DEM and orbital trajectory of the radar is considered as the first interferogram, while the other interferogram is generated from a pair of radar images captured before and after ground deformation.

The simulated magnitude map only contains topographic information, while the phase of the second interferogram contains both topographic information and ground deformation information. As a result, topographic information can be removed by undertaking differential interferometry and the ground deformation results can be generated.

(2) Three-pass D-InSAR

For areas with the flat terrain, three-pass D-InSAR can be adopted to measure ground deformation by generating two interferograms based on three radar images (Liao, et al., 2007).

The first interferogram is obtained from two radar images captured before ground deformation while the second interferogram is generated from one radar image captured after ground deformation and any one of the two radar images obtained before ground deformation. Only topographic information is contained in the first interferogram and both topographic information and ground deformation information

exist in the second interferogram. The ground deformation results can be obtained after undertaking differential interferometry.

(3) Four-pass D-InSAR

In four-pass D-InSAR, two interferograms are generated from four radar images. The first interferogram is generated from two radar images obtained before the ground deformation while the second interferogram is obtained from the other two radar images captured after the ground deformation. Both of the interferograms contain only topographic phase and the topography information of the monitoring area before and after the ground deformation can be obtained by the interferograms. Accordingly, the ground deformation results can be extracted from the differential interferogram created by the two interferograms (Agustan, 2010).

2.7.2 Limitations of D-InSAR

D-InSAR has been widely adopted in ground deformaiton monitoring. However, the reliability of a D-InSAR result is reduced due to its limitations.

(1) Temporal decorrelation

If the time interval for the acquisition of two radar images is too long, vegetation coverage and the topography of the monitored area will change, which results in changes in the characteristics of the scatterers on the ground (Gondwe, et al., 2010). As a result, temporal decorrelation may occur on the interferogram generated from this radar image pair. In addition, phase delay of the radar pulse occurring in the ionosphere and troposphere of the atmosphere also contribute to the temporal decorrelation (Li, et al., 2009) (Ding, et al., 2008).

(2) Spatial decorrelation

If the baseline between two radar antennas is too long, look angles (see Figure 4.2) for the two acquisitions of radar images are significantly different. Different phase of radar pulses caused by different look angles result in low coherence between the radar pulses and spatial decorrelation on the interferogram generated from the radar image pair (Strozzi, et al., 2001). In addition, phase delay caused by variability of atmospheric water vapour is another reason for spatial decorrelation (Hanssen, 2001).

(3) Phase noise in D-InSAR

Except for the ground deformation, phase caused by flat earth effects, topographic effects, atmospheric delay, orbit error and random phase noises are considered as the phase noise of the interferogram. Phase cycle and continuity of the interferometric fringes in the interferogram are affected by the phase noise. In order to extract real ground deformation results from the interferogram, phase noise must be removed.

- Flat earth effect

For an area with flat terrain, there is no periodic change in the interferometric fringes in the interferogram. Due to the curvature of the Earth's surface, propagation distances of the radar pulses between radar antenna and the scatterers on the ground are different (see Figure 4.9). As a result, phase difference of radar pulses caused by different propagation distances leads to periodic changes in interferometric fringes in the interferogram, which is considered to be the flat earth effect.

The flat earth effect can result in dense interferometric fringes, which are periodic changes to interferometric fringes in the interferorgam of the area without ground elevation change. In addition, an interferogram with flat earth effect is difficult for phase unwrapping (Strozzi, et al., 2001). A phase caused by flat earth effect can be removed based on the precise orbit data of the radar and the geometric principle of radar imaging (Li, et al., 2004).

- Topographic effect

In addition to the flat earth effect, undulating topography of the Earth will also lead to different propagation distances between radar antenna and the scatterers on the ground. An interferometric phase caused by undulating topography profile refers to a phase caused by topographic effect (see Figure 4.10). Topographic effect can be removed by DEM generated by InSAR. However, due to the accuracy of DEM generation, external DEM is usually applied to remove the topographic phase (Tomás, et al., 2005).

- Atmospheric delay

Due to water vapour in the troposphere, propagation delay of the radar signals may occur. In repeat-pass D-InSAR, two radar images are not obtained simultaneously and

atmospheric conditions for the two acquisitions of image pair are different. As a result, there is a phase difference between the two radar pulses. Atmospheric delay can be eliminated by atmospheric water vapour correction (Li, et al., 2009) and the persistent scatterers technique (Hooper , et al., 2013). For the persistent scatterers technique, a sparse grid of persistent scatterers (PS) with stable amplitude and phase are detected in the study area. These PS are characterized as the target with high signal to noise ratio (SNR). SNR is a ratio of the signal power to the noise power; the pixel with higher SNR is brighter than the one with lower SNR. Phase error of the interferogram caused by the atmospheric effect is strongly spatially correlated between the stack of interferograms. As a result, high-pass filtering in time and low-pass filtering in space can be carried out to estimate the atmospheric phase and remove the atmospheric effect (Hooper, et al., 2004).

- Orbit error

Orbit error caused by inaccurate position of the radar orbit leads to errors in ground deformation result (Ferretti, et al., 2007). Both the baseline between radar antennas and the look angle of the radar contribute to the flat earth phase and the topographic phase. Precise radar orbit data can ensure the estimation of the baseline and the look angle, and the removal of the phase caused by flat earth and topography effects from the interferogram.

Orbit error can be eliminated by the adoption of precise orbit data. Delft University of Technology provides precise orbit determination for the ERS and Envisat satellites (Delft University of Technology, 2014).

- Random noise

Random noises include thermal noise of the radar system, noise resulting from variable scattering within the pixel, errors in radar image coregistration, etc. (Ferretti, et al., 2007). It can be reduced by adopting multi-looking and filtering (Balzter, 2001). Lee and his colleagues worked on the relationship between the standard deviation of the noise and the number of looks (Lee, et al., 1994). Speckle noise can be eliminated by generating a multi-looking image. The number of looks is defined by the number of partitioned beam widths which refers to the number of images captured by the radar at the same time. However, the azimuth resolution of a multi-looking image is

reduced while eliminating the speckle noise (Moreira, 1991). In addition, noise of the interferometric phase can be reduced by Goldstein filtering (Goldstein & Werner, 1998) and Lee filtering (Lee, et al., 1994).

2.8 Ground Deformation Monitoring by PS-InSAR

Pairs of radar images used for D-InSAR are captured by spaceborne radar at different times. Due to the long time interval between the image pair acquisitions and the long baseline between the radar antennas, temporal coherence and spatial coherence of the interferogram created from the image pair are low, which results in decorrelation of the interferogram. Decorrelation of the interferogram not only results in phase noises but also leads to discontinuous stripes on the interferogram and difficulty in phase unwrapping (Ferretti, et al., 2001) (Strozzi, et al., 2001).

In order to obtain a more robust ground deformation result, an interferogram with good coherence is required. Range for the coherence of the interferogram is between 0 and 1, where 0 indicates that the interferogram is completed decorrelated while 1 represents that a robust deformation result can be extracted from this interferogram. Generally, interferogram with a coherence index between 0.5 and 1 is considered to be able to generate a differential interferogram for accurate ground deformation monitoring (Suksmono & Hirose, 2002). PS-InSAR was developed as an enhanced D-InSAR technique to overcome the decorrelation of the interferogram in D-InSAR.

Ferretti and his colleagues applied PS-InSAR to mitigate the effects of low temporal coherence and the atmospheric delay in 2000 (Ferretti & Rocca, 2000). Only PS with more stable ability of radar backscattering are selected in PS-InSAR. For instance, PS can be the roof or the corner of buildings and the bare rocks. The PS pixel has stable amplitude and phase in the interferogram and has good coherence even over a long time interval. As a result, more interferograms with good coherence can be generated and the reliability of the D-InSAR result is improved. In repeat-pass D-InSAR, coherence of the interferogram created from the radar image pair is low if the baseline between the two acquisitions of the image pair is longer than the critical baseline. The stable scattering characteristic of the PS ensures a good coherence of the interferograms even though the baseline between the two radar antennas is long (Ferretti, et al., 2001).

PS-InSAR is able to generate a stack of differential interferograms which represent the ground deformation results at different time intervals. Accordingly, time series analysis of the PS pixel in the interferogram can be carried out (Tizzani, et al., 2007). Ferretti and his colleagues estimated a nonlinear subsidence rate with PS-InSAR in 2000 (Ferretti, et al., 2000). PS-InSAR was also applied to measure land subsidence along Jingjin High Speed Rail by Ge et al. in 2009 and a time series analysis of land subsidence was conducted based the result of PS-InSAR (Ge, et al., 2009).

2.9 PS-InSAR in Railway Subsidence Monitoring

2.9.1 SNCF High Speed Rail Network

PS-InSAR was applied to measure subsidence of the SNCF[3] high speed rail network. In order to ensure the reliability of PS-InSAR results, historical levelling survey data or GPS data which record deformation history of the selected railway line are applied to calibrate PS-InSAR results. Standard deviation of the levelling survey results and PS-InSAR results can be used to assess the monitoring result.

In subsidence monitoring of the SNCF network, historical levelling survey data were used to validate the PS-InSAR results. It was identified in the validation that PS-InSAR can produce subsidence monitoring results with an accuracy of 4 mm. SNCF plans to monitor the subsidence of more railway lines using PS-InSAR to find the areas with more serious subsidence problems in their network (Altamira Information, n.d.)

2.9.2 Jubilee Extension Line in London

Ground subsidence may occur during underground tunneling projects. Tele-Rilevamento Europa (TRE) utilised PS-InSAR in ground subsidence monitoring of the Jubilee Extension Line Tunnel Project. Figure 2.9 indicates the annual average deformation velocity of the Jubilee Extension Line (the white arrow). Tunneling work on this extension line was carried out during the 1990s and completed in 1999. Based on the SAR images captured by ERS satellite from May 1992 to Dec 2000, a ground deformation velocity map of the Jubilee Extension Line was generated (TRE, 2011).

[3]SNCF is French National Railways

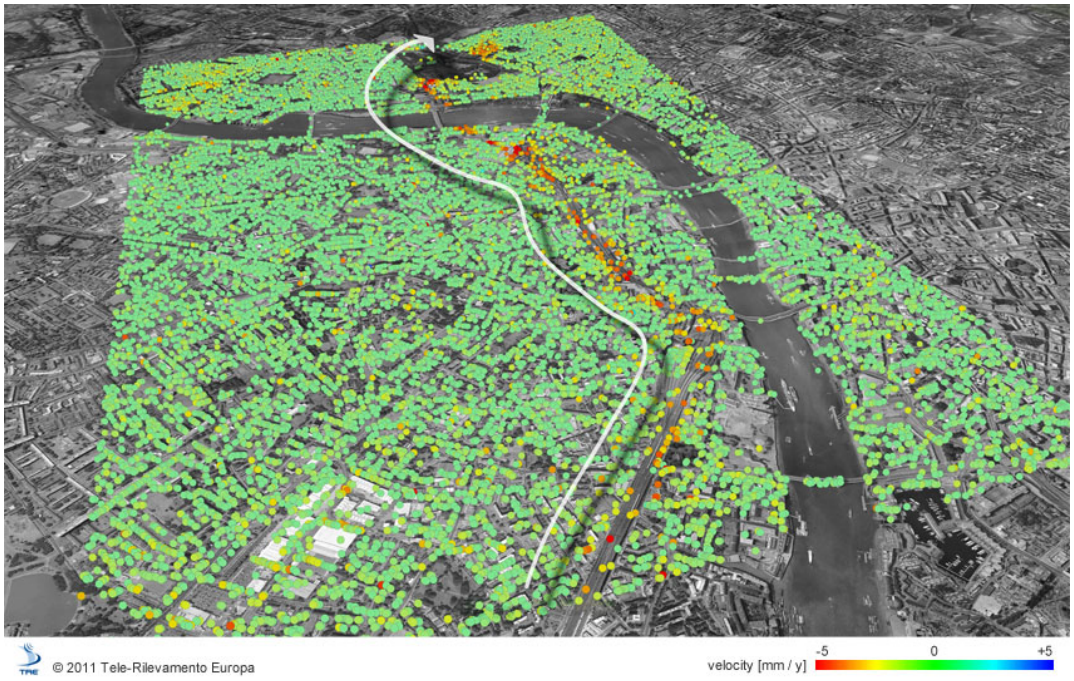

Figure 2.10: Ground subsidence velocity map of the Jubilee Extension Line in London

In the ground deformation velocity map, PS in red represents the area subsided up to 5 mm per year during the Jubilee Extension Line tunneling project.

2.9.3 Jinshan Railway in China

PS-InSAR has been widely implemented in railway subsidence monitoring in China and most of the applications indicate good coherence with the precise leveling measurement results. For instance, Ge and his colleague measured land subsidence of the Jingshan Railway in China by PS-InSAR based on Envisat ASAR images in 2008 (Ge, et al., 2008).

Figure 2.10 represents a velocity map of the land subsidence along the Jingshan Railway in 2004. The red rectangle indicates the monitoring area while the purple line represents the Jingshan railway line. According to the PS-InSAR result, the velocity of land subsidence along this railway line is up to 83.8 mm per year.

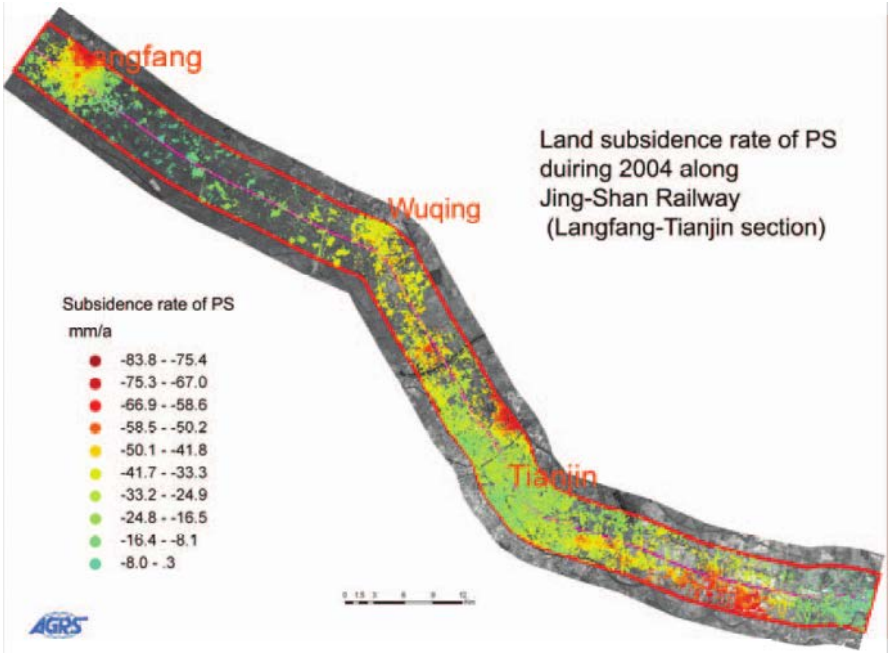

Figure 2.11: Land subsidence velocity map of Jingshan Railway in 2004

In order to verify the reliability of the PS-InSAR result, leveling measurement results obtained from 74 leveling benchmarks were used to compare with the PS-InSAR results. Standard deviation between the leveling survey and PS-InSAR results is 4.6mm, which indicates good agreement between the two results. As a result, it can be concluded that reliability of PS-InSAR in railway subsidence monitoring is acceptable.

2.10 Summary

InSAR is a technique to produce a radar interferogram from a pair of radar images, and extract information of ground deformation from the interferogram. This chapter described the development and applications of InSAR, and satellites which offer radar images for InSAR processing were reviewed.

If ground deformation occurs during the acquisitions of the image pair, D-InSAR is applied to remove topography information and extract real ground deformation. Based on the number of radar images used in differential interferometry, three categories of D-InSAR were reviewed and two-pass D-InSAR was selected in this research. In order to eliminate the limitations of D-InSAR, PS-InSAR, which is able to provide a more robust ground deformation result and conduct a time series analysis of ground deformation, was introduced. PS-InSAR has been applied in railway subsidence

monitoring of the SNCF High Speed Rail Network in France, the Jubilee Extension Line in London and the Jinshan Railway in China.

Chapter 3 Review of Railway Subsidence Prediction

3.1 Introduction

A time series is a collection of observations which are recorded over a specific period. According to the frequency at which the observations are made, it can be divided into discrete time series and continuous time series (Brockwell & Davis, 2002). The ground deformation data analysed in this thesis belong to discrete series, as they were recorded at certain intervals discretely.

One major purpose of time series analysis is to predict the future trend of the time series. After decades of the research, various mathematical models have been developed to produce such predictions. In this chapter, the major types of time series models will be reviewed, which include not only traditional statistical models that have been developed for decades but also those inspired by new technologies or theories in recent years.

In addition, this section will also present practical cases where the models mentioned above were utilised in studies of ground subsidence (Zhang, et al., 2011) (Yang, et al., 2009) (Tang, et al., 2007) as well as tunnel surface subsidence (Suwansawat & Einstein, 2006). It has been demonstrated that these techniques perform well in simulating historical subsidence and are also able to produce reliable predictions of future subsidence development.

3.2 Time Series Prediction Model

In general, time series prediction models can be divided into parametric and non-parametric models, depending on whether the prediction model is pre-determined by certain parameters. Moving average (MA), auto-regressive (AR), auto-regressive moving average (ARMA), decomposition analysis (Shiskin, 1958) and Box-Jenkins analysis (Box & Jenkins, 1976) can be considered as typical parametric models. In

terms of mathematical theories applied, all the models mentioned above have a common feature that they are developed based on statistical methodologies.

In the last 20 years, in the aftermath of information technology development, artificial intelligence has been gradually utilised in time series analysis and models such as artificial neural network (ANN) models have been developed based on this technology (Quah & Srinivasan, 1999) (Rabiner, 1989) (Azoff, 1994). Compared to statistical models, ANN models have better performance when dealing with non-linear relationships. Furthermore, in the early 1980's, grey system theory was introduced by Deng (Deng, 1982). It is capable of handling time series that have a limited number of observations and contain unknown parameters and inter-relationships. There are also a few other time series prediction approaches including fuzzy system (Stepnicka, et al., 2009), support vector machines (Thissen, et al., 2003) etc., which are widely used in various sectors.

3.2.1 Statistical Models

(1) Component analysis

Regardless of mathematical technique and the complexity of statistical models applied in the time series prediction, component analysis mainly focuses on four key components of the time series, namely level, trend, seasonality and noises (Mentzer & Moon, 2005). The goal of the statistical analysis is to determine the level, trend and seasonality features of a time series.

Level is usually described with different forms of average, which reflect the central tendency of the historical time series data. The simplest measure of level is the arithmetic mean. If the time series is relatively stable over a certain period and only havs small movements around a fixed point, as shown in Figure 3.1, the future development can be forecasted using the arithmetic mean of the historical data:

$$F_{n+1} = \sum_{t=1}^{n} S_t \ /n \tag{3.1}$$

Where,

F_{n+1}: forecast value for the next period;

S_t: historical data at the period t;

n: the number of historical data.

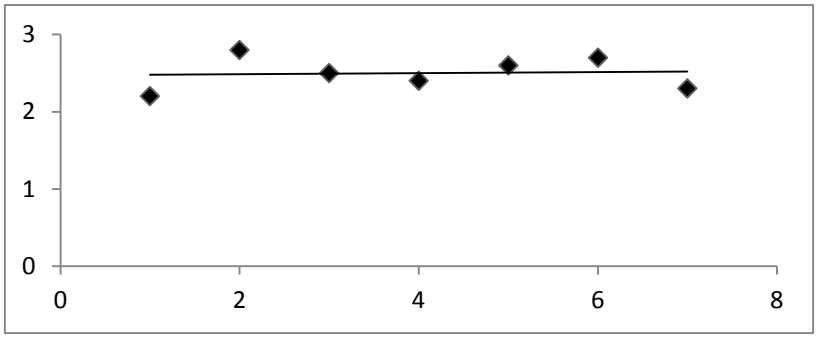

Figure 3.1: Level only time series

The advantage of this measure is that it is usually quite straightforward to calculate and it also removes the effect of fluctuations. However, when the time series is not stable with small level changes, the performance of the average-based forecast can be quite poor (Mentzer & Moon, 2005). In order to dampen out the prediction errors resulting from the instability and fluctuation of the time series, moving average was introduced, which is the average of the time series data in a previous fixed period (Jones, 1966).

$$F_{n+1} = \sum_{t=n+1-i}^{n} S_t / i \tag{3.2}$$

Where,

i: the selected periods which is also known as the selected 'window'.

Compared to simple average which basically gives the same weights to all the historical data, moving average only considers the data captured in the selected window as the indicator for the forecast. Apparently, moving average based prediction can better reflect the recent development of the time series. However, as the selection of the size of the window is quite subjective, there is no absolute benchmark to assess whether the selected window is optimal or not. When the window size becomes larger, the moving average gets closer to the simple arithmetic average. On the contrary, when only one period is chosen for the moving average calculation, it basically assumes the last period as the best forecast for the next period (Mentzer & Moon, 2005). In order to address the issues of moving average and establish a more systematic way of assigning weightings to the previous periods, a technical method, such as exponential smoothing which gives more emphasis on the most recent data (Jones, 1966), is introduced.

$$F_{t+1} = \alpha S_t + (1-\alpha)F_t \quad (3.3)$$

Where,

S_t: actual data at the period t;

F_t: forecast value for the period t;

α: weighting for the estimation (between 0 and 1).

When the time series does not stay at its current level and switches to other levels continuously, trend is brought into the prediction model to reflect the level changes. In general, trend can be considered as the difference between the two levels:

$$T_t = L_t - L_{t-1} \quad (3.4)$$

Where,

T_t: trend at the period t;

L_t: level at the period t.

Similar to the estimation of level, exponential smoothing can also be applied to estimate trend (Mentzer & Moon, 2005):

$$T_{t+1} = \beta(L_t - L_{t-1}) + (1-\beta)T_t \quad (3.5)$$

Where,

T_{t+1}: forecast trend for the next period;

$L_t - L_{t-1}$: actual trend at the period t;

T_t: forecast trend in the period t;

β : weighting for estimation (between 0 and 1).

Apart from level and trend, some time series also reveal significant seasonal patterns. For instance, the subsidence of the subgrade in plateau during winter and summer can vary materially. There are two main methods to adjust for seasonality, namely additive seasonal adjustment and multiplicative seasonal adjustment:

$$F_{t+1} = S_t + SA_{t-Z} \text{ (Additive)} \quad (3.6)$$

$$F_{t+1} = S_t / SA_{t-Z} \text{ (Multiplicative)} \quad (3.7)$$

Where,

F_{t+1}: forcast seasonality for the next period;

SA: seasonal adjustment;

Z: the length of the seasonal cycle.

Combining the estimation of level, trend and seasonality together, the forecast of the time series can be made as follows:

$$F_{t+1} = \alpha(S_t/SA_{t-Z}) + (1-\alpha)(L_{t-1} + T_t) \quad (3.8)$$

Where,

F_{t+1}: forcast data for the next period;

St/SA_{t-Z}: actual data at period t;

$L_{t-1}+T_t$: forcast data for the period t.

(2) Auto-regressive moving average

Among various statistical models which were built up based on the rationale introduced above, auto-regressive moving average (ARMA) is one of the most prevailing methodologies. It is a combination of two models including the auto-regressive (AR) model and moving average (MA) model. The AR model assumes that the prediction of the time series can be produced based on a finite number of previous observations:

$$S_t = c + \sum_{n=1}^{p} \gamma_n S_{t-n} + \varepsilon_t \quad (3.9)$$

Where,

S_t: forcast value for the period t;

c: a constant;

p: number of historical periods involved, also known as the order of the AR model;

γ: parameters;

S_{t-n}: actual data for the period t-n;

ε_t: white noise at the period t, which is stationary and has expected value of 0.

Similarly, a MA model tries to estimate the future movements of the time series based on the average of the time series together with random noises during selected previous periods. The number of periods selected is known as the order of the MA model.

$$S_t = \mu + \varepsilon_t + \sum_{n=1}^{q} \theta_n \varepsilon_{t-n} \quad (3.10)$$

Where,

μ: the mean of the time series (a constant);

ε_t: white noise at period t, which is stationary and has expected value of 0;

q: number of historical periods involved, also known as the order of the MA model;

θ: parameters;

ε_{t-n}: white noise at period t-n, which is stationary and has expected value of 0;

When considering both the AR and MA in the time series prediction model, it becomes auto-regressive moving average model (ARMA). The model ARMA (p, q) can be structured as follows (Brockwell & Davis, 2002):

$$S_t = c + \varepsilon_t + \sum_{n=1}^{p} \gamma_n S_{t-n} + \sum_{n=1}^{q} \theta_n \varepsilon_{t-n} \quad (3.11)$$

In the equation above, the AR part represents the impact of historical time points on the current period, while the MA part can be considered as random fluctuations / shocks in the past. The ARMA model is particularly suitable for a time series which is not only influenced by historical movements but also hit by unexpected shocks. The most critical part for an ARMA model is to decide its orders, i.e. the values of p and q respectively. Since the ARMA model was firstly introduced by Wold in 1938, which described ARMA model theoretically (Wold, 1938), mathematicians have developed various methodologies to calculate and choose the order of the model. The most popular method was introduced by Box and Jenkins (Box & Jenkins, 1970) in 1970, which significantly facilitated the utilisation of ARMA model and made it feasible to apply the ARMA model to real world data. The main elements of Box and Jenkins approach are (Makridakis & Hibon, 1997):

- Proposing methods of transforming non-stationary time series to stationary series
- Using autocorrelation and partial autocorrelation to determine optimal values of p and q for the model
- Providing computer programme-based modules to estimate the parameters of the model
- Examining and optimising both the values of p and q as well as the parameters

The ARMA model constructed through the Box-Jenkins methodology is known as the auto-regressive integrated moving average (ARIMA) model, which has become one

of the most popular prediction models for time series. The ARIMA model can be interpreted as ARIMA (p, d, q), where p and q have the same definition as in the ARMA model. The additional d represents the number of differencing that the time series needs to make in order to be stationary.

3.2.2 Artificial Neural Network

An artificial neural network (ANN) is a computer-based model inspired by the natural neural system in animal's brain and the way in which the neural system deals with the information. Human's understanding on the world is through a process of learning and recognition. During this process, when information is received by the brain, it may be decomposed into elements each of which will be handled by specific neurons according to their respective functions. Then based on outputs produced by each neuron and the interactions among neurons, a global action and recognition will emerge. ANN tries to mimic the information processing procedure of the natural neural system by creating artificial neurons that can perform similar but highly abstracted tasks. Each artificial neuron is a computational module, which is usually comprised of four components, inputs, weights, activation function and outputs respectively (Gershenson, 2003). ANN was firstly introduced by McCulloch and Pitts in 1943, when they described the procedure of human brain's recognition on complex information through the cooperation among neurons (McCulloch & Pitts, 1943). In their paper, a simple neuron model was also introduced, which became the basis of numerous artificial neuron network models developed later. As the output of an artificial neuron is determined by the activation function, which is further based on inputs and their corresponding weights, the most critical part of an ANN model is to decide weights of each neuron.

Since the ANN was introduced, various algorithms have been developed to learn and adjust weights automatically based on the historical data. Gradient descent backpropagation is one of the most widely utilised algorithms, which enables the ANN to optimise input weights in order to minimising output errors (Rumelhart & McClelland, 1986). According to the gradient descent backpropagation algorithm, ANN is structured with layers, including the input layer and output layer as well as hidden layers if there are more than two layers. In the simplest 2-layer ANN, neurons

on the input layer receive data and pass them to neurons on the output layer, which will then produce output through the activation function based on inputs and their weights. The whole process can be illustrated in Figure 3.2.

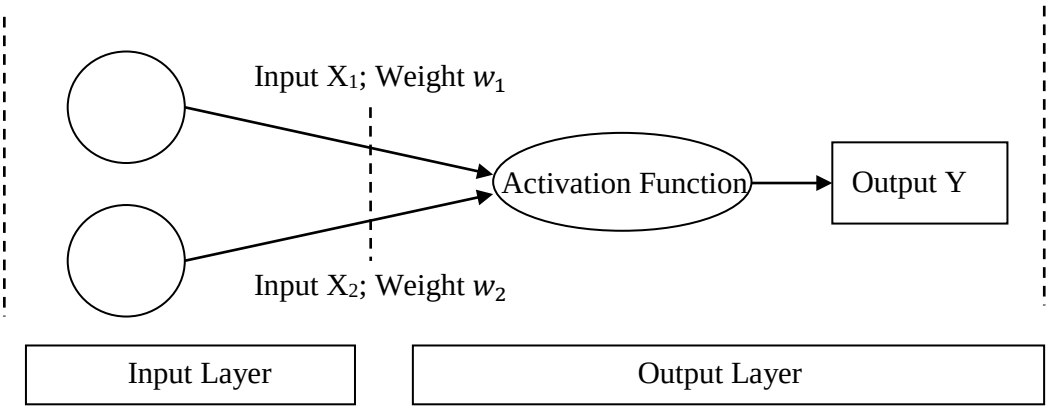

Figure 3.2: Structure of the neural network

Apart from gradient descent backpropagation algorithm, other frequently applied algorithms also include Levenberg–Marquardt back propagation, Genetic algorithm etc (Ghaffari, et al., 2006). Due to its adaptability in dealing with various data types and relationships, ANN has become one of the most effective approaches to machine learning and pattern recognition in many fields.

3.2.3 Grey Model

Grey system theory was firstly introduced by Deng in 1982 (Deng, 1982). It aims to analyse systems with unknown parameters and estimate their movements accordingly. During the past 20 years, grey system theory has driven significant attentions in both the academic area and the practical fields.

In terms of transparency, systems can be divided into 3 categories, namely black system, white system and grey system. If parameters and their relationships are not known in a system, the system is called a black system or black box. On contrary, if all information is known and transparent in a system, the system is defined as white system. When a system's status is between the black and a white systems, i.e., only a portion of the information is known, it is a grey system (Deng, 1982). Due to the lack of transparency in grey system with unknown parameters, it is usually difficult to

utilise parametric statistical models to describe the behaviour of the grey system. The grey system theory is thus developed to (Deng, 1989):

- Establish alternative process instead of statistical analysis to understand grey system
- Transform the original raw grey data to a more structured series for modeling purpose
- Introduce grey model to describe the movements of grey system and make predictions on the future status

The grey model can be described as GM (m, n), where m is the order of differencing and n represents the number of parameters in the model. The most basic and important grey model is GM (1, 1), which use the first order differencing and have only 1 parameter (Deng, 1989). The differencing it implements is Accumulated Generating Operation (AGO), which is defined as (Deng, 1989):

$$x_k^{(1)} = \sum_{i=1}^{k} x_i^{(0)} \tag{3.12}$$

Where,

$x_k^{(1)}$: the transformed data at time k;

$x_i^{(0)}$: the raw data at time i.

Through AGO, the original grey data can be transformed to a series with more dependency between data points, which is then suitable for modelling and forecasting. Apart from GM (1, 1), other grey models have been also established, resulting from a combination of grey system theory and other system-describing theories. These models include the grey Verhulst model (Wen & Huang, 2004), grey fuzzy model (Huang & Huang, 1996), and support vector regression grey model (Chang & Tsai, 2008).

3.2.4 Comparisons between Time Series Prediction Models

Statistical models, ANN models and grey models have all been approved to be successful in describing and predicting time series. However, as the time series data in the real world vary significantly in terms of type, volume, frequency etc., the accuracy of these models is highly dependent on the characteristics of the target data.

As the most widely used model in statistical analysis on time series, ARIMA tries to describe time series with pre-determined modelling structure, i.e. linear regression and/ or moving average. With the Box-Jenkins methodology which can assist in determining the orders of the model, ARIMA is quite flexible in modelling different types of time series based on auto-regression on past data, moving average of previous data or a combination of auto-regressive and moving average (Zhang, 2003). However, when the time series reveals certain non-linear pattern, the accuracy of ARIMA drops. In the real life, most of the data series are not purely linear (Aslanargun, et al., 2007). Thus, it is not always sufficient to use only ARIMA to describe the time series.

Compared to ARIMA, ANN is capable of modelling non-linear time series through its flexible model structure which does not have any fixed form but is derived from the application of the learning function on the data itself, resulting in a much better adaptability in modelling data with different features (Zhang, 2003). Comparisons of performances between ARIMA and ANN have been undertaken in numerous papers. It appears that based on empirical research results, ANN outperforms ARIMA models (Chin & Arthur, 1996) (Kohzadi, et al., 1996) (Prybutok, et al., 2000), particularly in capturing unexpected sudden changes within time series (Chen & Lai, 2011).

Although ARIMA and ANN are still dominating the time series modelling and forecasting, grey models have attracted significant academic attention recently and have been widely implemented in practice. Compared to ARIMA and ANN, grey models have relative strength in the following areas:

- Time series with limited data availability. Both the ARIMA and ANN require large volume of data in order to establish reliable models. However, grey models can still work well with only a few data points (Deng, 1989).
- As grey models always adapt to the new observations available in the time series, it has better performance in real-time prediction than other methods (Kayacan, et al., 2010). Especially for systems with unknown factors or unknown relationships between influential factors, grey models are more robust against noises (Kayacan, et al., 2010).

3.3 Time Series Models in Subsidence Prediction

3.3.1 ARMA Models

As the most prominent time series prediction approach, ARMA has been bought into different types of subsidence modelling and forecasting.

(1) ARMA in mining area subsidence prediction

ARMA was used in land subsidence and movement prediction in a mining area in China. In the project, the autocorrelation function and partial autocorrelation function was firstly applied to confirm the suitability of ARMA model. Then EViews, a statistical research tool, was utilised to estimate the parameters and establish the ARMA model. Movement observations from 2001 to 2010 in the mining area were selected in the simulation. According to the comparison between the results of forecasting estimated from ARMA model and the actual data, ARMA model revealed high accuracy, particularly within short prediction period (Zhang, et al., 2011).

(2) ARMA in railway subsidence prediction

ARMA was also used to predict the ground subsidence during the construction of urban underground railway in China. The raw subsidence data were transformed through the first order differencing in order to produce a stationary time series data. The order of the model was determined by Akaike Information Criterion algorithm, while the parameters of the model were optimised based on least squares method. The model was then adopted to forecast the subsidence of Shenzhen Metro Line 2 in China, which eventually appeared to be reliable in the subsidence prediction (Yang, et al., 2009).

3.3.2 Artificial Neural Network

Since the development of most subsidence is usually non-linear, an Artificial Neural Network (ANN) approach has become widely used in this field.

(1) Prediction of maximum surface subsidence resulting from earth pressure balance (EPB) tunnelling in the Bangkok Mass Rapid Transit Authority (MRTA) project

A multiple-layer neural network model was employed for subsidence prediction, which consists of 1 input layer, n hidden layers and 1 output layer. Factors which have an impact on the settlement were categorised into 3 main classes, namely tunnel geometry, geological conditions and shield operation factors. There were 2 factors in tunnel geometry, 3 factors in geological conditions and 5 factors in shield operation. Therefore the input layer was comprised of 10 neurons which corresponded with the 10 factors. The output layer only contains 1 neuron which produced the predicted maximum subsidence caused by EPB. The classical backpropagation algorithm was used to determine the weights for each neuron.

The sample data included the subsidence data of the 20 km of twin tunnels in Bangkok, which were further divided into the training set and the validation set as per the standard practice in time series prediction. In order to decide the number of hidden layers and neurons on each hidden layer, the project established 18 different structures of ANN, varying in terms of numbers of hidden layers, nodes on each hidden layer and data points used in the training set. Root mean square error (RMSE) was used to assess the performance of these models. After the models were tested both with the train set and validation set, the RMSE suggested that the neural network model with 1 hidden layer and 20 neurons in the hidden layer performed the best and the optimal number of data points for the training set was 2,000. Finally, the selected model was implemented for the whole tunnel and it was concluded that the ANN model was capable of producing reliable prediction of the surface subsidence for the project (Suwansawat & Einstein, 2006).

(2) Railway track deterioration prediction with ANN

In the railway industry, a research by the Turkish State Railways used ANN in forecasting railway track geometry deterioration where subsidence is one of the major influential factors. In the study, the ANN model was a multi-layer one which had 4 layers, including 2 hidden layers. The input layer contained 12 neurons, representing 12 inputs that can be grouped into 4 categories, i.e. load factors, material factors, soil factors and environmental factors. Among these factors, five were quantitative variables, such as traffic loads, speed, curvature, gradient and cross level, while others were qualitative variables, including sleeper type, rail type, rail length, falling rock,

land-slide, snow, and flood. All the qualitative variables were described with dummy values, i.e. 1 or 0. Two hidden layers had 8 and 6 neurons respectively and were activated with a hyperbolic tangent function. The final output was the deterioration rate.

The sample data were selected from observations on 820 segments on a 180 km railway between Arifiye and Eskisehir in Turkey from 2009 to 2011. The ANN model was identified and assessed through a SPSS package. According to the modelling results, the study found that the ANN model had a solid performance in predicting the track deterioration rate, provided that R^2 (coefficient of determinations) for all parameters was above 70%. It was also concluded that the ANN model had significant potential for assisting maintenance and repair planning (Guler, 2013).

3.3.3 Grey Theory based Prediction

In the real world, subsidence data are sometimes not sufficient enough for statistical analysis or ANNs modeling. In these situations, a grey model is an effective alternative approach, which requires much less data and does not need to identify all key factors in order to develop the prediction model.

A study on land subsidence in Shanghai used the GM (1, 1) to estimate the land subsidence around a skyscraper in the Lujiazui Area. As it was relatively difficult to monitor the land subsidence for a long period and there were various factors which contributed to the subsidence, the available data for modeling were quite limited and had different intervals between observations. Therefore, the study made further transformation on the raw data by using the average interval between observations, changing the raw data points into a new time series with equal time interval, which could then be modeled with the standard GM (1, 1). After a comparison between the prediction results from GM (1, 1) and the actual subsidence data, as well as the prediction produced by the adaptive neuro-fuzzy inference system (ANFIS), which was another widely used approach in subsidence forecasting, the study concluded that the GM (1, 1) can produce reliable forecasts with similar accuracy as the ones made by ANFIS, while the GM (1, 1) requires much less data volume. However, the performance of GM (1, 1) was much better in a short period, indicating that the model should continuously be adjusted and re-established with the newly available data

being incorporated to replace old data, in order to ensure the accuracy of the model (Tang, et al., 2007).

3.4 Summary

As described above, due to the importance of railway subsidence monitoring, time series techniques have been widely applied in this field. The main time prediction models include ARMA which is based on traditional statistical theories, artificial neural network models inspired by artificial intelligence and a grey model which is derived from system theory.

There is no approach that is definitely superior to others. Each of them has their relative strength in a particular area. Generally speaking, ARMA is more suitable for time series with large data volume and clear developing trend, while artificial neural network performs well when there are fewer observations with an un-linear trend. Compared to these two approaches, a grey model requires the least volume of data and specifically works for systems with partially unknown parameters. At the end of this section, a few practical cases were given with regard to the application of time series models in subsidence prediction, which include the utilisation of an ARMA model in the subsidence monitoring of a mining area in China, the neural network model in tunnel surface subsidence detection in Bangkok and the grey model in land subsidence around a skyscraper in Shanghai. All of these projects have been proved to produce satisfactory performance in subsidence prediction and can therefore provide significant support in future maintenance planning and scheduling as well as safety assessment in subsidence-related areas such as the railway industry.

Chapter 4 Railway Subsidence Monitoring with InSAR

4.1 Introduction

Interferometric Synthetic Aperture Radar (InSAR) has been widely applied in various research areas, such as topography mapping, DEM (Digital Elevation Model) generation, ocean currents mapping and landscape deformation measurement. In this chapter, the author aims to introduce the methodology of InSAR to railway subsidence monitoring.

Firstly, the difference between Real Aperture Radar (RAR) and Synthetic Aperture Radar (SAR) will be discussed. Following a description of the principle of SAR, the principle of DEM generation by InSAR is provided. In order to measure real ground deformation which has occurred over a long time period, D-InSAR (Differential InSAR) is applied. This chapter describes the principle of D-InSAR and the main procedures for D-InSAR processing. Lastly, as an enhancement of D-InSAR, the process of PS-InSAR, which is able to obtain more robust ground deformation results, is introduced.

4.2 Real Aperture Radar

In order to obtain topography and deformation information for a landscape, two or more images captured by a radar system are required (Lu, et al., 2007). There are two radar systems which can be used for the acquisition of radar images, which are Real Aperture Radar (RAR) and Synthetic Aperture Radar (SAR).

4.2.1 Principle of Real Aperture Radar Operation

The principle for the acquisition of radar images by RAR is presented in Figure 4.1. A radar antenna transmits a beam of microwave pulses to the ground at regular intervals and illuminates a footprint of the beam on the ground. The radar pulses are then

backscattered from scatterers on the ground to the same radar antenna, which are then recorded by the radar antenna (Bamler & Hartl, 1998). The moving radar system continuously transmits beams of radar pulses to the ground and illuminates a wide swath on the ground, which presents the area imaged by the radar.

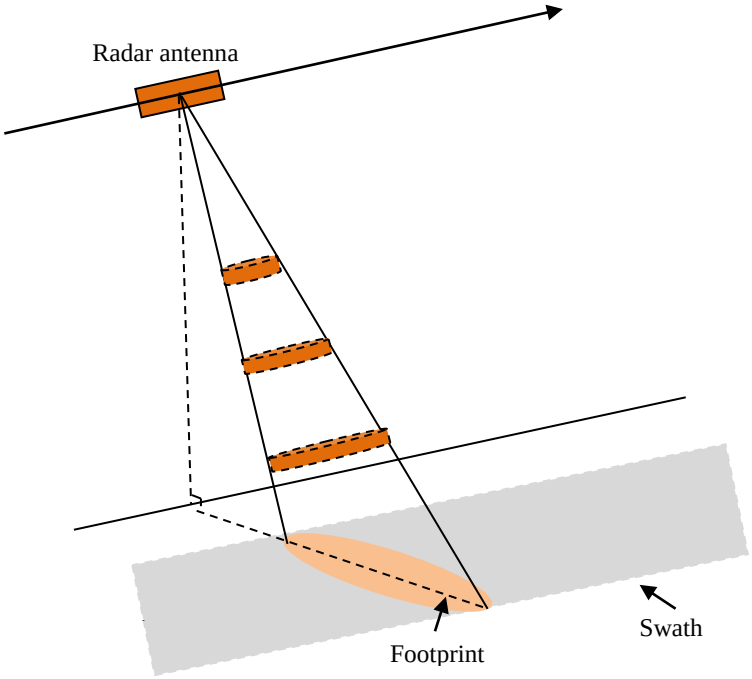

Figure 4.1: Principle of radar imaging

The image captured by the radar indicates the reflectivity of the illuminated ground and records amplitude and phase of the radar echo. The topography of the landscape, such as ground slope and roughness of the ground surface, affects the amplitude and phase of the radar echo.

4.2.2 Resolution of Radar Image

The radar image can be considered as a mosaic consisting of image pixels which are arranged in rows and columns (Ferretti, et al., 2007). Each pixel represents a resolution cell of the radar image and the size of the pixel indicates the ground resolution of the image, which enables targets to be distinguished targets in the image.

For instance, two scatterers on the ground cannot be discriminated on the radar image if they are captured in the same image pixel.

In addition, each resolution cell of the radar image indicates an area on the ground. The topography of this area is represented by the terrain slope in the azimuth direction and the terrain slope in the ground range resolution. The azimuth direction is the direction along the track parallel to the direction of the movement of the radar, while the ground range direction refers to the across track direction, perpendicular to the direction of radar movement.

As pixels of the radar image are arranged in rows and columns, rows and columns of the image refer to azimuth locations and ground range locations respectively. Accordingly, azimuth resolution and ground range resolution contribute to the ground resolution of the radar image. The ground range resolution is the projection of the spatial resolution which is the resolution in the slant range direction (see Figure 4.3). The slant range direction is the Line of Sight (LOS) direction, which connects the radar antenna and the scatterer on the ground.

The resolution of the radar image is then represented by the slant range resolution, ground range resolution and azimuth resolution (Chen, et al., 2000) and it depends on the radar pulse duration T, look angle θ, the elevation of the radar antenna H and width of radar antenna L (Ferretti, et al., 2007) (see Figure 4.2).

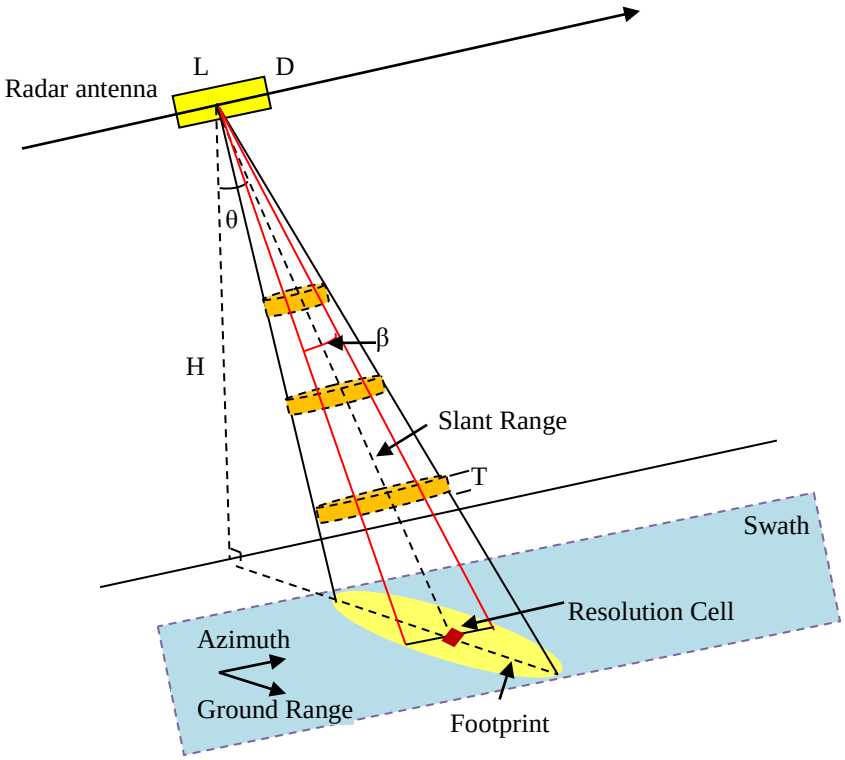

Figure 4.2: Geometry of real aperture radar

(1) Slant range resolution

The slant range resolution is the capability to distinguish between scatterers in the slant range direction (see Figure 4.3). Due to the out and back propagation of the radar pulse, the pulse duration should be divided by two (McCandless & Jackson, 2004).

$$\Delta R = \frac{CT}{2} \tag{4.1}$$

Where,

ΔR: slant range resolution;

C: speed of light (300,000 km/s);

T: pulse duration (shown as a time).

(2) Ground range resolution

The ground range resolution is the capability to distinguish scatterers in the ground range direction and it is the projection of the spatial resolution.

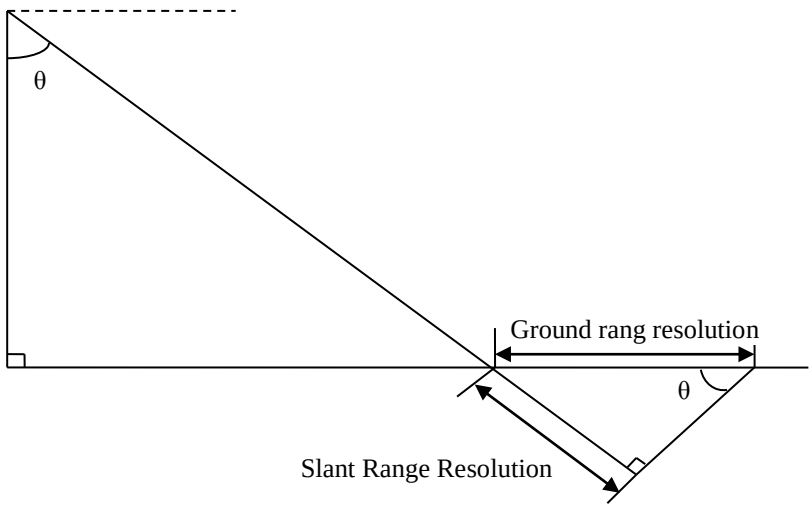

Figure 4.3: Relationship between slant range resolution and ground range resolution

Accordingly, the ground range resolution can be calculated by dividing the slant range resolution by the sine of the look angle.

$$\Delta Y = \frac{\Delta R}{\sin\theta} = \frac{CT}{2\sin\theta} \tag{4.2}$$

Where,

ΔY: ground range resolution;

θ: look angle of the radar.

The ground range resolution ΔY is only affected by the look angle θ. The smaller the look angle, the worse the ground range resolution of the radar image. As a result, the radar antenna must fly with a side looking angle.

(3) Azimuth resolution

The azimuth resolution represents the capability to distinguish scatterers in the azimuth direction. The dimension of the azimuth beam width at any range determines the azimuth resolution at the corresponding range (Cutrona, et al., 1966). The azimuth beam width of the radar is determined by the ratio of the radar wavelength and the along-track antenna length of the radar (Xia, 2010) (Ulady, et al., 1986) (see Figure 4.2). Accordingly, the azimuth resolution is calculated by the equation below (McCandless & Jackson, 2004).

$$\Delta X = R\beta = \frac{R\lambda}{L} = \frac{H\lambda}{\cos\theta L} \tag{4.3}$$

Where,

ΔX: azimuth resolution;

R: slant range;

β: azimuth beam width of radar antenna;

λ: wavelength;

L: length of the radar antenna;

H: elevation of the radar track.

As indicated by the equation 4.3, the azimuth resolution of the radar image can be improved by increasing the length of radar antenna. This is a limitation of the RAR system because the length of the antenna is limited by the space available at the launch time.

4.3 Synthetic Aperture Radar

As stated in Section 4.2.2, the azimuth resolution of a radar image can be improved by increasing the length of the radar antenna. However, a very long antenna is not feasible. Synthetic Aperture Radar (SAR) can be applied to obtain a radar image with a good azimuth resolution by a radar arrangement with a relatively short physical antenna.

Beams of radar pulses are transmitted to the scatterers on the ground from the moving radar antenna and then the radar echoes are backscattered to the same antenna. Due to the relative motion between the radar antenna and the scatterer on the ground, there is a frequency change of the radar echo, which refers to Doppler Frequency Shift (Bürgmann, et al., 2000). The azimuth resolution can be improved based on the detection of Doppler Frequency Shift. If the echoes from the scatterer on the ground can be recorded continuously by the moving radar antenna, they can be composed into one beam of radar echoes. The composed beam of radar echoes can be considered as the echo is backscattered from the scatterer to a linear array of virtual radar antennas. The linear array of virtual radar antennas refers to the synthetic aperture.

For instance, as shown in Figure 4.4, the radar antenna is transmitting microwave pulses to A on the ground while it is moving along the track from position 1 to position n. Accordingly, radar echoes from A are received by the radar antenna at time 1, time 2, until time n continuously. When the radar is moving along the linear

array L_{sa}, echoes from A can always be observed by the moving radar antenna. Then the echoes are composed into one beam of radar echoes. Synthesized linear array L_{sa} is considered as the azimuth antenna length of the SAR, which replaces the physical length of the radar antenna in the azimuth direction. Thanks to the application of the SAR, the antenna length of the ERS satellite was increased from 10 m to a synthetic aperture of 4 km (Liew, 2001).

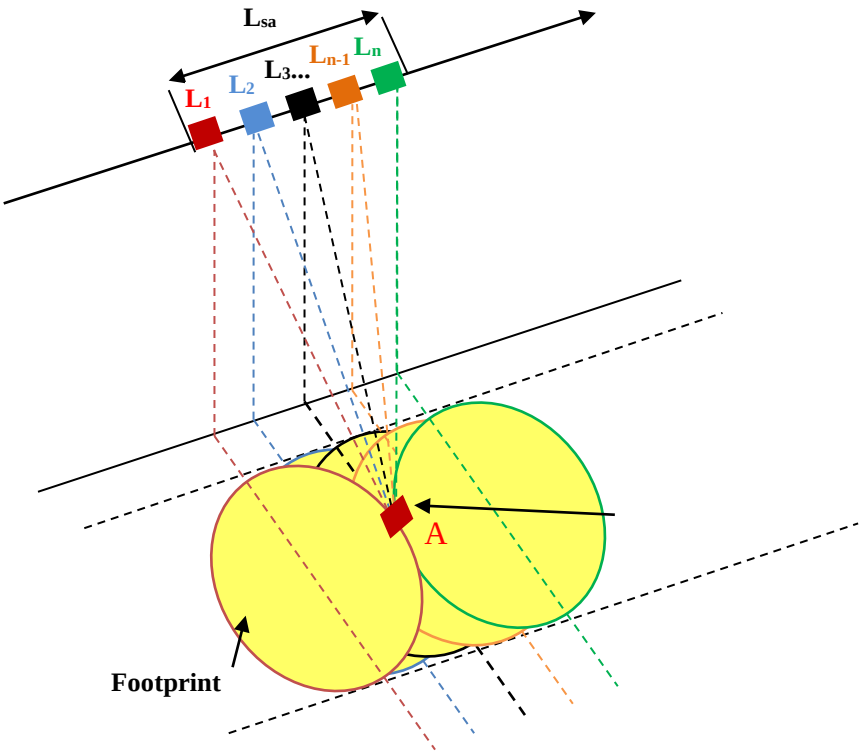

Figure 4.4: Principle of synthetic aperture radar

4.4 DEM Generation by InSAR

SAR images with a good resolution can be used to produce a DEM of the imaged area. Information about the terrain surface can be analysed using the DEM (Perski, et al., 2009). InSAR, a further development of SAR, is a technique used to produce radar interferograms based on a pair of SAR images captured by the two radar antennas mounted on the same satellite, which are used to generate a DEM of the imaged area (see Figure 4.5).

4.4.1 Principle

In Figure 4.5, Radar antenna S_1 and S_2 transmit radar pulses to the scatterer P on the ground and receive different echoes from P. The radar pulse and its echo in a SAR system are recorded as a complex number with amplitude and phase information and can be represented as a pixel of a Single Look Complex (SLC) image. The SLC image refers to a SAR image generated by a synthetic aperture. A synthetic aperture is regarded as a single look.

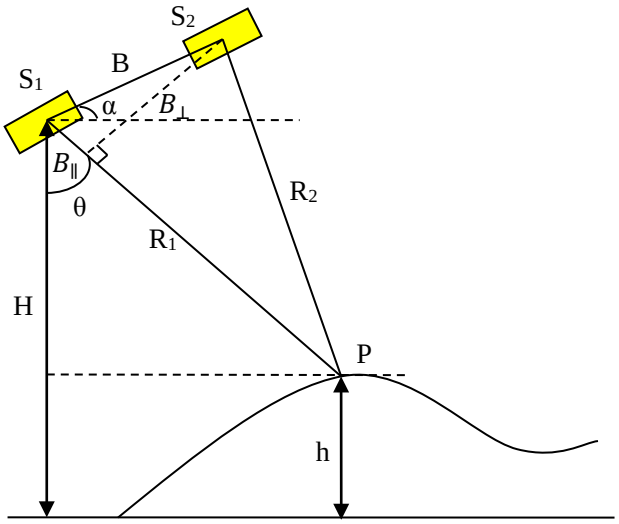

Figure 4.5: Geometry for DEM generation

For radar antennas S_1 and S_2 operating at different elevations, propagation distances R_1 and R_2 of the radar pulses between the two radar antennas and P are different, which induces a phase difference between the corresponding pixels in the two SAR images. $\Delta\varphi$ is assumed as the phase difference of two radar echoes caused by the different radar propagation paths R_1 and R_2.

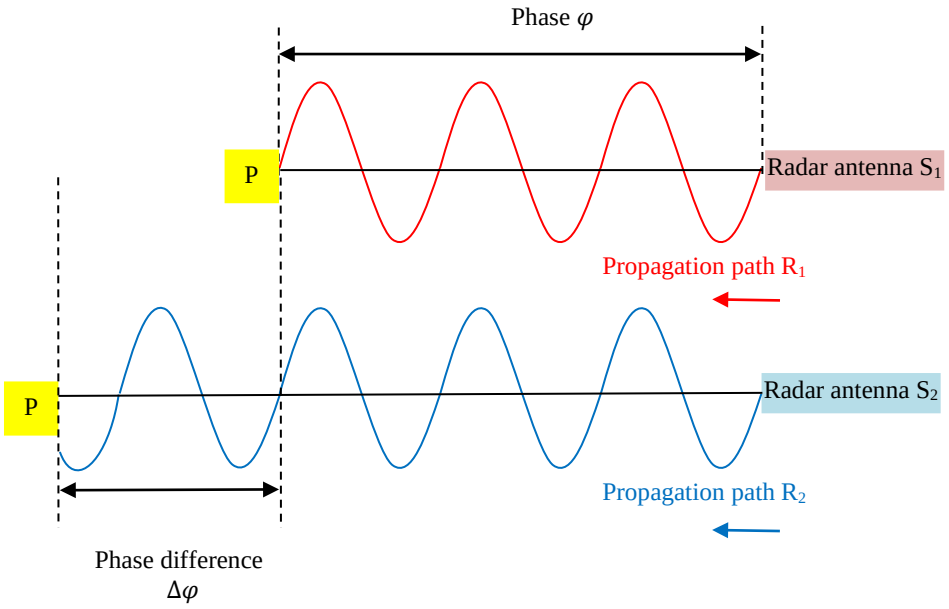

Figure 4.6: Radar propagation path and phase of radar pulse

Due to the phase difference between the corresponding pixels in the SLC image pair, an interferogram can be generated. Based on the interferogram, the DEM of the imaged area can be produced. If ground deformation occurred during the acquisition of the image pairs, the ground deformation can also be extracted from the interferogram.

4.4.2 Phase Difference

In order to generate the DEM of the imaged area and measure the deformation of the scatterers, the phase of the interferogram is measured first. Radar echoes received by the radar antenna are recorded in a complex number format and represented by a SLC image. As a result, each pixel of the SLC image is represented by a complex number with the amplitude and phase information of the radar echo backscattered from the scatterer in the pixel (Ortiz, 2007). The amplitude of the complex number represents the strength of the echo, while its phase indicates the argument of the complex number (Samiei-Esfahany, 2008). For instance, in Figure 4.5, the radar echoes from scatterer P to S_1 and S_2 can be represented by complex numbers $S(R_1)$ and $S(R_2)$ respectively.

$$S(R_1) = A(R_1)e^{[i\varphi(R_1)]} \tag{4.4}$$

$$S(R_2) = A(R_2)e^{[i\varphi(R_2)]} \tag{4.5}$$

Where,

$S(R_1)$, $S(R_2)$: complex number for the radar echo;

$\varphi(R_1)$, $\varphi(R_2)$: phase of the radar echo;

$A(R_1)$, $A(R_2)$: amplitude of the radar echo.

The interferogram is produced pixel by pixel, therefore it is necessary to ensure that the scatterer P is in the corresponding pixels of the two SLC images by coregistration of the image pair (Ferretti, et al., 2007). Coregistration is carried out by multiplying the complex number of radar echo $S(R_1)$ and the conjugate complex number of radar echo $S(R_2)$.

$$S(R_1)S^*(R_2) = A(R_1)e^{[i\varphi(R_1)]}A(R_2)e^{[-i\varphi(R_2)]} \tag{4.6}$$

Where,

$S^*(R_2)$: conjugate complex number of $S(R_2)$.

By the application of coregistration, the amplitude of the interferogram is obtained by multiplying the amplitude of the two echoes, while the phase of the interferogram is the phase difference between the two echoes (Ferretti, et al., 2007).

$$S(R_1)S^*(R_2) = A(R_1)A(R_2)e^{i[\varphi(R_1)-\varphi(R_2)]} \tag{4.7}$$

The phase of the interferogram is the argument of the complex number.

Then,

$$\varphi_p = \arg[S(R_1)S^*(R_2)] = \arctan\left\{\frac{I[S(R_1)S^*(R_2)]}{R[S(R_1)S^*(R_2)]}\right\} = \varphi(R_1) - \varphi(R_2) \tag{4.8}$$

Where,

φ_p: phase of the interferogram;

$\arg[S(R_1)S^*(R_2)]$: argument of the complex number;

$R[S(R_1)S^*(R_2)]$: real part of the complex number;

$I[S(R_1)S^*(R_2)]$: imaginary part of the complex number.

For electromagnetic waves, the propagation length within a cycle is a wavelength λ and the phase of the electromagnetic wave for a cycle is 2π. Accordingly, the phase

difference of the two radar echoes can be obtained based on the propagation length (Ferretti, et al., 2007).

$$\frac{2\pi}{\varphi(R_1)-\varphi(R_2)} = \frac{\lambda}{R_1-R_2} \tag{4.9}$$

Where,

λ: wavelength of the radar pulse;

R_1, R_2: propagation distances from the radar antenna to the target scatterer;

$\varphi(R_1)$,$\varphi(R_2)$: phase of the radar pulse.

Additionally, the propagation of the radar pulse is an out and back journey, therefore the propagation distance of the two radar echoes should be doubled.

$$\frac{2\pi}{\varphi(R_1)-\varphi(R_2)} = \frac{\lambda}{2(R_1-R_2)} \tag{4.10}$$

$$\varphi_p = \varphi(R_1) - \varphi(R_2) = \frac{4\pi}{\lambda}(R_1 - R_2) \tag{4.11}$$

Where,

φ_p: phase difference of the two radar pulses.

4.4.3 DEM generation

According to the geometry of the DEM generation in Figure 4.5 and the phase φ_p represented above, the elevation of the scatterer P can be obtained (Liang, et al., 2012).

$$h = H - R_1 \cos\theta \tag{4.12}$$

Where,

h: elevation of the scatterer P;

H: elevation of the radar antenna S_1.

According to the cosine theorem,

$${R_2}^2 = {R_1}^2 + B^2 - 2R_1 B\cos\left(\frac{\pi}{2} - \theta + \alpha\right) = {R_1}^2 + B^2 - 2R_1 B\sin(\theta - \alpha) \tag{4.13}$$

And,

$$\varphi_p = \frac{4\pi}{\lambda}(R_1 - R_2) \tag{4.14}$$

$$R_2 = R_1 - \frac{\varphi_p \lambda}{4\pi} \tag{4.15}$$

Then,

$$\left(R_1 - \frac{\varphi_p \lambda}{4\pi}\right)^2 = {R_1}^2 + B^2 - 2R_1 B\cos\left(\frac{\pi}{2} - \theta + \alpha\right) \quad (4.16)$$

$${R_1}^2 + \left(\frac{\varphi_p \lambda}{4\pi}\right)^2 - 2 \times \frac{\varphi_p \lambda}{4\pi} R_1 = {R_1}^2 + B^2 - 2R_1 B\sin(\theta - \alpha) \quad (4.17)$$

$$R_1\left[2B\sin(\theta - \alpha) - \frac{\varphi_p \lambda}{2\pi}\right] = B^2 - \left(\frac{\varphi_p \lambda}{4\pi}\right)^2 \quad (4.18)$$

$$R_1 = \frac{B^2 - \left(\frac{\varphi_p \lambda}{4\pi}\right)^2}{2B\sin(\theta - \alpha) - \frac{\varphi_p \lambda}{2\pi}} \quad (4.19)$$

Accordingly,

$$h = H - R_1\cos\theta = H - \frac{B^2 - \left(\frac{\varphi_p \lambda}{4\pi}\right)^2}{2B\sin(\theta - \alpha) - \frac{\varphi_p \lambda}{2\pi}}\cos\theta \quad (4.20)$$

If no ground deformation has occurred between the acquisitions of the SLC image pair, the elevations of the points on the ground represent the topography information. A DEM of this area can be generated based on the topography of the imaged area.

4.5 Ground Deformation Monitoring by D-InSAR

InSAR, as a topography measurement technique, is highly sensitive to ground deformation. As a result, D-InSAR performs particularly well in ground deformation monitoring by removing topography information from the interferogram. As reviewed in Chapter 2, D-InSAR can be categorised into two-pass D-InSAR, three-pass D-InSAR and four-pass D-InSAR based on the number of SLC images used in differential interferometry (Lubis, et al., 2011).

4.5.1 Principle

For this research, two-pass D-InSAR was adopted to monitor ground deformation. Two sets of SLC images, captured before and after ground deformation respectively by the same radar antenna, are used to generate one interferogram which contains the topography and ground deformation information. Orbit parameters of the radar and external DEM created by Shuttle Radar Topography Mission (SRTM) are used to simulate an interferogram which is presented by a magnitude image of the area. The magnitude image only contains topography information. Accordingly, topography

information can be removed by undertaking differential interferometry, and the ground deformation results can be extracted from the differential interferogram.

4.5.2 Conditions for a Robust Result

In order to obtain a robust result of ground deformation using D-InSAR, the SLC image pair should meet the following criteria.

(1) SLC image with amplitude and phase information

The two interferograms to be used in the differential interferometry are generated from a SLC image pair. Each pixel of the SLC images must be represented by a complex number with the amplitude and phase information of the radar echo backscattered from scatterer in this pixel (see equation 4.4).

(2) Small baseline

In order to avoid spatial decorrelation, the baseline between the two acquisitions of the image pair should be no longer than the critical baseline. For instance, a perpendicular baseline of less than 800 m was defined for the selection of the interferometric pairs in the time series analysis of Mexico City's subsidence using InSAR (Yan, et al., 2012). For the subsidence monitoring in Murcia in Spain, 800 m was also chosen as the critical perpendicular baseline for the selection of the interferometric pair (Herrera, et al., 2009).

(3) Interferograms with good coherence

Amplitude and phase of the radar echo represent the strength of the radar echo and the argument of the complex number respectively (Samiei-Esfahany, 2008). If the amplitude and phase of radar echoes from the corresponding pixels of the SLC image pair are similar, the interferogram generated from this image pair has a good coherence.

Interferograms with good coherence are essential for the acquisition of a robust ground deformation result. Coherence of the interferograms is normally in the range of 0 to 1, where coherence of 0 indicates complete decorrelation of the D-InSAR result and coherence of 1 represents a very robust result. In the PS-InSAR data processing tool StaMPS, a coherence threshold of 0.3 is applied to define a pixel in

the interferogram with good coherence (Hooper , et al., 2013). Figure 4.7 shows the coherent phase image and incoherent phase image of the mountain area (European Space Agence, 2015).

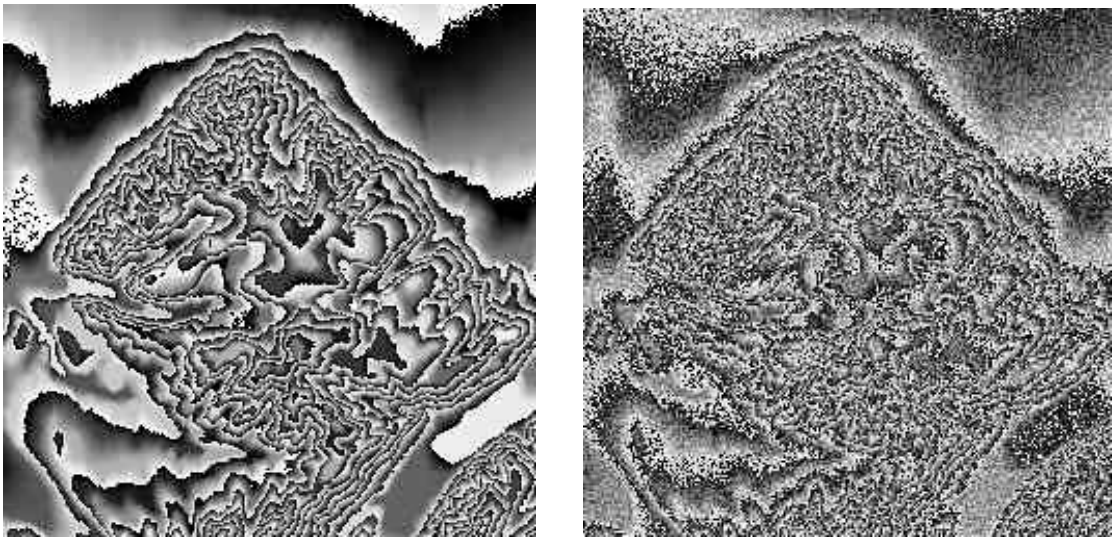

Figure 4.7: Coherent phase image of the mountain (left) and incoherent phase image of the mountain (right)

4.5.3 Procedure for Ground Deformation Monitoring

As stated, ground deformation results can be extracted by D-InSAR based on a pair of SLC images and external DEM. Figure 4.8 represents the procedure for applying two-pass D-InSAR in ground deformation monitoring.

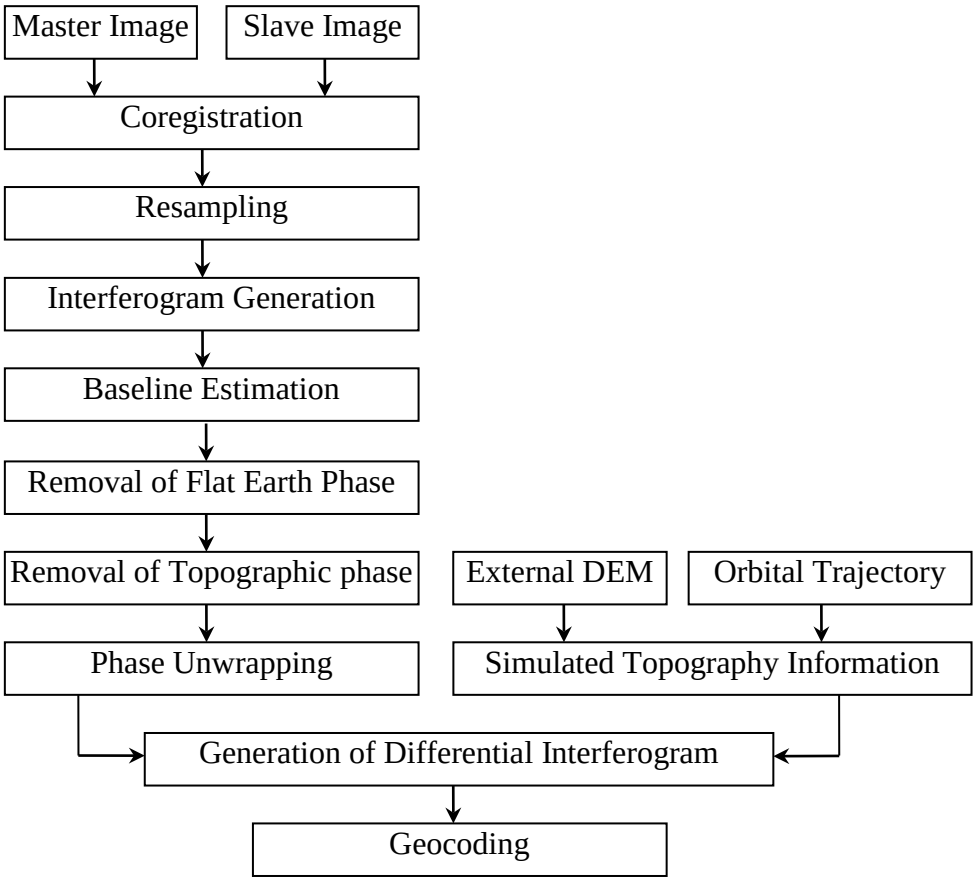

Figure 4.8: Ground deformation monitoring by two-pass D-InSAR

The steps of the procedure can be summarised as follows.

- Read SLC images

A pair of SLC images, captured before and after ground deformation by synthetic aperture radar, is selected. One SLC image is considered as the master image while the other image is the slave image. Due to random amplitude and phase information in the radar echoes from the individual scatterer, speckle noise appears in the SLC image (Moreira, 1991).

A multi-looking approach is applied to reduce the speckle noise by partitioning the beam of the synthetic aperture radar in the azimuth direction and generating more individual SAR images (Moreira, 1991). The SAR images are processed individually and composed pixel by pixel to generate a final multi-looking image. By the

application of multi-looking, the Signal to Noise Ratio (SNR) of the radar image is improved by reducing the azimuth resolution of the image.

- Coregistration and resampling

Coregistration to match the image pair, which involves coarse coregistration and fine coregistration, is applied to ensure the scatterer on the ground contributes to the corresponding pixels in master and slave images.

Coarse coregistration, a pair of SLC images is matched with an accuracy of one or two pixels. In the first step, tie points, which are features on the ground and corresponding pixels in the image pair, are selected. Theoretically, the more tie points are selected the more reliable is the result. However, a large number of tie points increases the calculation of the data processing.

After selecting tie points within the imaged area, the corresponding pixels in the image pair are matched by the cross-correlation method which is the most widely used approach for coarse coregistration (Franceschetti & Lanari, 1999) (Li & Bethel, 2008). A window which represents a part of the master image is selected. Pixels in the master image within this window are matched with the windows of the same size on the slave image. The window on the slave image, which has the highest cross-correlation coefficient, is selected as the matching window. Accordingly, azimuth and ground range offsets of the corresponding pixels are obtained. After matching all the pixels within the windows, average azimuth and range offsets of the pixels can be calculated. Based on the calculation result, the slave image can be shifted to match the position of the master image (Li & Bethel, 2008).

Coarse azimuth and range offset values for the corresponding pixels are essential for fine coregistration of the image pair. The acceptable accuracy for fine coregistration is 1 out of 10 pixels (Hanssen & Bamler, 1999). It has been demonstrated that there are certain rules to estimate the coordinate offsets of the corresponding pixels. Generally, the coordinate offsets can be fitted by higher order polynomials (Li & Bethel, 2008). On the master and slave images, a large number of corresponding pixel pairs are selected. Based on the azimuth and range coordinates of the pixels on the master image and the coarse coordinate offsets of the paired pixel on the slave image, a second order polynomial can be established for the estimation of a more precise

coordinate offset of the pixel pair. For instance, the precise coordinate offset can be fitted by a second order polynomial based on the least squares method. As a result, instead of the average azimuth and range offsets of the pixels in coarse coregistration, a coordinate transformation equation is generated for the fine coregistration of the SLC image pair (Li & Bethel, 2008).

By the application of the coordinate transformation equation, the slave image is resampled to the master image by transferring pixels from the grid of the slave image to the grid of master image (Slacikova & Potuckova, 2011).

- Interferogram generation

After coregistration and resampling, pixels in the slave image have the same coordinates as the corresponding pixels in the master image. Because each pixel is recorded as a complex number, an interferogram can be generated by multiplying the complex number of pixels in the master image and the conjugate complex number of the corresponding pixels in the slave image.

- Baseline estimation

In order to remove the flat earth phase and the topography phase from the interferometric phase and obtain the real ground deformation results, a baseline estimation is a critical step. This estimates the distance between the two radars for the acquisitions of the SLC image pair. The baseline can be estimated by an analysis of the orbit file if a precise orbit file is available.

- Addressing the flat earth effect

Due to the curvature of the Earth, points on the ground with the same elevation would have a phase difference for the two radar antennas. The phase difference results in the additional flat earth phase component to the phase of the interferogram. As shown in Figure 4.9, in repeat-pass D-InSAR, S_1 and S_2 are two radar antennas which transmit radar pulses to the scatterers on the ground and receive radar echoes. P and P’ are two scatterers with the same elevation on the ellipsoid surface of the Earth.

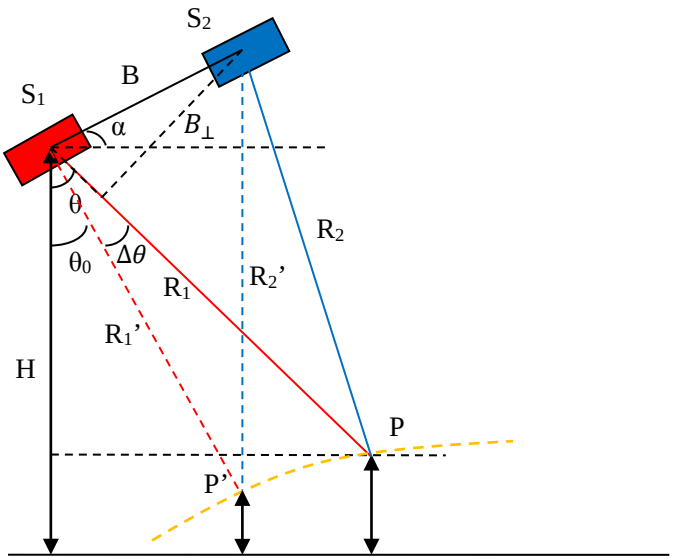

Figure 4.9: Geometry of flat earth effect

The phase of the radar pulses S_1P and S_2P is represented below.

$$\varphi_{s_1p} = \frac{4\pi}{\lambda} R_1 \tag{4.21}$$

$$\varphi_{s_2p} = \frac{4\pi}{\lambda} R_2 = \frac{4\pi}{\lambda} (R_1 + \Delta R) \tag{4.22}$$

Where,

φ_{p1}, φ_{p2}: phase of radar pulse S_1P and S_2P;

R_1, R_2: propagation distance from S_1, S_2 to P;

ΔR: difference between propagation distances R_1, R_2.

$$\Delta\varphi_p = \varphi_{s_2p} - \varphi_{s_1p} = \frac{4\pi}{\lambda} \Delta R \tag{4.23}$$

Where,

$\Delta\varphi_p$: phase difference between φ_{p1} and φ_{p2}.

According to cosine theorem,

$$\begin{aligned} {R_2}^2 &= {R_1}^2 + \Delta R^2 + 2R_1 \Delta R \\ &= {R_1}^2 + B^2 - 2R_1 B \cos\left(\frac{\pi}{2} - \theta + \alpha\right) \\ &= {R_1}^2 + B^2 - 2R_1 B \sin(\theta - \alpha) \end{aligned} \tag{4.24}$$

Where,

B: baseline between S_1 and S_2.

For spaceborne radar,

$$\Delta R < B \ll R_1 \tag{4.25}$$

Therefore, ΔR^2 can be ignored.

$$2R_1\Delta R = B^2 - 2R_1 B\sin(\theta - \alpha) \tag{4.26}$$

$$\Delta R = \frac{B^2}{2R_1} - B\sin(\theta - \alpha) \approx -B\sin(\theta - \alpha) \tag{4.27}$$

Thus,

$$\Delta\varphi_p = \frac{4\pi}{\lambda}\Delta R = -\frac{4\pi}{\lambda}B\sin(\theta - \alpha) \tag{4.28}$$

Similarly,

$$\Delta\varphi_{p'} = -\frac{4\pi}{\lambda}B\sin(\theta_0 - \alpha) \tag{4.29}$$

Where,

$\Delta\varphi_{p'}$: phase difference between radar pulses S_1P' and S_2P'.

Accordingly, the flat earth phase $\Delta\varphi_{flat}$ can be calculated.

$$\begin{aligned}\Delta\varphi_{flat} &= \Delta\varphi_p - \Delta\varphi_{p'} \\ &= \left[-\frac{4\pi}{\lambda}B\sin(\theta - \alpha)\right] - \left[-\frac{4\pi}{\lambda}B\sin(\theta_0 - \alpha)\right] \\ &= -\frac{4\pi}{\lambda}B[\sin(\theta_0 + \Delta\theta - \alpha) - \sin(\theta_0 - \alpha)] \\ &= -\frac{4\pi}{\lambda}B[\sin(\theta_0 - \alpha)\cos\Delta\theta + \cos(\theta_0 - \alpha)\sin\Delta\theta - \sin(\theta_0 - \alpha)]\end{aligned} \tag{4.30}$$

In a spaceborn radar system, $\Delta\theta \rightarrow 0$.

$$\sin\Delta\theta \approx \tan\Delta\theta \approx \Delta\theta \tag{4.31}$$

$$\cos\Delta\theta \approx 1 \tag{4.32}$$

Therefore,

$$\Delta\varphi_{flat} == -\frac{4\pi}{\lambda}B\cos(\theta_0 - \alpha)\Delta\theta = -\frac{4\pi}{\lambda}B_\perp\Delta\theta \tag{4.33}$$

In order to obtain a good D-InSAR result, the interferometric phase component caused by the flat earth effect must be removed by means of the precise orbit data of the radar (Li, et al., 2004).

- Addressing the topography effect

After removing flat earth phase, the Earth's surface can be considered as a plain. However, a topographic phase component results from the undulating topography of the Earth and will also contribute to the phase of the interferogram.

As shown in Figure 4.10, in repeat-pass D-InSAR, S_1 and S_2 are the two radar antennas which transmit radar pulses to the scatterers on the ground and receive radar echoes. P and P' are two scatterers with the same terrain height and different elevations

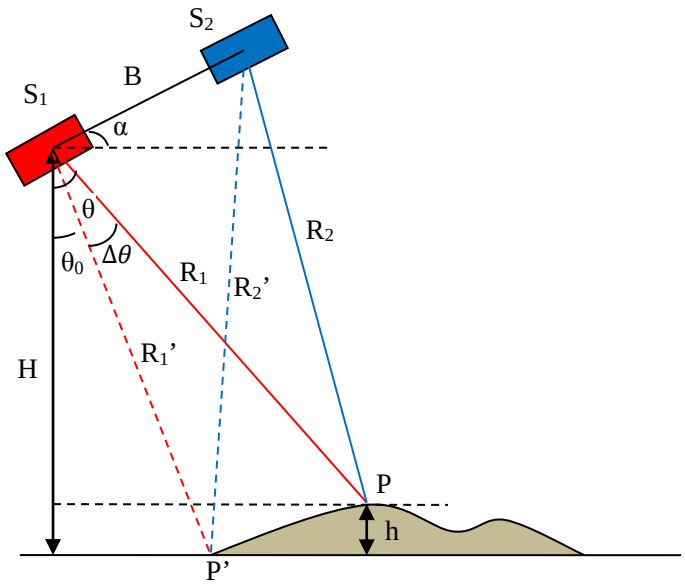

Figure 4.10: Geometry of the topography effect

The phases of radar pulse S_1P and S_2P are represented below.

$$\varphi_{s_1p} = \frac{4\pi}{\lambda} R_1 \tag{4.34}$$

$$\varphi_{s_2p} = \frac{4\pi}{\lambda} R_2 = \frac{4\pi}{\lambda} (R_1 + \Delta R) \tag{4.35}$$

$$\Delta\varphi_p = \varphi_{s_2p} - \varphi_{s_1p} = \frac{4\pi}{\lambda} \Delta R \tag{4.36}$$

Where,

φ_{p1}, φ_{p2}: phase of the radar pulse S_1P and S_2P;

$\Delta\varphi_p$: phase difference between φ_{p1} and φ_{p2}.

Similar to the calculation for the flat earth phase.

$$\Delta\varphi_p = \frac{4\pi}{\lambda} \Delta R = -\frac{4\pi}{\lambda} B \sin(\theta - \alpha) \tag{4.37}$$

$$\Delta\varphi_{p'} = -\frac{4\pi}{\lambda} B \sin(\theta_0 - \alpha) \quad (4.38)$$

Where,

$\Delta\varphi_{p'}$: phase difference between radar pulses S_1P' and S_2P';

B: Baseline between radar antennas S_1 and S_2.

Topographic phase $\Delta\varphi_{topo}$ can be calculated.

$$\Delta\varphi_{topo} = \Delta\varphi_p - \Delta\varphi_{p'} = -\frac{4\pi}{\lambda} B \cos(\theta_0 - \alpha)\Delta\theta \quad (4.39)$$

The topographic phase component can be removed by the external DEM or the DEM generated by InSAR (Tomás, et al., 2005).

- Phase unwrapping

On the interferogram, colour change of the interferometric fringe starts from the pixel where ground deformation is 0 to a pixel which has the same fringe colour as the starting pixel after completing a whole cycle. The phase difference between the two pixels is defined as 2π, which is a cycle of the interferometric fringe. Accordingly, after n completed colour cycles, the phase difference between the pixel with same colour as the starting pixel is 2π multiplied by n. Thus, the phase estimated on the interferogram is ambiguous. The multiples of 2π are called the phase integer cycle ambiguity. Therefore, the real phase of the pixel on the interferogram is calculated by the equation below.

$$\varphi_{real} = \varphi_{est} + 2\pi n \quad (4.40)$$

Where,

φ_{real}: real phase of the pixel;

φ_{est}: estimated phase of the pixel;

n: $n \in Z$, Z is a set of integers .

The interferometric phase of the interferogram starts to be wrapped modulo 2π. As a result, phase unwrapping should be applied to obtain the real phase of the interferogram by estimating the phase difference between neighbouring pixels on the interferogram (Klees & Massonnet, 1998).

- Simulated topography information

In order to remove the topographic phase and to obtain information of the real ground deformation, external DEM and precise orbital files are used to simulate a magnitude image of the DEM. The magnitude image with amplitude and phase information of the pixels contains only topography information. (Eineder & Adam, 2005).

- Generation of differential interferogram

By applying differential interferometry to the inteferogram generated from the SLC image pair and the simulated magnitude image of the DEM, the topographic phase is removed and a differential interferogram is generated.

- Geocoding

Geocoding aims to convert the unwrapped phase of the pixels in the differential interferogram from a radar coordinate system (range and azimuth) into a terrain map with the height information in the earth coordinate system (Schwabisch, 1998).

4.6 Ground Deformation Monitoring by PS-InSAR

Due to the limitations of the D-InSAR technique, such as temporal decorrelation caused by long time intervals between the image pair acquisition and spatial decorrelation caused by the long baseline between two radars, the reliability of the D-InSAR result is reduced. These limitations are addressed by means of Pesistent Scatterer InSAR (PS-InSAR), whereby more reliable ground deformation results can be obtained.

4.6.1 Selection of Master Image

In PS-InSAR, SAR images of the area to be observed are captured at different times by the radar and used to form image pairs for the generation of the time series interferograms. One master image is selected among all the SAR images based on the minimization of the temporal baseline, spatial baseline and mean Doppler centroid frequency difference (Hooper, et al., 2004); the rest of the images are defined as the slave images.

4.6.2 Interferogram Generation

Once the master image has been selected, interferometric pairs which consist of a master image and a slave image can be generated. For instance, N+1 SAR images are able to form N interferometric pairs and generate N interferograms.

The slave image of each interferometric pair is coregistered and resampled with the master image by transferring pixels from the grid of the slave image to the grid of the master image (Slacikova & Potuckova, 2011). Then, N time series interferograms are generated. After removing the flat earth phase from the interferograms, external DEM is applied to remove the topography information from the interferograms by carrying out differential interferometry, and a stack of time series differential interferograms is generated.

4.6.3 Phase Noise Estimation

The stack of differential inteferograms contains phase information of each pixel in the interferograms. After the flat earth removal and topography removal in D-InSAR, not only ground deformation but also phase noises, such atmospheric delay, orbit error, DEM error and other noise, contribute to the residual phase of each pixel in the interferogram.

$$\varphi_{x,i} = \varphi_{def,x,i} + \varphi_{atm,x,i} + \varphi_{orb,x,i} + \varphi_{dem,x,i} + \varphi_{n,x,i} \tag{4.41}$$

Where,

$\varphi_{x,i}$: phase of the pixel x in the i^{th} interferogram;

$\varphi_{def,x,i}$: ground deformation phase;

$\varphi_{atm,x,i}$: atmospheric delay phase;

$\varphi_{orb,x,i}$: orbit error phase;

$\varphi_{dem,x,i}$: residual topographic phase caused by DEM error;

$\varphi_{n,x,i}$: noise phase.

The residual phase noise of the pixel is defined as the original phase minus the average phase of the pixels within a circle with a specific radius (Hooper, et al., 2004) (Hooper , et al., 2013). Accordingly, the phase noise of the pixel x in the interferogram i is represented as below.

$$\Delta\varphi = \varphi_{x,i} - \overline{\varphi}_{x,i} \tag{4.42}$$
$$= (\varphi_{dem,x,i} - \overline{\varphi}_{dem,x,i} + \varphi_{n,x,i} - \overline{\varphi}_{n,x,i}) + (\varphi_{def,x,i} - \overline{\varphi}_{def,x,i}) + (\varphi_{atm,x,i} - \overline{\varphi}_{atm,x,i}) + (\varphi_{orb,x,i} - \overline{\varphi}_{orb,x,i})$$

Where,

$\Delta\varphi$: phase noise of the pixel x;

$\overline{\varphi}_{x,i}$: average phase of the pixels;

$\overline{\varphi}_{def,x,i}$: average ground deformation phase of the pixels;

$\overline{\varphi}_{atm,x,i}$: average atmospheric delay phase of the pixels;

$\overline{\varphi}_{orb,x,i}$: average orbit error phase of the pixels;

$\overline{\varphi}_{dem,x,i}$: average DEM error phase of the pixels;

$\overline{\varphi}_{noise,x,i}$: average noise phase of the pixels.

Within the selected circle, $\varphi_{def,x,i}$, $\varphi_{atm,x,i}$ and $\varphi_{orb,x,i}$ are assumed to be spatially correlated over a specific distance while $\varphi_{dem,x,i}$ and $\varphi_{n,x,i}$ are assumed to be spatially-uncorrelated (Hooper, et al., 2004). For spatially correlated items over a small distance, the phase change of the pixels is small and can be ignored. For spatially uncorrelated items, the average phase of the pixels within the selected circular area is estimated as zero. In addition, the noise phase results from variable scattering from the pixel, errors in coregistration and thermal noise, and it is small enough not to affect the phase stability of the pixel. As a result, the phase caused by DEM error $\varphi_{dem,x,i}$ is the only contributor to the phase noise of the pixel $\Delta\varphi$.

$$\Delta\varphi = \varphi_{x,i} - \overline{\varphi}_{x,i} \approx \varphi_{dem,x,i} \tag{4.43}$$

In addition, the DEM error phase is proportional to the perpendicular baseline.

$$\varphi_{dem,x,i} = B_{\perp x,i} K_{dem,x} \tag{4.44}$$

Where,

$B_{\perp x,i}$: perpendicular baseline of pixel x in the i^{th} interferogram;

$K_{dem,x,}$: proportionality constant for pixel x in the i^{th} interferogram.

Accordingly,

$$\varphi_{x,i} - \overline{\varphi}_{x,i} = B_{\perp x,i} K_{dem,x} \tag{4.45}$$

$\varphi_{x,i}$ and $\overline{\varphi}_{x,i}$can be obtained from the interferogram while $B_{\perp x,i}$ can be acquired from the precise knowledge of the radar orbit. Therefore, the proportionality constant for pixel x can be estimated based on the least squares method. As a result, the DEM error phase of pixel x in the i^{th} interferogram can be estimated sufficiently well by $B_{\perp x,i}$ and $K_{dem,x}$.

$$\widehat{\varphi}_{dem,x,i} = B_{\perp x,i} K_{dem,x} \tag{4.46}$$

Where,

$\widehat{\varphi}_{dem,x,i}$: estimated DEM error phase of pixel x of the i^{th} interferogram.

The phase stability of the pixel can be estimated by Υ which is a measure for the coherence of the pixel based on the estimated phase noise of the pixel.

$$\Upsilon_x = \frac{1}{N}\left|\sum_{i=1}^{N} \exp\left\{\sqrt{-1}\left(\varphi_{x,i} - \overline{\varphi}_{x,i} - \widehat{\varphi}_{dem,x,i}\right)\right\}\right| \tag{4.47}$$

Where,

Υ_x: coherence of the pixel x in the stack of the interferograms;

N: the number of interferograms.

4.6.4 Selection of the Persistent Scatterer

In order to eliminate phase noise and obtain a robust ground deformation result, only pixels with a dominating scatterer are selected as the persistent scatterer (PS) pixels. The selected PS pixels have good coherence even over a long time period.

The scattering signal of a pixel can be considered as a beam of signals from individual scatterers within this pixel. Random scatterers with variable amplitude and phase information within a pixel result in random phase distribution between $-\pi$ and π while a persistent scatterer is the main contributor to the amplitude and phase of the pixel. As a result, a PS pixel has stable phase and amplitude.

Figure 4.11 (Hooper, 2006) depicts the phase distribution of the corresponding pixel in 100 SAR images. Red arrows indicate the scattering signal of an individual scatterer within the pixel. Blue plots represent the simulated phase of the pixel in the 100 SAR images. The distribution of blue plots is random for the pixel without PS and is centralised in the PS pixel (Hooper, 2006). A PS pixel not only has stable

amplitude and phase information but also has a good coherence with the corresponding pixel on other SAR images.

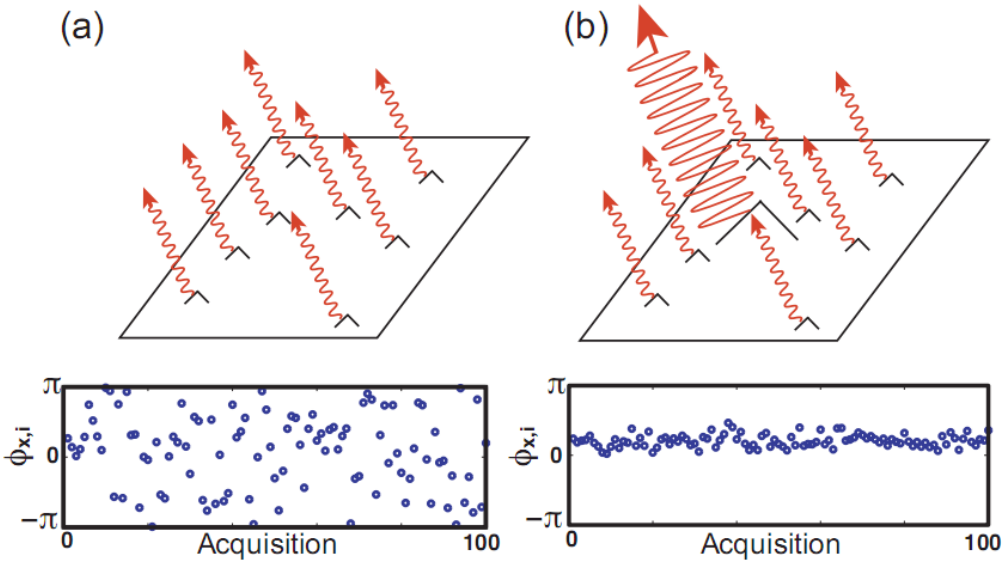

Figure 4.11: Simulated phase for a pixel without PS (a) and a pixel with PS (b)

An approach based on pixel amplitude stability is applied to select the PS from the stack of differential interferograms. An amplitude dispersion index threshold is defined for PS candidate (PSC) selection (Ferretti, et al., 2001).

$$D_A \equiv \frac{\sigma_A}{\mu_A} \tag{4.48}$$

Where,

D_A: amplitude dispersion index of the pixel;

σ_A : standard deviation of the pixel amplitude;

μ_A: mean of the pixel amplitude.

The scatterer within this pixel is selected as a PSC if D_A of this pixel is smaller than the amplitude dispersion index threshold. Accordingly, the larger the threshold value, the better the choice of the PSC. A threshold value of 0.4 was selected for measuring volcanic deformation by Hooper and his colleagues (Hooper, et al., 2004).

However, most of the PSC selected based on the amplitude dispersion index threshold are not PS. For scatterers with low SNR, the relationship between phase stability and amplitude dispersion will break down. As a result, PS selection based on amplitude

stability for an area with vegetation coverage does not work as well as when it is implemented for an urban area with many man-made structures, due the low SNR of the scatterers in an area of vegetation (Hooper, et al., 2004). A further PS selection will be applied on the selected PSC based on the phase stability of the pixel.

As described in the phase noise estimation step, the phase stability of the pixel can be estimated by Υ, a measure for the coherence of the pixel (see equation 4.47). The larger the coherence of the pixel, the more likely the scatterer within this pixel is the PS. A coherence threshold γ^{thresh} for the pixel is set for the selection of the PS. The coherence of a random phase pixel will not be high. Normally, if the coherence of a pixel is less than 0.3, the probability of the PS being present in this pixel is almost zero (Hooper, et al., 2004).

In addition, the signal contribution from neighbouring pixels may result in phase noise of the signal for the PSC. As a result, PSC with signal contributions from neighbouring pixels should be eliminated. The PSC will be dropped if the standard deviation of the phase noise for all its neighbouring pixels for the stack of differential interferograms is greater than 1 (Hooper , et al., 2013).

4.6.5 Dem Error Correction and Phase Unwrapping

As described in the phase noise estimation step, the DEM error phase of the pixel can be estimated from the perpendicular baseline and the proportionality constant for the pixel (see equation 4.46). Based on the estimated DEM error, the phase error caused by the DEM error can be corrected. In the equation below, $\varphi_{x,i}$ minus $\widehat{\varphi}_{dem,x,i}$ refers to the phase noise of the pixel after the DEM error correction.

$$\varphi_{x,i} - \widehat{\varphi}_{dem,x,i} = \varphi_{def,x,i} + \varphi_{atm,x,i} + \varphi_{orb,x,i} + (\varphi_{dem,x,i} - \widehat{\varphi}_{dem,x,i}) + \varphi_{n,x,i} \quad (4.49)$$

$$= \varphi_{def,x,i} + \varphi_{atm,x,i} + \varphi_{orb,x,i} + \varphi'_{dem,x,i} + \varphi_{n,x,i}$$

Where,

$\varphi_{x,i}$: phase of the pixel x in the i^{th} interferogram;

$\varphi_{def,x,i}$: ground deformation phase;

$\varphi_{atm,x,i}$: atmospheric delay phase;

$\varphi_{orb,x,i}$: orbit error phase;

$\varphi_{dem,x,i}$: residual topographic phase caused by DEM error;

$\varphi_{n,x,i}$: noise phase;

$\hat{\varphi}_{dem,x,i}$: estimated DEM error phase of pixel x;

$\varphi'_{dem,x,i}$: residual DEM error phase of pixel x.

The Estimated DEM error $\hat{\varphi}_{dem,x,i}$ is almost the same as $\varphi_{dem,x,i}$, therefore, the residual DEM error phase can be ignored.

After the DEM error correction stage, the ambiguous phase of each pixel is recovered by phase unwrapping. Goldstein filtering is adopted to filter the corrected phase of the pixel and to reduce its phase noise before phase unwrapping (Goldstein & Werner, 1998). Different from conventional InSAR, a time series analysis is carried out in PS-InSAR. Therefore, apart from the phase wrapped in the azimuth and range dimensions, time is the third dimension in phase unwrapping. Three dimensional (3D) phase unwrapping is simulated as two dimensional (2D) phase unwrapping by removing the phase difference of the pixel in the time dimension which refers to the phase difference caused by the time interval between the acquisitions of the master image and each slave image (Hooper & Zebker, 2007). As a result, the real phase of each pixel across the interferogram can be obtained by calculating the phase difference between the neighbouring pixels based on the statistical-cost, network-flow algorithm for phase unwrapping (SNAPHU) (Chen & Zebker, 2001) (Hooper , et al., 2013). This is a complicated method, which is integrated in the software StaMPS used for the PS-InSAR data processing and will not be discussed further.

4.6.6 Phase Filtering for Spatially Correlated Error

Even after phase unwrapping, it is still difficult to extract the ground deformation phase from the phase of the interferogram, due to the phase contribution of the four phase errors which are atmospheric phase, orbit phase, residual DEM error phase and noise phase. The spatially correlated items, such as atmospheric phase and orbit phase, are assumed to be temporally uncorrelated terms. High-pass filtering in time and low-pass filtering in space can be carried out to estimate the phase of the spatial correlated items (Hooper, et al., 2004).

Spatially correlated terms can be removed based on the estimation result. Only the ground deformation phase, residual DEM error phase and noise phase exist in the phase of the pixel. As both the residual DEM error phase and noise phase are small enough to be ignored, the ground deformation phase of the pixel can be obtained (Hooper, et al., 2004).

4.6.7 Extraction of Ground Subsidence

The phase caused by the ground deformation can be extracted from the phase of the pixel in the interferogram and the ground deformation result in the LOS direction can be obtained. In order to obtain the real ground deformation, the ground deformation value in the LOS direction is projected on the direction perpendicular to the ground.

4.7 Summary

This chapter introduced the methodologies used for subsidence monitoring, and their relevance for the railway. Section 4.2 described the concept of Real Aperture Radar (RAR) and its imaging principle. In order to improve the resolution of the radar image, an approach using Synthetic Aperture Radar (SAR) was introduced in Section 4.3. This is able to obtain a radar image with good resolution with a short radar antenna. Based on the principle of SAR, Section 4.4 presented a method for DEM generation by InSAR. Once ground deformation has occurred, a DEM generated by InSAR contains not only topography information but also ground deformation information. Section 4.5 introduced the principle and procedures of applying D-InSAR in ground deformation extraction. Moreover, the conditions required for a good D-InSAR result were illustrated. Following the introduction of D-InSAR, the principle of PS-InSAR was introduced in Section 4.6. PS-InSAR overcomes some of some the limitations of D-InSAR, such as temporal decorrelation and spatial decorrelation and is able to obtain a robust ground deformation result. Section 4.6 indicated the approaches for PS selection and the main procedures for ground deformation monitoring.

Chapter 5 Railway Subsidence Prediction with Time Series Prediction Models

5.1 Introduction

The aim of the overall study is to check the suitability of prediction models and their performance in subsidence forecasting. In order to select the most reliable model, all three types of models mentioned in Chapter 3 will be applied and the performance of these models will then be compared.

This section firstly introduces a method based on the auto-regressive and moving average (ARMA). The ARMA model is based on traditional statistical theories and it is suitable for time series with a large data volume and clear developing trend. Specifically, the auto-regressive integrated moving average (ARIMA) model, which is a generalised version of ARMA based on the Box-Jenkins approach, is introduced. Then the detailed procedure of the Box-Jenkins approach is described, ranging from data transformation to model validation. Compared to the fully standardised processes of the approach using the ARIMA model, the methodology when using an artificial neural network (ANN) model may vary, depending on the type of ANN chosen for the research. The ANN model was inspired by artificial intelligence and it works well when the system has fewer observations than traditional statistical model with an un-linear trend. A multi-layer neural network equipped with the learning algorithm of gradient descent backpropagation, is selected in this study since it is applied widely. This chapter will illustrate the rationale of constructing input, hidden and output layers, the critical functions to produce the output of the neural network as well as the detailed working processes of the gradient descent backpropagation algorithm. At the end, the main steps of grey modeling are described, which include grey sequence generating, A grey modeling and grey forecasting. Grey model is able to analyse the system with limited observations, partly unknown parameters and inter-relationships.

5.2 Railway Subsidence Prediction Models

5.2.1 ARIMA (p,d,q) Model

The Box-Jenkins methodology is the most popular approach to developing an ARIMA model. In general, there are 5 major steps to establish an ARIMA model: transforming raw data, determining the order of differencing, and the auto-regressive and moving average, estimating the parameters for the model, testing the suitability and accuracy of the model and using the model for forecasting.

(1) Data transformation

As an ARIMA model is only applicable for a stationary data series all the trend and seasonality features must be removed from the raw data, if they exist. In order to detrend the raw data, the trend parameter can be divided by fitting the raw data with a linear trend line which is then subtracted from the raw data. Sometimes, the raw time series data can show a pattern of non-linear trend. In this situation, the data must be transformed first in order to convert the non-linear trend to a linear trend. The most frequently adopted algorithm is a logarithm which can transform compounding growth into a linear growth and which can also convert the multiplicative relationship into an additive relationship. Seasonality can be removed by incorporating seasonal adjustments which can be either additive or multiplicative, as mentioned earlier.

(2) Determining the order of the model

The first step in establishing an ARIMA model is to decide the order of differencing, which can further remove any non-stationary pattern from the data. An Auto Correlation Function (ACF) is usually used to determine the order of differencing. It is the correlation between different periods of the time series data, where the time difference is referred to as the 'lag'.

The Auto correlation function (ACF) at lag t is:

$$\rho_s(t) = \mathrm{Corr}(S_{T+t}, S_T) \equiv \frac{\gamma_s(t)}{\gamma_s(0)} \tag{5.1}$$

Where,

$\rho_s(t)$: correlation at lag t (correlation between S_T and S_{T+t});

S_T, S_{T+t}: actual data at the periods T and T+t;

$\gamma_s(0)$: variance of the time series data.

The Auto covariance function (ACVF) at lag t is:

$$\gamma_s(t) = \mathrm{Cov}(S_{T+t}, S_T) \tag{5.2}$$

Where,

$\gamma_s(t)$: covariance at lag t (covariance between S_T and S_{T+t}).

The determining rules can be summarised as follows (Duke University, n.d.):

- If the time series data shows continuously significant positive autocorrelation, further differencing is required (Figure 5.1);
- If the time series shows significant negative autocorrelation, particularly at lag 1, the order of differencing should be decreased (Figure 5.2).

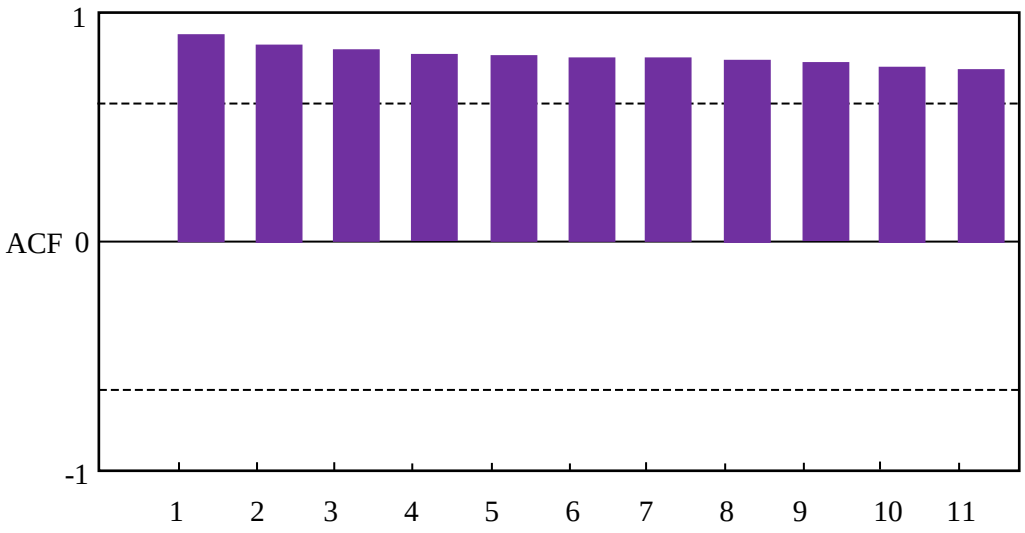

Figure 5.1: Significant positive autocorrelation (no cut off)

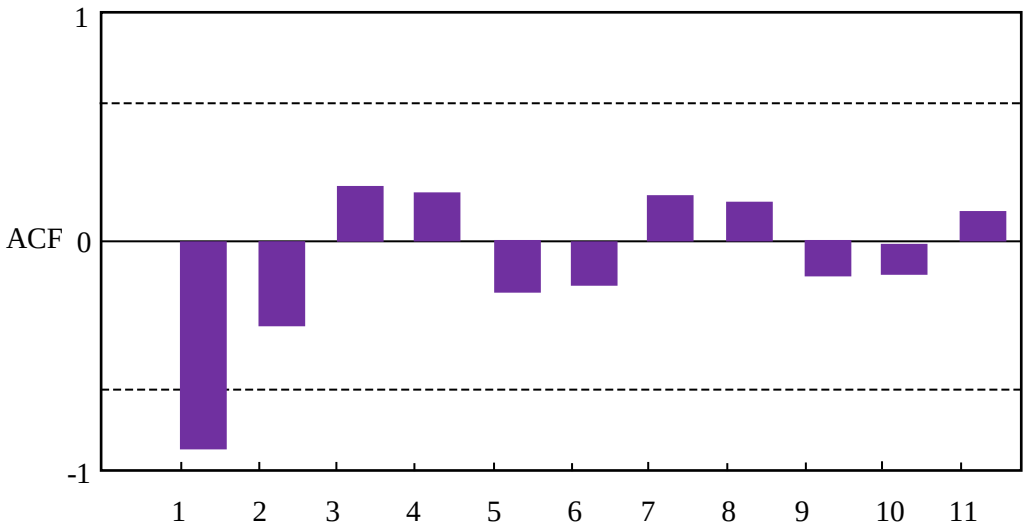

Figure 5.2: Significant negative autocorrelation

After obtaining a stationary time series through trend and seasonal adjustments as well as differencing, the next step is to decide the order of the AR and the order of the MA. According to the Box-Jenkins approach, the auto correlation function (ACF) and partial auto correlation function (PACF) can be used to find the value of p and q (Box & Jenkins, 1976).

Slightly different from ACF, PACF is a type of conditional ACF which is the autocorrelation between S_T and S_{T+t} after removing their dependence on S_{T+1} through to S_{T+t-1}.

$$\mathrm{PACF(t)} = \mathrm{Corr}(S_{T+t} - L_t(S_{T+t}), S_T - L_t(S_T)) \tag{5.3}$$

Where,

S_T, S_{T+t}: actual data at the periods T and T+t;

$L_t(S_{T+t})$: projection of S_{T+t} based on n S_{T+1} , S_{T+2} … S_{T+t-1}

$L_t(S_T)$: projection of S_T based on n S_{T+1} , S_{T+2} … S_{T+t-1}

The first step is to have plots of ACF and PACF for the time series with lags. Then the pattern of the plots can be used to determine a suitable type of ARIMA models for the time series (Duke University, n.d.).

- If the ACF plots do not cut off, but the PACF plots cut off after lag p, then the ARIMA (p,d,0) should be adopted (Figure 5.3);

- If the ACF plots cut off after lag q, but the PACF plots do not cut off, then the ARIMA (0,d,q) are preferred (Figure 5.4);
- If neither of the ACF and PACF plots cut off, then the ARIMA (p,d,q) model should be chosen.

In the third scenario listed above, it is usually quite difficult to guess the p and q. One of the best approaches is to apply a trial and error approach, where the engineer guesses the values of p and q first and then adjusts the values until there is no significant auto correlation of the residuals.

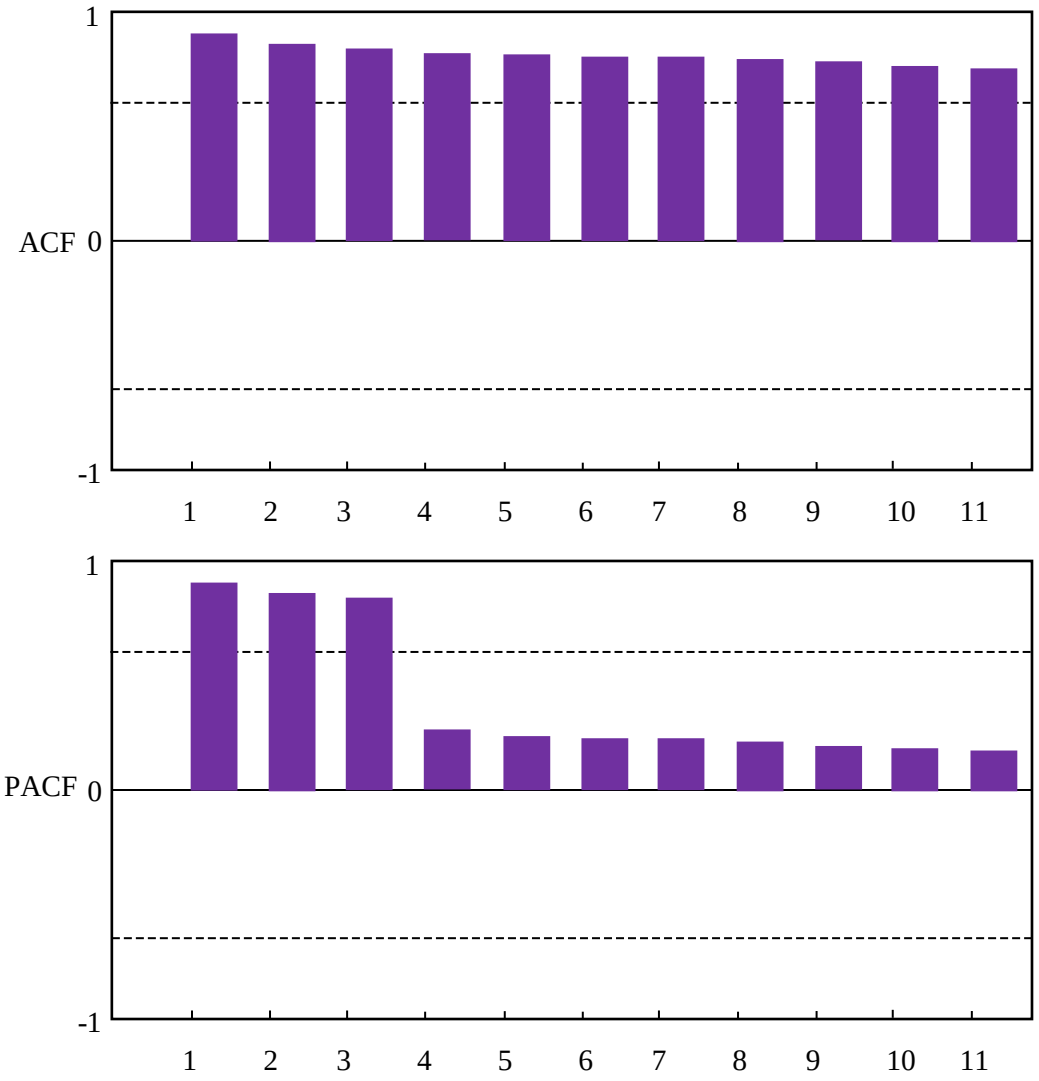

Figure 5.3: ACF plots do not cut off (upper); PACF plots cut off at p=4 (lower)

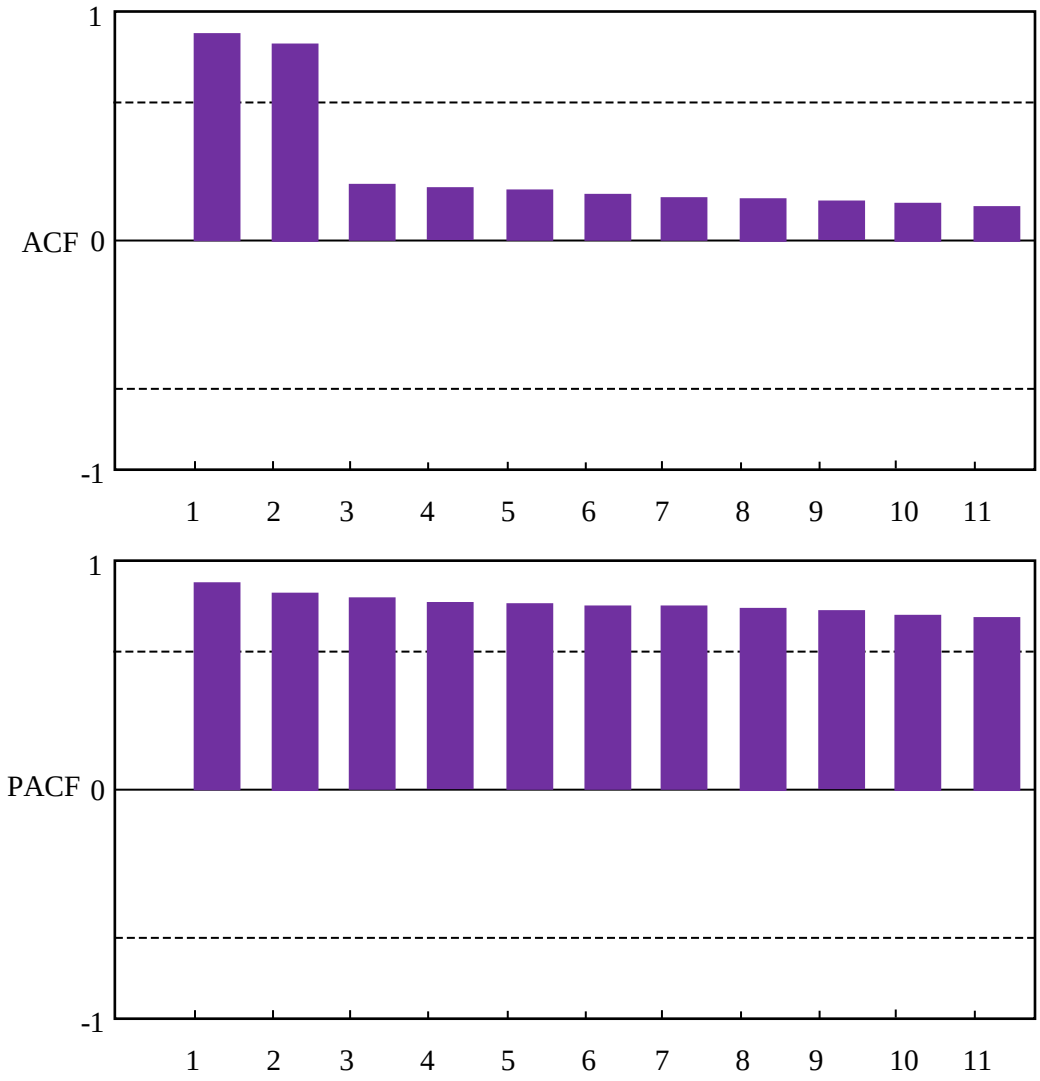

Figure 5.4: ACF plots cut off at q=3 (upper); PACF plots do not cut off (lower)

(3) Estimating the parameters of the model

After determining the orders for the ARIMA model, the final stage of constructing the model is to estimate the parameters of the AR terms and the MA terms. Depending on the values of p and q, there are different methods for the estimation.

- If there are only AR terms in the ARIMA model, meaning q is equal to 0, the ARIMA model is a pure linear regression model. In this case, the standard least squares method can be used to fit the parameters.

- For an ARIMA model with both AR and MA terms, the least squares estimation is not applicable, as the MA terms bring in a non-linear relationship. Instead, the maximum likelihood estimation approach should be chosen, which can solve the parameters (Box & Jenkins, 1976).

(4) Testing the ARIMA model and forecasting the future

Once the ARIMA model has been established, the residuals between the actual historical time series data and the data estimated by the model should be checked. If the distribution of the residuals is random and stationary, the proposed model is appropriate. Otherwise, the model needs to be adjusted (Makridakis & Hibon, 1997).

5.2.2 Artificial Neural Network Model

To develop a basic ANN model, there are three main steps:

(1) Choose the input and output data

As a typical ANN model comprises of one input layer, one output layer and certain hidden layers, the first step is to determine the structures of the input and output layers, i.e., the number of neurons placed thereon.

The number of nodes on the input layer usually depends on the number of factors which will be considered in the analysis and that will contribute to the final output. Sometimes, the input data contains not only quantifiable elements but also some qualitative factors. In this situation, category values can be used for the qualitative data. For instance, qualitative descriptions low, median and high can be presented as quantitative expression 0.1, 0.5 and 0.9 respectively. In order to avoid over-fitting weights of neurons in the learning process of an ANN, some researchers suggested normalising the original input data into data with the same range (Haykin, 1994).

The output layer usually contains only 1 neuron which produces the required outcome. In this thesis, the purpose is to predict subgrade subsidence. Therefore, the output can be either the forecasted subsidence or the subsidence changes in the future.

(2) Data learning process

As mentioned earlier, there are several popular approaches for the ANN to learn the historical data and to adjust neuron weights automatically. For the present study, the

gradient descent backpropagation algorithm is chosen to determine these weights. Back propagation means that an error signal will be generated first at the output layer and it will then be propagated back to the prior layers, which enables the ANN to learn from the error and activate automatic adjustments.

The main procedure starts with assigning random weights to all the input and hidden neurons, which produces an initial output. Then the initial output is compared with the expected output. If the error between the initial output and the expected output is significant, the ANN will then adjust the weights of each input and the hidden neurons. This iteration will continue until the error is minimum. The definition and threshold for the minimum error may vary in practice. In the 'nnet' package from R, it looks to minimise least squares and the threshold is set to $1.0 * e^{-4}$.

The outputs of the ANN depend on the inputs and the activation function, which produce values passed to the output function. The activation function can be illustrated as follows:

$$A_k = \sum_{i=0}^{n} x_i w_{ki} \tag{5.4}$$

Where,

A_k: activation function of the neuron k;

n: the number of the inputs for the neuron k;

x_i: the i^{th} input for the neuron k;

w_{ki}: weight of the i^{th} input for the neuron k.

Usually x_0 is assumed to be 1 and the activation function is thus changed to the following equation:

$$A_k = \sum_{i=1}^{n} x_i w_{ki} + b_k \tag{5.5}$$

Where,

b_k: $x_0 w_{k0}$, and this is known as the bias term.

Therefore, the actual inputs for neuron k are $x_1, x_2, \ldots, x_n$. The reason to have a bias term is that it can bring more flexibility into the learning process of the ANN and achieve the required output, which otherwise cannot be obtained without a bias term. As the bias term is actually equal to w_{k0}, it can be learned exactly like the other weights.

The output function can be the same as the activation function. However, the most widely used output function is a sigmoid function:

$$O_k = \frac{1}{1+e^{A_k}} \tag{5.6}$$

Where,

O_k: output from the neuron k.

Then the prediction errors are calculated as:

$$E_k = (O_k - T_k)^2 \tag{5.7}$$

Where,

E_k: error of the output from the neuron k;

T_k: expected output from the neuron k.

The error is the square of the difference between the output and the expected output as it will always be positive and represents the degree of discrepancy.

The total prediction error is:

$$E = \sum_{k=1}^{n}(O_k - T_k)^2 \tag{5.8}$$

The ANN adjusts the weights of the input and hidden neurons in order to decrease the total prediction error. The adjustments will be based on the dependency of the total error on each weight, which is given as a gradient as follows:

$$\Delta w_{ki} = -\eta \frac{\partial E}{\partial w_{ki}} \tag{5.9}$$

Where,

Δw_{ki}: the adjustment on w_{ki};

η: known as the learning rate which determines the size of each adjustment.

To obtain the derivative of E in respect to w_{ki}, partial derivatives can be used.

$$\frac{\partial E}{\partial w_{ki}} = \frac{\partial E}{\partial O_k} * \frac{\partial O_k}{\partial w_{ki}} \tag{5.10}$$

Where:

$$\frac{\partial E}{\partial O_k} = 2(O_k - T_k) \tag{5.11}$$

$$\frac{\partial O_k}{\partial w_{ki}} = \frac{\partial O_k}{\partial A_k} * \frac{\partial A_k}{\partial w_{ki}} = O_k(1 - O_k)x_i \tag{5.12}$$

Therefore,

$$\frac{\partial E}{\partial w_{ki}} = 2(O_k - T_k)O_k(1 - O_k)x_i \quad (5.13)$$

$$\Delta w_{ki} = -\eta * 2(O_k - T_k)O_k(1 - O_k)x_i \quad (5.14)$$

Similarly, if there are multiple layers in the ANN (see Figure 5.5), x_i will be generated from the previous layer and the same process can be applied to obtain the changes in the weights for the input for the previous layer:

$$\Delta w_{ij} = -\eta \frac{\partial E}{\partial w_{ij}} = -\eta \frac{\partial E}{\partial x_i} * \frac{\partial x_i}{\partial w_{ij}} \quad (5.15)$$

Where,

Δw_{ij}: the adjustment on w_{ij};

w_{ij}: weight of the input for neuron i on the previous layer, which produces x_i for the next layer.

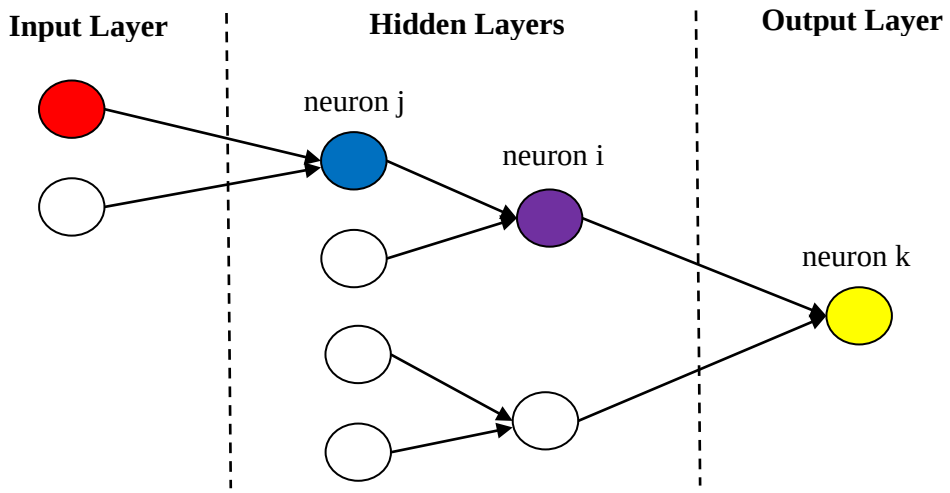

Figure 5.5: ANN model with multilayers

Then the adjustment of the weights (Δw_{ij}) can be obtained as follows:

$$\frac{\partial E}{\partial x_i} = 2(O_k - T_k)O_k(1 - O_k)w_{ki} \quad (5.16)$$

$$\frac{\partial x_i}{\partial w_{ij}} = x_i(1 - x_i)u_j \quad (5.17)$$

Where,

u_j: the j^{th} input for the neuron i.

Sometimes, a momentum term will also be introduced in the calculation of the weight adjustments in order to avoid the weight adjustment being terminated at a local minimum of the prediction error. The adjustment with a momentum term is in the form of:

$$\Delta w_{ki}(t) = -\eta \frac{\partial E}{\partial w_{ki}} + m \Delta w_{ki}(t-1) \tag{5.18}$$

Where,

m: the momentum term that has a value between 0 and 1.

The equation means that the adjustment of the weight also considers the impact of the adjustment made in the previous iteration. The momentum term represents the degree of this impact, which has been demonstrated to be effective in avoiding the local minimum and find the global minimum of the prediction error. If the value of m is set to too high, then the risk of skipping the global minima will be increased. On contrary, if m is too small, it might not be large enough to avoid local minima. Usually it will be set to a relatively small value at first and adjusted later depending on the change of prediction errors.

Based on the algorithm illustrated above, all the weights of the neurons can be decided when the prediction error reaches its minimum level.

(3) Model testing

As there are no established criteria to determine the optimal structure of the ANN model, the performance of the ANN model can vary even with the same back propagation algorithm. In order to obtain a reliable ANN model, the last step is to check and compare the accuracy and reliability of models with various structures, including different numbers of hidden layers, numbers of nodes on each hidden layer and numbers of data points in the training set (Suwansawat & Einstein, 2006).

The most common measure to assess the performance of an ANN model is the root mean square error (RMSE), which can be calculated as follows:

$$RMSE = \sqrt{\frac{\sum_{k=1}^{n}(O_k - T_k)^2}{n}} \tag{5.19}$$

Where,

O_k: the output from neuron k;

T_k: the actual observation for neuron k;

n: the number of output neurons.

Usually, an ANN model with more layers and more nodes on the hidden layers will have a smaller RMSE with the training set. However, this will also increase the risk of over-fitting, in other words, the performance of the model will drastically drop when being used in actual forecasting. Hence, the optimal model should have relatively small RMSE for both the training set and the validation set in order to avoid over-fitting.

5.2.3 Grey Model

As there is only one variable in the time series prediction for this study, which is the observation of the subsidence at various time points, a GM (1, 1) model will be suitable for the prediction. Generally, grey theory-based modelling and forecasting can be divided into 3 steps:

(1) Grey sequence generation

The raw data from a grey system does not usually have clean patterns in a time series data set, leading to the difficulty of extracting governing laws from the data. The grey system theory attempts to transform the raw data into a more regular series whose pattern can be captured through grey analysis. This process is known as grey sequence generating (Deng, 1989), which is achieved though Accumulated Generating Operation (AGO).

Assuming that we have a series of settlement observations as:

$$x^{(0)} = \left(x^{(0)}(1),\ x^{(0)}(2),\ x^{(0)}(3), \dots, x^{(0)}(n)\right),\ n \geq 4, \tag{5.20}$$

Where,

$x^{(0)}(n)$: the original time series data at time n.

The AGO will then generate the new grey data as follows:

$$x^{(1)}(k) = \sum_{i=1}^{k} x^{(0)}(i) \tag{5.21}$$

This means that $x^{(1)}(k)$, as the k^{th} data point in the grey sequence, is the sum of all original data before the k^{th} position. Clearly, the AGO establishes a relationship between the new grey data through cumulative summation. The new grey time series data obtained are as follows:

$$x^{(1)} = \left(x^{(1)}(1),\ x^{(1)}(2),\ x^{(1)}(3), \dots, x^{(1)}(n)\right),\ n \geq 4 \tag{5.22}$$

Where,

$x^{(1)}(n)$: the grey time series data at time n.

(2) Grey modelling

After generating the grey sequence, a first order differential equation of a grey GM (1, 1) model can be built (Deng, 1989).

$$\frac{dx^{(1)}(t)}{dt} + ax^{(1)}(t) = b \tag{5.23}$$

Where,

a: the developing coefficient;

b: the grey input.

The equation then can be transformed through the following steps:

$$dx^{(1)}(t) + ax^{(1)}(t)dt = bdt \tag{5.24}$$

$$\int_k^{k+1} dx^{(1)}(t) + a\int_k^{k+1} x^{(1)}(t)dt = b\int_k^{k+1} dt \tag{5.25}$$

Where,

$$\int_k^{k+1} dx^{(1)}(t) = x^{(1)}(k+1) - x^{(1)}(k) = x^{(0)}(k+1) \tag{5.26}$$

$$a\int_k^{k+1} x^{(1)}(t)dt = a(x^{(1)}(k+1) + x^{(1)}(k))/2 \tag{5.27}$$

Letting $z^{(1)}(k+1) = (x^{(1)}(k+1) + x^{(1)}(k))/2$, also known as the mean of the neighbouring data , then

$$a\int_k^{k+1} x^{(1)}(t)dt = az^{(1)}(k+1) \tag{5.28}$$

$$b\int_k^{k+1} dt = b \tag{5.29}$$

Therefore, the final grey model can be defined as (Deng, 1989):

$$x^{(0)}(k+1) + az^{(1)}(k+1) = b \tag{5.30}$$

Based on the least squares method, the value of a and b can be obtained as follows:

$$[a, b]^T = (B^T B)^{-1} B^T Y \tag{5.31}$$

Where,

$$B = \begin{bmatrix} -z^{(1)}(2) & 1 \\ \cdots & \cdots \\ -z^{(1)}(n) & 1 \end{bmatrix};$$

$$Y = \begin{bmatrix} x^{(0)}(2) \\ \cdots \\ x^{(0)}(n) \end{bmatrix}.$$

Therefore, the solution of the equation 5.23 is as follows:

$$x^{(1)}(t) = \left(x^{(0)}(1) - \frac{b}{a}\right) e^{-at} + \frac{b}{a} \tag{5.31}$$

The time response series of the differential equation is defined as follows:

$$x_F^{(1)}(k+1) = \left(x^{(0)}(1) - \frac{b}{a}\right) e^{-ak} + \frac{b}{a} \tag{5.32}$$

(3) Grey forecasting

In order to obtain the real data at time $(k+1)$, the Inverse Accumulated Generating Operation (IAGO) can be used, which is calculated as follows:

$$x_F^{(0)}(k+1) = x_F^{(1)}(k+1) - x_F^{(1)}(k) \tag{5.33}$$

$$x_F^{(0)}(k+1) = \left(x^{(0)}(1) - \frac{b}{a}\right) e^{-ak}(1 - e^a) \tag{5.34}$$

For prediction at any time $(k+n)$, it can be obtained as:

$$x_F^{(0)}(k+n) = \left(x^{(0)}(1) - \frac{b}{a}\right) e^{-a(k+n-1)}(1 - e^a) \tag{5.35}$$

However, as the accuracy of the grey model decreases when making predictions for a longer period into the future, usually the above equation for prediction at time $(k+n)$ is not used. Instead, a rolling GM (1, 1) model has been developed for long-term prediction (Kayacan, et al., 2010).

Generally, the rolling model will produce a prediction sequence based on the forward data. For instance, assuming that the forecast at time k, $x_F^{(0)}(k)$ has been obtained based on $x_F^{(0)}(k-1)$, $x_F^{(0)}(k-2)$, $x_F^{(0)}(k-3)$, $x_F^{(0)}(k-4)$, when making the forecast for the next period, $x_F^{(0)}(k+1)$, the data points used in the model will be

shifted by 1 period forward, namely $x_F^{(0)}(k)$, $x_F^{(0)}(k-1)$, $x_F^{(0)}(k-2)$, $x_F^{(0)}(k-3)$, keeping the next forecast as always based on the most recent 4 data points.

Furthermore, a grey model is also capable of handling time series observations with unequal intervals. Assuming an interval is Δt_k, unequal time intervals mean that times $\Delta t_1, \Delta t_2, \cdots, \Delta t_{n-1}$ are not always the same. To model an unequal grey sequence, the following steps are taken.

- Obtaining average interval;

$$l = \frac{(k_n)}{n-1} \tag{5.36}$$

Where,

k_n: total time interval of the time series at time n.

- Calculating the time difference between the actual and average time intervals;

$$d_k = (k-1) * l - (t_k - t_1) \tag{5.37}$$

- Transforming the original unequal sequence into a regular series with equal time interval.

$$x_1^{(0)}(k) = x^{(0)}(k) + \frac{d_k}{(t_k - t_1)} * \left(x^{(0)}(k) - x^{(0)}(k-1)\right) \tag{5.38}$$

Through the above 3 steps, a standardised equal interval time series can be created.

$$x_1^{(0)} = \left(x_1^{(0)}(1), x_1^{(0)}(2), x_1^{(0)}(3), \ldots, x_1^{(0)}(n)\right), n \geq 4, \tag{5.39}$$

The previously discussed processes GM (1, 1) modelling can be applied to the standardised data. After making the prediction on $x_1^{(0)}(k)$, the forecast original time series data $x^{(0)}$ can also be obtained by reversing the transformation steps.

$$x_F^{(0)}(k) = x_{1F}^{(0)}(k) - \frac{d_k}{l} * (x_{1F}^{(0)}(k) - x_{1F}^{(0)}(k-1)) \tag{5.40}$$

Where,

$x_{1F}^{(0)}(k)$: the forecast of $x_1^{(0)}$ at time k.

5.3 Summary

In this section, the main principles and procedure of the ARIMA model, multi-layer ANN model and grey model have been introduced in detail. For the ARIMA approach,

the Box-Jenkins method is the core component of the whole methodology. It provides guidance on the initial data preparation and a transformation that ensures that the input data can meet the requirements of the model. It also provides several rules for determining the orders of the ARIMA model as well as the parameters of the model, which will be used in the subsidence simulation in the following section when establishing the ARIMA model based on historical data. However, as these rules are only indicative principles, some judgement will be involved in the process.

In the artificial neural network model, the initial step of determining the structure of the neural network is relatively straightforward and there has been no clear evidence that the number of input neurons, hidden layers and hidden neurons on each hidden layer will have a significant impact on the performance of the model. The key part of the ANN model is the learning algorithm that it applies in determining the weights of each neuron. The working flow of gradient descent backpropagation has been explained in this chapter, which is mainly a process of minimising the prediction error through iterations and trials. This can provide a deep insight into the way in which the ANN model works. However, researchers do not really need to build up the algorithm by themselves, as it is already provided as a package in many statistical tools and the whole process can be run automatically.

The last model introduced in this section is the grey model. The method starts with grey sequence generation which is also the most critical part of this approach. It transforms the initial data into an inter-related sequence by means of the Accumulated Generating Operation, which can be modelled by the grey differential model. Then according to the solutions of the grey differential model, the grey sequence can be modelled and predicted, which finally leads to the prediction of the original data. Compared to the other two models, one notable advantage of the grey model is that it can handle time series with varying intervals. An example will be given in the subsidence simulation section below.

Chapter 6 Railway Subsidence Monitoring Case Study

6.1 Introduction

A case study based on the infrastructure of the High Speed One (HS1) railway in Britain is described in this chapter. The case study was conducted to assess the application of PS-InSAR in railway subsidence monitoring. This chapter begins with route configuration of the study area. The route of HS1 was selected for subsidence monitoring due to the tunnelling works which took place during construction, the geology and the weather of the study area. Later, this chapter presents the procedures for ordering radar data covering a period from June 2007 to September 2010. Following the data collection section, a tool for PS-InSAR processing is introduced. The subsidence monitoring result for HS1 is then presented in this chapter, including a time series analysis of selected PS along HS1 and the deformation profile of HS1. Based on the monitoring result, the subsidence status of HS1 will be assessed and railway sections with the potential for subsidence will be indicated.

6.2 Route Configuration

HS1, previously known as the Channel Tunnel Rail Link (CTRL), is a 109 km railway line from London St. Pancras International Station through Kent to the end of the Channel Tunnel in the UK (see Figure 6.1 (HS1, 2013)). HS1 is a ballasted railway and its design speeds are up to 230 km/h for domestic services and 300 km/h for international services (HS1, 2013).

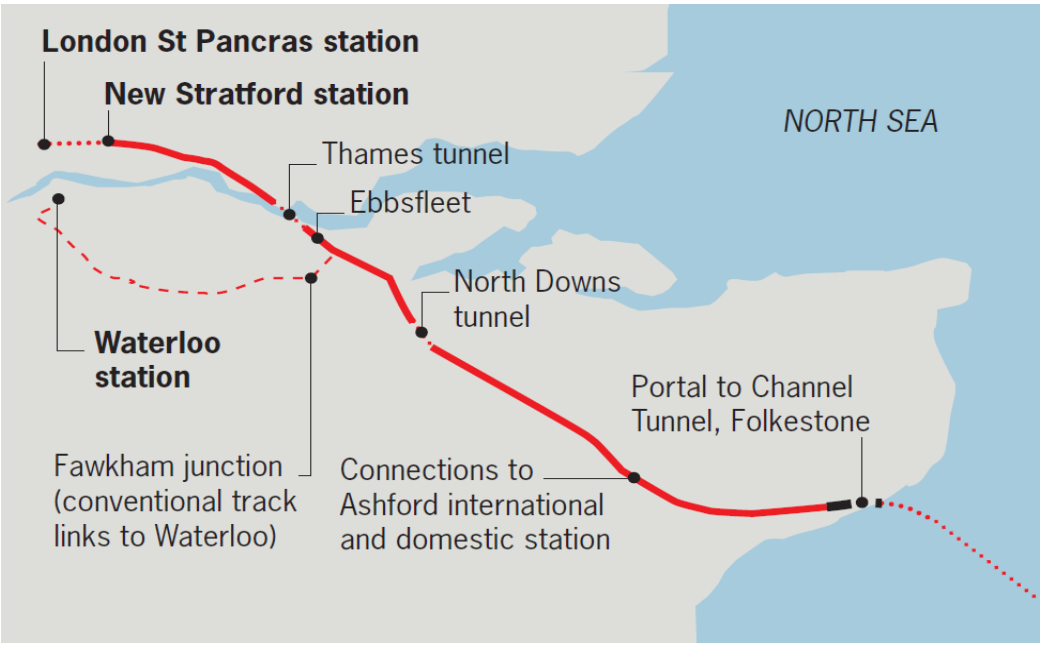

Figure 6.1: Route configuration of HS1

On 30 July 2003, the first Euro star train ran on Section 1 of HS1. Section 1 of HS1 runs 70 km from the Southfleet Junction near Ebbsfleet International Station in Kent to the UK end of the Channel Tunnel. As an extension of Section 1, Section 2 of HS1, which is 39 km from Southfleet Junction to London St. Pancras International Station, was put into operation in November 2007. HS1 enables passengers to travel from London to Paris in 2 hours and 15 minutes (Alstom, 2010).

Of the HS1 infrastructure, 85% is in the tunnel or next to a domestic railway, such as the Chatham Main Line and North Kent Line, or a trunk road, for example the M20 and M26 (The Committees of Public Accounts, 2012). As in any tunnel construction, the tunnelling work of HS1 and the adjacent infrastructure created a risk of subsidence for HS1. In addition, ground movement data collected from the North Downs Tunnel area which has a geology of chalk indicates the potential for larger ground movement compared with the movement of similar soft or hard rock conditions in the Midlands and North of England (High Speed Two (HS2) Limited, 2013).

The annual average rainfall for the area traversed by Section 1 of HS1 is more than 700 mm per year (NERC, 2008), which may also result in subsidence. For the reasons stated, Section 1 of HS1 is selected as the study area in this research.

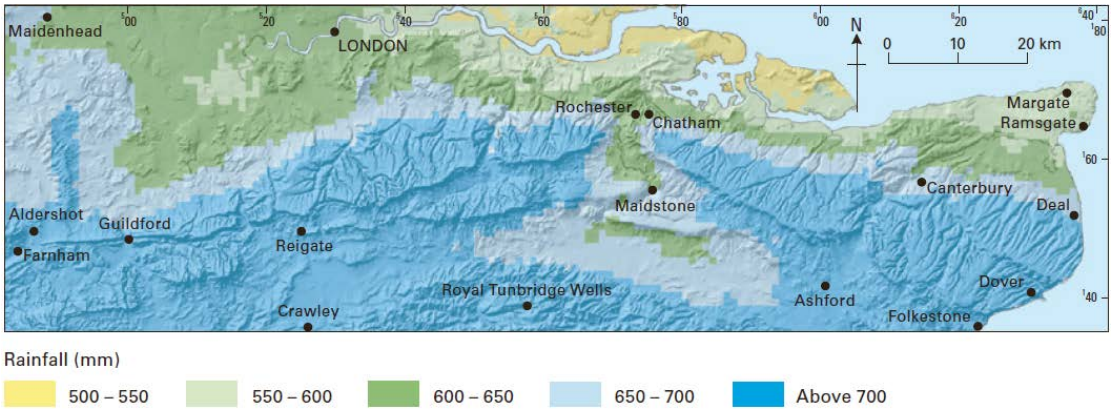

Figure 6.2: Annual average rainfall for the period 1961-1990

6.3 Data Collection

After considering the time to acquire the data, coverage, resolution and price of SAR images, Envisat Advanced Synthetic Aperture Radar (Envisat ASAR) data was selected for this research. The ASAR antenna of the Envisat satellite has five working modes which are image mode, alternating polarisation mode, wide swath mode, global monitoring mode and wave mode. The image mode of the ASAR antenna is able to obtain the SLC images with a 30 m spatial resolution and a 100 km swath width (GRAS, 2014). Due to the high spatial resolution and large image coverage, SAR images obtained by the image mode can be applied in ground subsidence monitoring.

6.3.1 Data Availability

The availability of Envisat ASAR data can be checked by the means of EOLI-SA. EOLI-SA is a free tool which enables users to check the availability of ESA's achieved earth observation data, and to order the data.

Users are able to refine the data request by defining the category of the data, the time interval of the data and the coverage. In this study, the category of the data is Envisat ASAR Image Mode. In addition, Section 1 of HS1 was put into operation on 30 July 2003. Therefore, the availability of the Envisat ASAR data captured after this date was checked in the EOLI-SA.

A part of Section 1 of HS1 was selected for subsidence monitoring. The length of this railway section is about 53 km. In terms of the data coverage, a quadrilateral area with a width of 35.13 km and a length of 48.90 km, which covers the relevant railway section, was selected. The coordinates of the corners of this quadrilateral are 51.460N0.301E, 51.143N0.301E, 51.460N0.875E and 51.143E0.875E respectively. The red curve in Figure 6.3 represents the selected HS1 railway and the purple rectangle indicates the Envisat ASAR data coverage in this research.

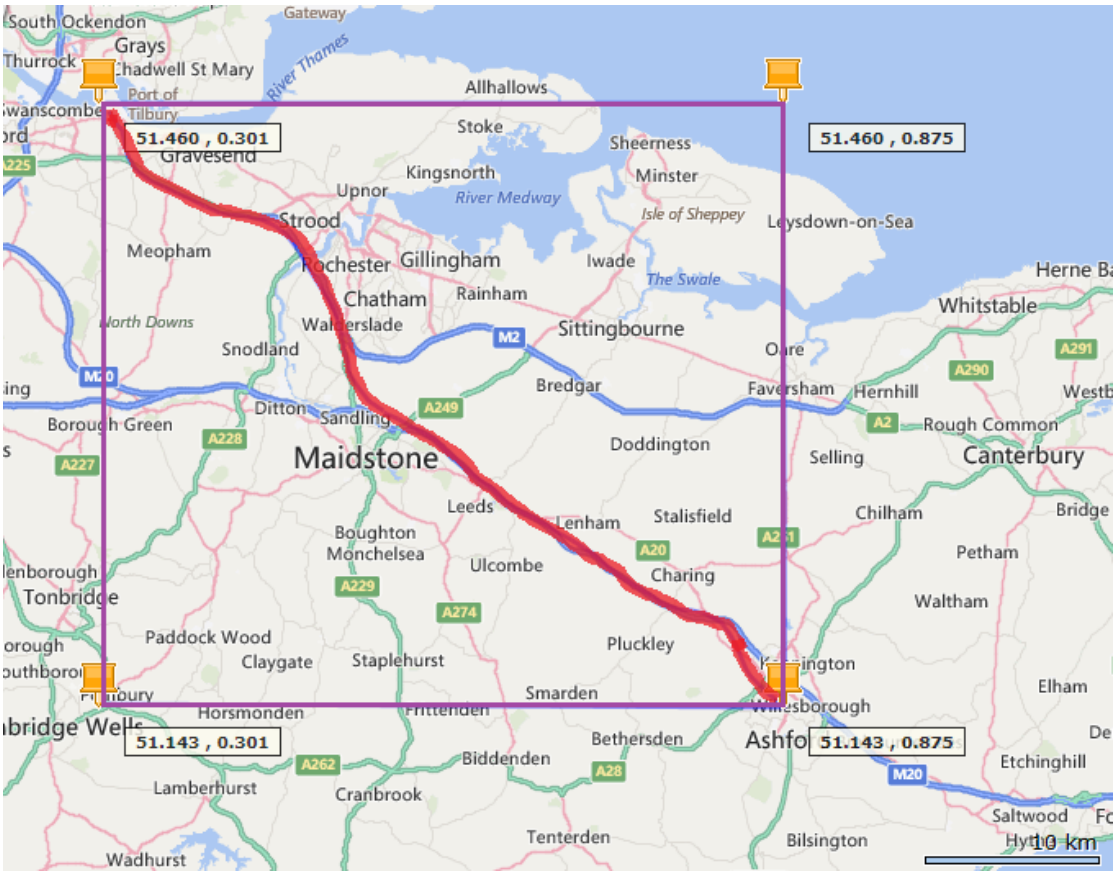

Figure 6.3: Location of the study railway route and Envisat ASAR data coverage

Once the study area was chosen, the data availability could be checked in EOLI-SA. The user interface of EOLI-SA is represented in Figure 6.4.

Figure 6.4: User interface of EOLI-SA

The pink rectangle indicates the defined study area while the green quadrilateral represents the coverage of the available Envisat ASAR data. 48 Envisat ASAR data which are all captured on track 51, are available to apply. A list of the 48 Envisat ASAR data sets can be found in Appendix A.

6.3.2 Data Ordering

To order data for an academic purpose, a research proposal which describes the research background and research plan must be submitted to the European Space Agency (ESA). After assessing the research proposal, the Envisat ASAR data ordered by the author of the proposal was supplied by ESA.

In addition to the spatial decorrelation caused by the long perpendicular baseline, long time intervals between two acquisitions of data will result in temporal decorrelation in the interferogram. For instance, the time interval for the two successive data sets which were captured on 02 December 2005 and 11 May 2007 respectively is 525 days, and vegetation changes on the ground during this period lead to temporal decorrlation. Accordingly, available data with appropriate temporal baseline and spatial baseline will be selected for railway subsidence monitoring.

In this study, Envisat ASAR data obtained after 11 May 2007 was selected for PS-InSAR processing. The data captured on 26 December 2008 was selected as the master image, based on the minimization of the temporal baseline and the spatial baseline, as well as the mean Doppler centroid frequency difference. The rest of the images are the slave images.

Once the master image was chosen, the perpendicular baseline of the image pairs could be checked. A perpendicular baseline of 800 m was applied for the image pair selection, as robust results were obtained with this dimension in previous research (Yan, et al., 2012) (Herrera, et al., 2009). Therefore, interferometric pairs with a perpendicular baseline of less than 800 metres were are selected in this research. Accordingly, 21 SLC images obtained by the Envisat ASAR antenna during the period of 15 June 2007 to 17 September 2010 were ordered from ESA in this study.

No.	Track	Orbit	Acquisition Date (dd/mm/yy)	Temporal Baseline (days)	Perpendicular Baseline (m)
1	51	27660	15/06/2007	-560	81.1
2	51	28161	20/07/2007	-525	119
3	51	28662	24/08/2007	-490	356
4	51	29664	02/11/2007	-420	372.3
5	51	31668	21/03/2008	-280	318.6
6	51	32670	30/05/2008	-210	102.4
7	51	33171	04/07/2008	-175	263.6
8	51	33672	08/08/2008	-140	432.9
9	51	34173	12/09/2008	-105	-448.9
10	51	34674	17/10/2008	-70	284.8
11	51	35175	21/11/2008	-35	-271.7
12	51	35676	26/12/2008	0	0
13	51	36177	30/01/2009	35	-306
14	51	36678	06/03/2009	70	471.2
15	51	37680	15/05/2009	140	176.1
16	51	40185	06/11/2009	315	369.8
17	51	41688	19/02/2010	420	-111.9

18	51	42189	26/03/2010	455	418.1
19	51	43692	09/07/2010	560	-126
20	51	44193	13/08/2010	595	103.1
21	51	44694	17/09/2010	630	511.1

Table 6.1: Envisat ASAR data from ESA

6.4 Data Processing Tool

The Stanford Method for Persistent Scatterers (StaMPS) is a free software package which was originally developed by Hooper and his colleagues at Stanford University in 2004. StaMPS was developed further at the University of Iceland, Delft University of Technology, and at the University of Leeds (Hooper , et al., 2013) (Hooper, et al., 2012).

StaMPS aims to monitor ground deformation over a large coverage area based on the time series analysis of PS selected within the monitoring area (Hooper, et al., 2012). Some free software, such as Doris, ROI_PAC, Triangle and SNAPHU, are integrated in StaMPS for SAR image processing, and users are able to apply them by using these programmes in StaMPS. Table 6.2 shows the function of each of the free software packages integrated in StaMPS.

Software in StaMPS	**Functions**
ROI_PAC	Generate SLC data with standard Committee on Earth Observation Satellites (CEOS) format from raw data
Doris	Read and coregistration of SLC data; DEM phase conversion; Interferogram generation
Triangle	Generate Delaunay Triangulation by persistent scatterers
SNAPHU	Phase unwrapping
MATLAB	PS-InSAR processing

Table 6.2: Function of each free software integrated in StaMPS

The raw data captured by ERS, Envisat and ALOS satellites is focused by means of ROI_PAC and can then be processed in StaMPS. For data processing starting with SLC images, the step of focusing can be skipped and the SLC images can be directly applied in Doris for interferogram generation. StaMPS is able to process SLC images acquired from ERS, Envisat, RADARSAT-1/2, TerraSAR-X and COSMO-SkyMed satellites (Hooper , et al., 2013). Envisat ASAR data obtained from ESA are SLC images, therefore the SLC images can be processed in StaMPS.

6.5 Railway Subsidence Monitoring Process

PS-InSAR processing for railway subsidence monitoring starts with the SLC data obtained from the Envisat ASAR antenna. A directory for SLC data is built and the data are stored in it for data processing. In addition, master SLC data is selected and all the SLC data are cropped based on the coverage of the study area.

Two-pass D-InSAR is then applied to the cropped master image and slave images, and interferograms are generated. In order to remove topography information from the interferogram, an external DEM obtained from SRTM is used to simulate the topographic phase in the interferogram. As a result, a stack of differential interferograms can be generated by differential interferometry of the interferograms generated from the SAR images and simulated magnitude image of the external DEM provided by Shuttle Radar Topography Mission 3 (SRTM 3).

In order to obtain a more reliable ground deformation result, PSC with good coherence over a long time period are selected from the interferograms based on the amplitude stability and phase stability. The signal contribution from neighbouring pixels of the PSC result in noisy PS pixel, therefore the noisy PSC must be dropped by PS weeding. In addition, DEM phase correction can be undertaken based on the estimated DEM errors. After phase unwrapping and phase filtering for spatially correlated error, ground deformation information can be extracted from the stack of differential interferograms. Figure 6.5 represents the ground deformation monitoring process by StaMPS based on PS-InSAR. The monitoring process is divided into the data pre-processing process, the D-InSAR process and the PS-InSAR process.

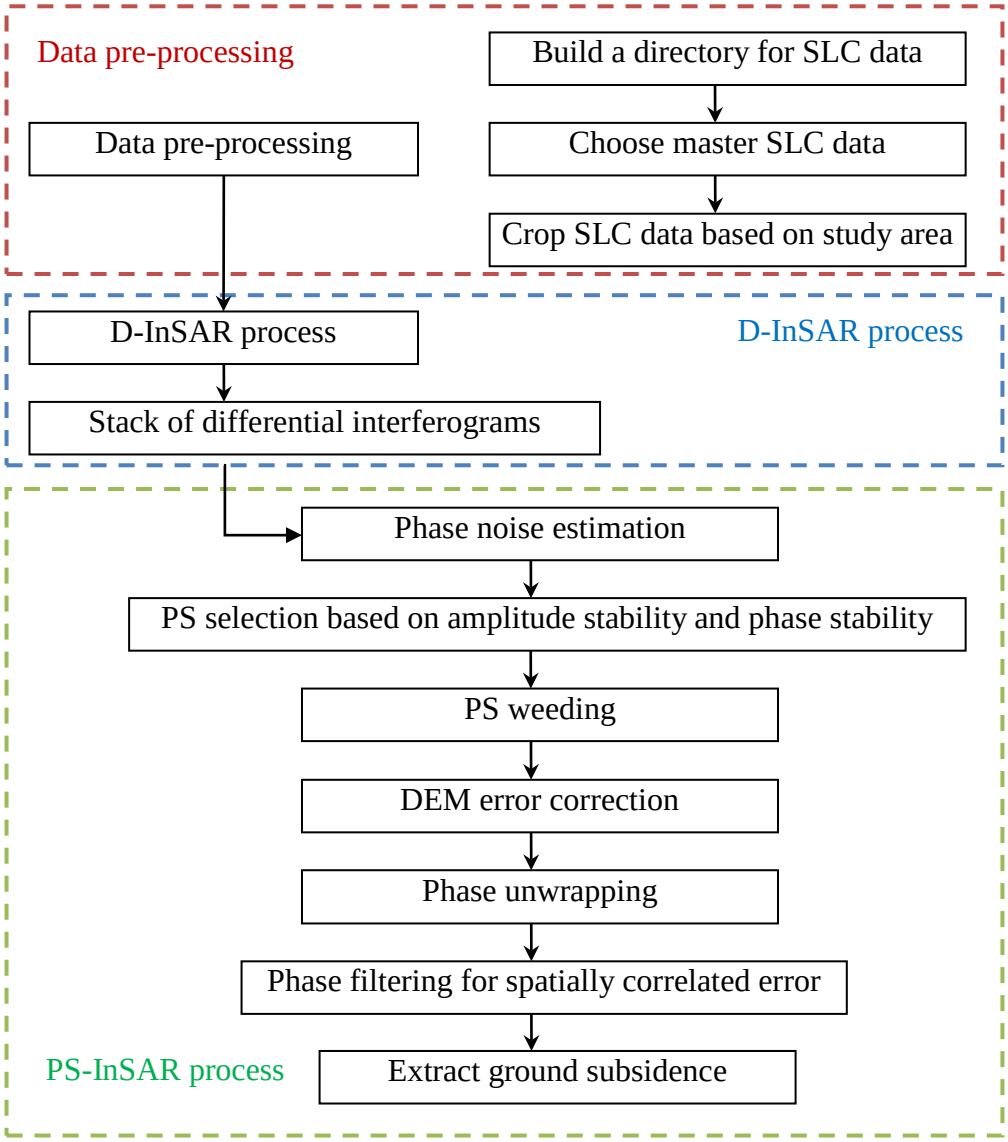

Figure 6.5: Railway subsidence monitoring process by StaMPS

In this case study, 21 SLC images captured by Envisat ASAR antenna are applied in StaMPS for PS-InSAR data processing. The 21 SLC images which were obtained during the period from 15 June 2007 to 17 September 2010 are listed in Table 6.1.

6.5.1 Data Pre-processing Process

In the data pre-processing step, the SLC image captured on 26 December 2008 was selected as the master image while the rest of the SLC images were considered as slave images. After cropping all the SLC images based on the study area, the 21 SLC images were ready for the D-InSAR process.

Figure 6.6 represents the cropped magnitude images for the selected dates. The magnitude image represents the topography of the study area, and contains the amplitude and phase information for each pixel of the SLC image. The magnitude image was generated at the time of reading the SLC image. In order to reduce speckle noise in the SLC image, a 4:1 multi-looking was applied to the image. The bright pixels on the magnitude image have the high signal to noise ratio (SNR) while the dark pixels have the low SNR.

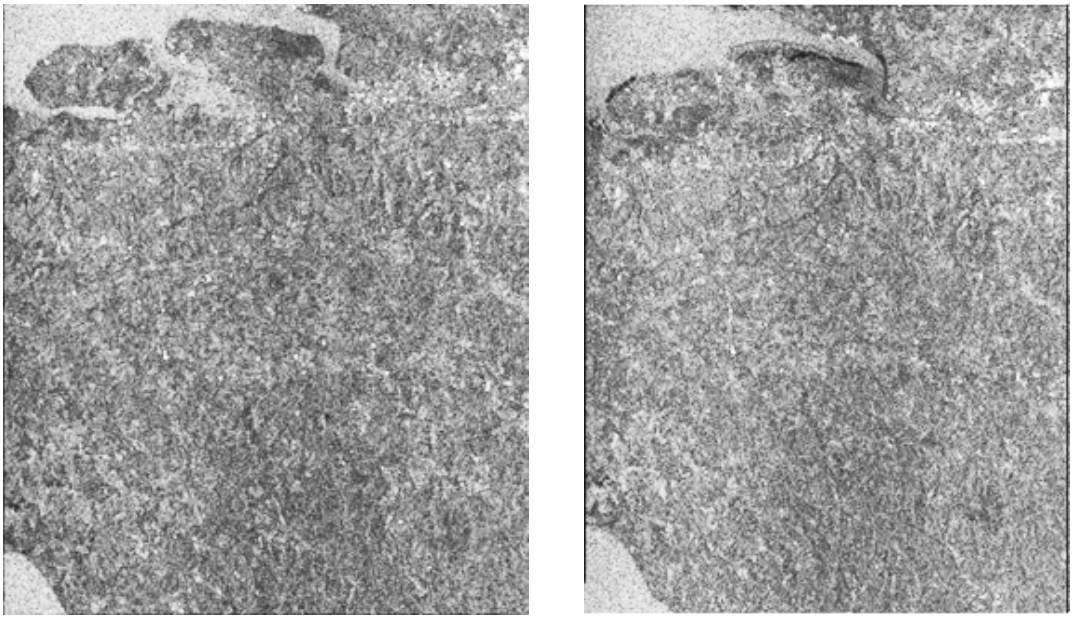

Figure 6.6: Cropped magnitude images of the master date 26/12/2008 (left) and slave date 01/30/2009 (right)

6.5.2 D-InSAR Process

Differential interferometry is carried out to remove topography information from the interferograms generated from the interferometric image pairs. One master image and 20 slave images were selected in this case study to form 20 image pairs and generate 20 interferograms. Figure 6.7 illustrates the 20 image pairs with temporal baseline and perpendicular baseline information.

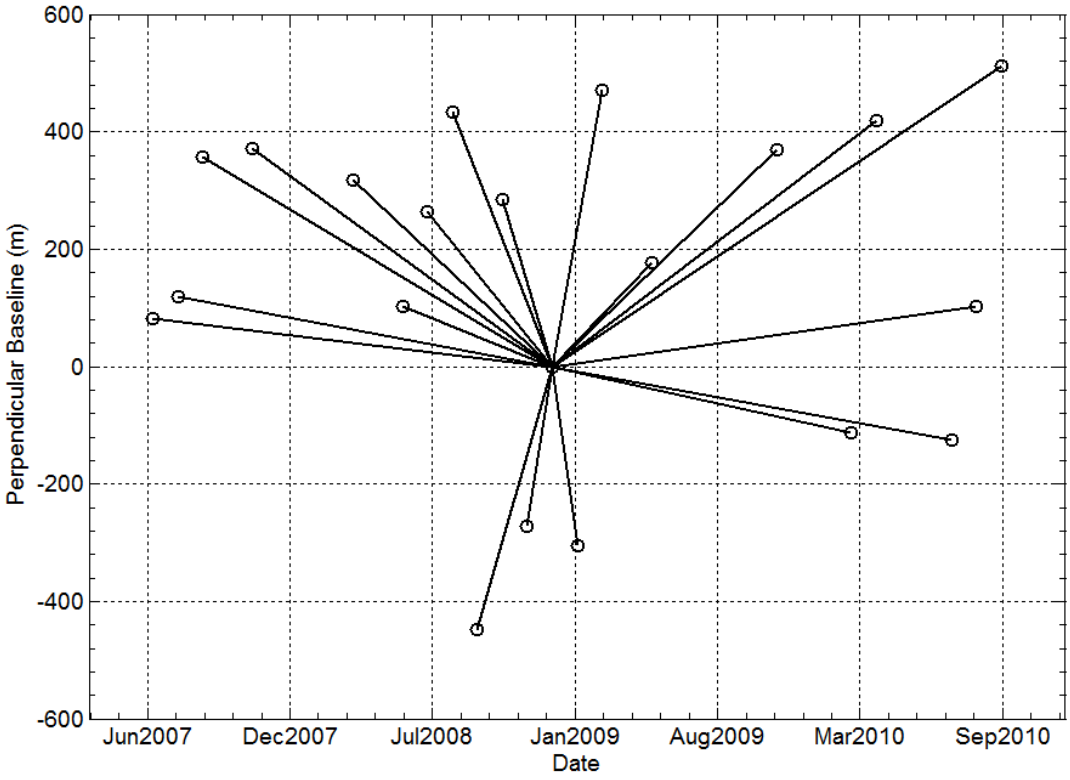

Figure 6.7: Temporal and perpendicular baselines of the image pairs

In this case study, a DEM provided by the SRTM 3 was adopted to the simulated topographic phase of the interferogram and remove topography information. The coordinates of the border points of the area covered by the downloaded DEM are 1.5W, 1.9E, 50.1S and 51.9N. Figure 6.8 is the simulated magnitude image of the DEM. It can be used for the coregistration with the SLC image.

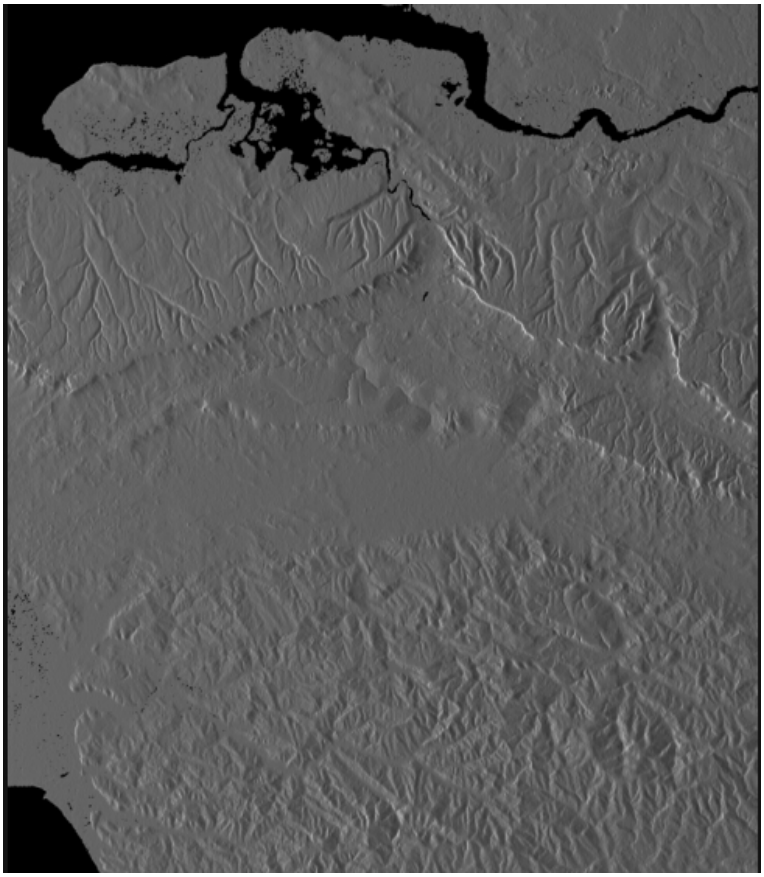

Figure 6.8: Simulated magnitude image of the DEM

After the coregistration, the simulated magnitude image of the DEM contains the topographic phase. As a result, topographic information can be removed from the interferogram generated from the SLC image pair by undertaking differential interferometry. Before removing the topographic phase, the flat earth phase was removed from the interferogram by precise orbit data of the radar. Figure 6.9 represents the interferograms after flat earth removal and topographic phase removal based on the interferometric image pair 26/12/2008 and 21/11/2008.

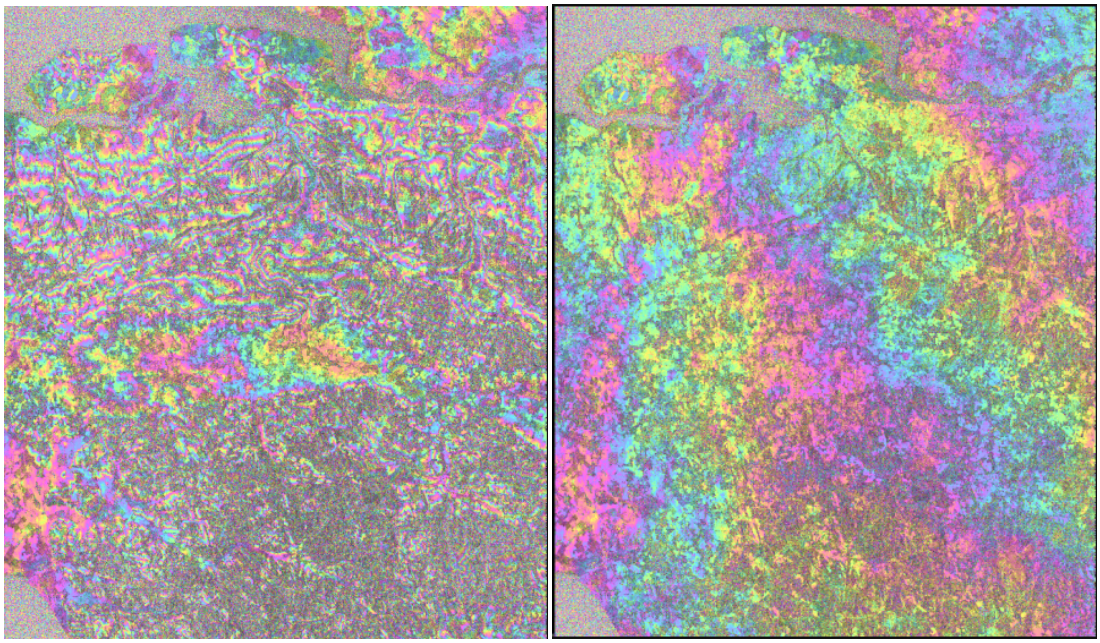

Figure 6.9: Flattened interferogram (left) and interferogram after topographic phase removal (right)

Based on the interferograms generated from the 20 selected interferometric image pairs and the topographic phase simulated by external DEM, 20 differential interferograms were created.

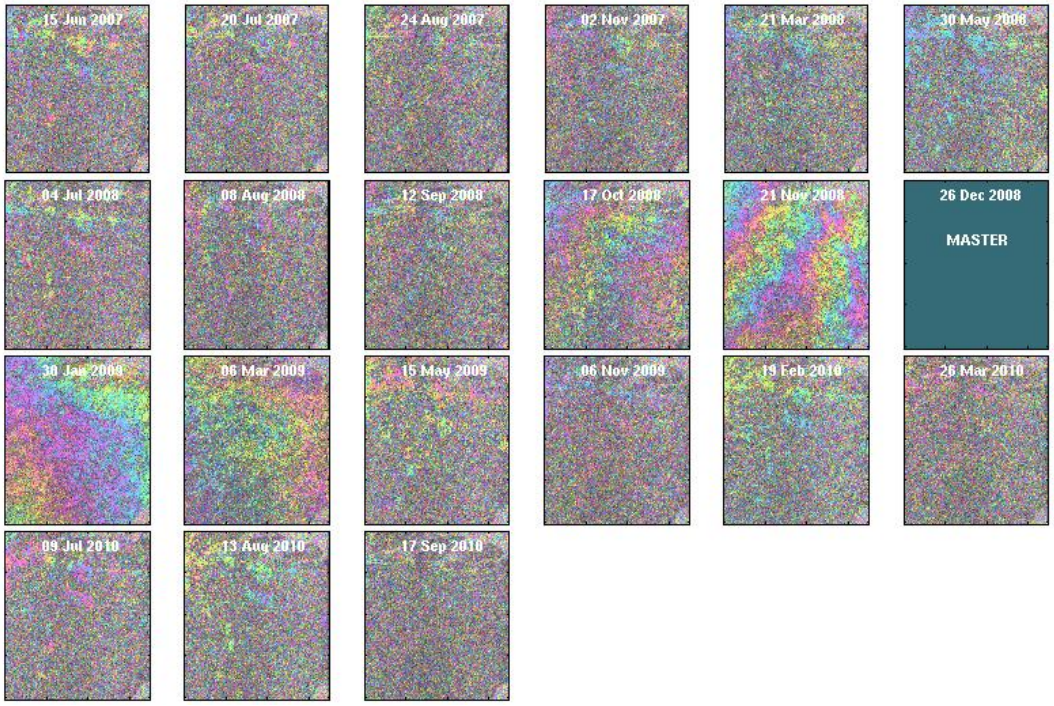

Figure 6.10: The 20 differential interferograms created in the D-InSAR process

6.5.3 PS-InSAR Process

(1) Selection of the Persistent Scatterer

As mentioned in Chapter 4, each pixel in the interferogram is represented by a complex number with amplitude and phase information. Amplitude and phase information indicates the strength of the radar echo and argument of the complex number. As a result, the radar echo of each PS pixel has stable amplitude and phase.

An approach based on the pixel amplitude stability is applied for the PS selection. A reasonable amplitude dispersion index is between 0.4 and 0.42, and 0.4 is selected for the amplitude dispersion index threshold in this case study. The scatterer within a pixel is selected as a PSC if its amplitude dispersion index is smaller than the threshold. Due to low SNR of scatterers (e.g. SNR<10 (Hooper, et al., 2004)) in vegetation areas, the relationship between the phase stability and amplitude dispersion will break down. As a result, the selected PSC is further selected based on the phase stability of the pixel. A coherence threshold of 0.3 is set for the PSC refinement in this research.

(2) Phase unwrapping result

Following the PS selection, 3D phase unwrapping is carried out based on the SNAPHU algorithm to obtain the real interferometric phase of each pixel in the interferogram. After removing the DEM error and orbital ramps, the unwrapped phase of each interferogram is represented in Figure 6.11. It is clear to see that the unwrapped phase of the second interferogram has a much wider range of radian, which means that the second interferogram has more errors in the phase unwrapping. To ensure the reliability of the time series deformation monitoring, the second interferogram with significant errors in phase unwrapping should be removed from the stack of differential interferograms.

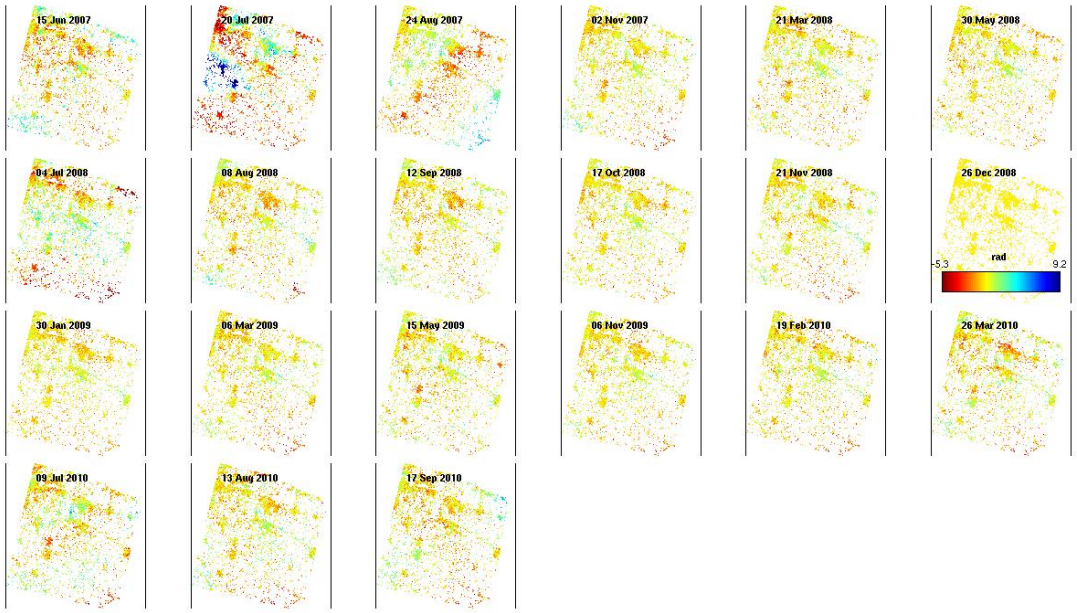

Figure 6.11: Unwrapped phase of each differential interferograms

Figure 6.12 shows the unwrapped phases of each differential interferograms after removing the second interferogram. Compared with Figure 6.11, the ranges of radian for each interferogram are more consistent. The 19 differential interferograms are then applied in time series deformation monitoring.

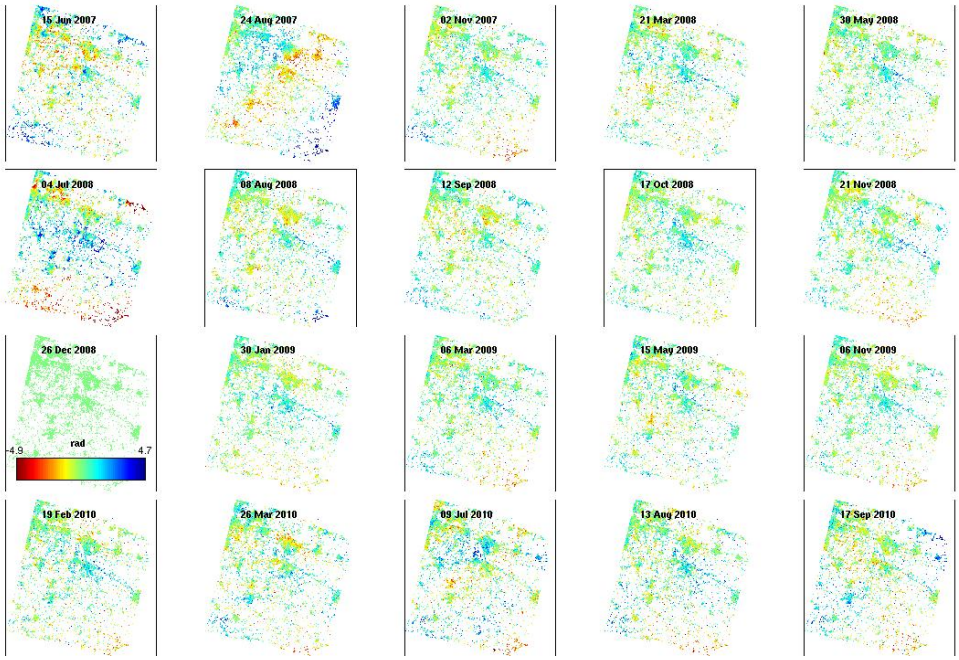

Figure 6.12: Unwrapped phase of each differential interferograms after removing the second interferogram

(3) Generation of the annual average deformation velocity map

High-pass filtering in time and low-pass filtering in space are applied to the pixels in the interferogram to remove the spatial correlated phase, such as atmospheric phase and orbit phase. After phase filtering, the ground deformation in the line of sight (LOS) direction can be extracted from the interferogram. Based on the stack of differential interferograms generated from the 19 image pairs, an annual average deformation velocity map of the study area is generated.

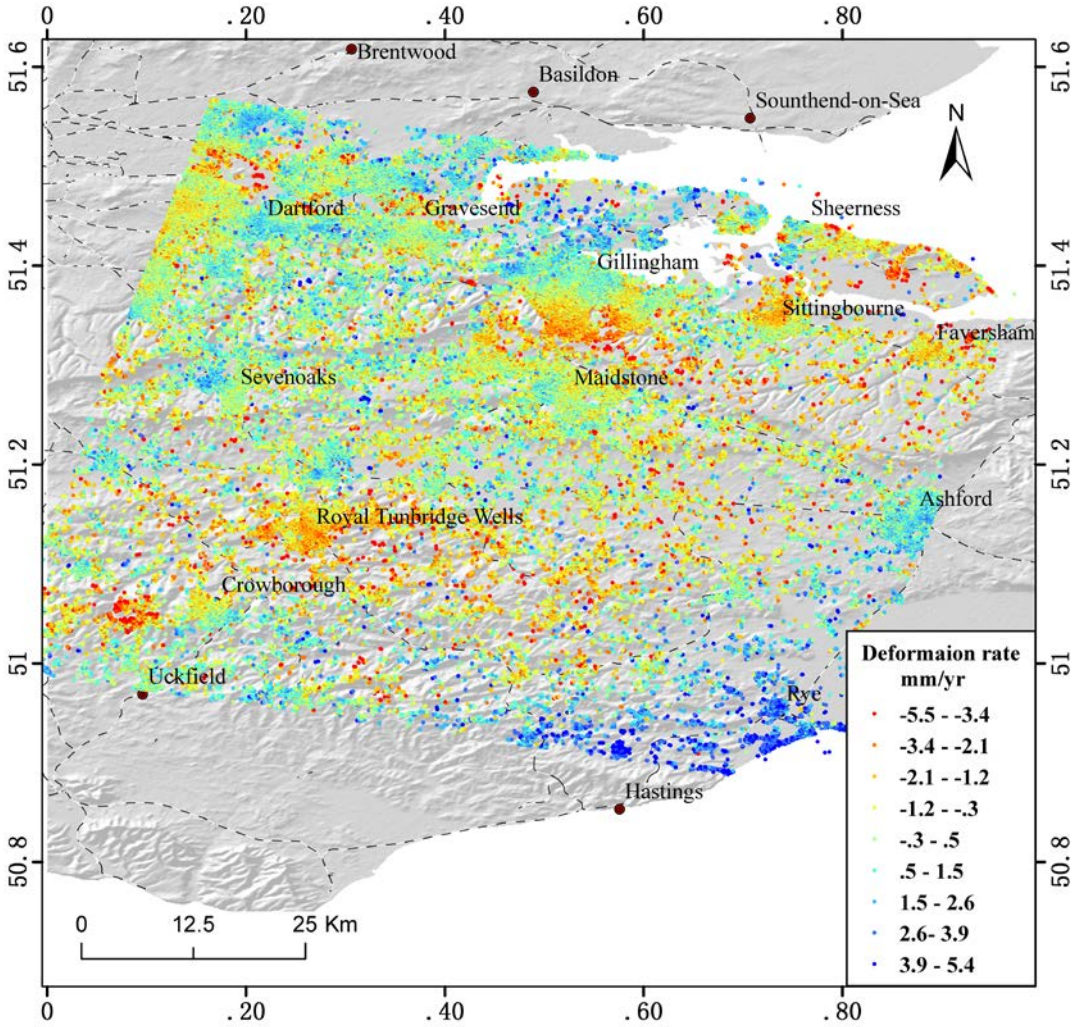

Figure 6.13: Annual average deformation velocity map

Figure 6.13 represents the annual average deformation velocity of the study area. On this map, a total of 179,745 PS were selected. Different colours refer to different deformation velocities. During the monitoring period, some PS rose and some PS fell. The deformation colour range for the PSs is from -5.5 to 5.4 mm per year. For example, the red PS means that this PS subsided 5.5 mm per year.

The deformation velocity data of the PS along the HS1 route indicates that no large scale deformation occurred on the selected section of HS1 during the monitoring period.

(4) Time series analysis of the selected PS

For any PS within the study area, a time series deformation analysis can be carried out based on the historical records of the PS deformation during the monitoring period. Three PS, which are PS1, PS2 and PS3, are selected to show the results of the time series deformation analysis.

In order to eliminate the error in the deformation monitoring result, a square centred on the selected PS with a width of 600 m was created. As well as the selected PS, other PS may be located within this square. Accordingly, the time series deformation records of the selected PS can be estimated based on the mean of the time series deformation records of all the PS within this square.

Figure 6.14, Figure 6.15 and Figure 6.16 show the time series deformation analysis for the three selected PS. The small circles indicate the time series deformation records of the PS during the monitoring period. The position of the PS in the LOS direction on the date when the first SLC image was captured is considered as 0 mm. Accordingly, the slope of the line between the two circles is negative if the PS subsided and vice versa.

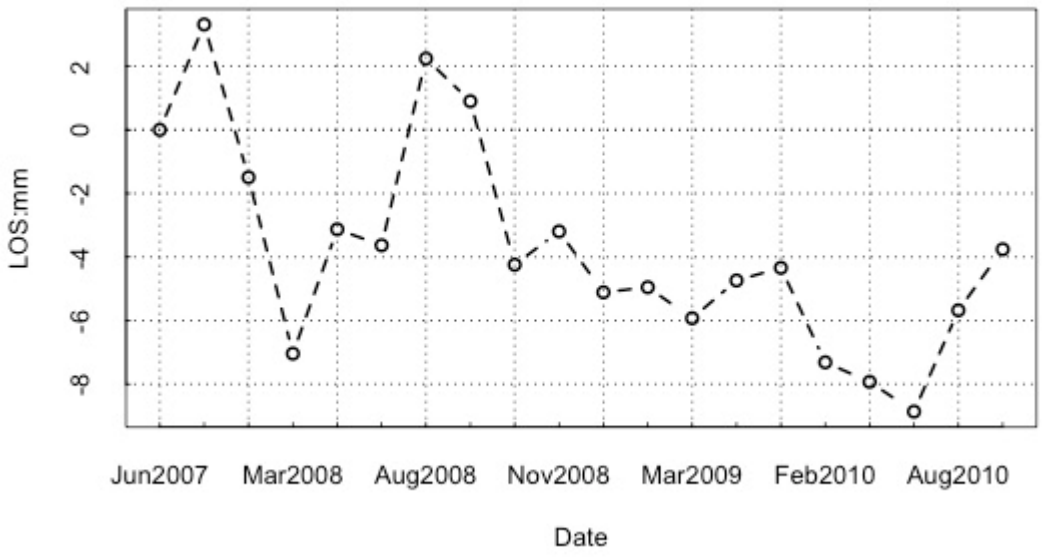

Figure 6.14: Time series deformation analysis of selected PS1

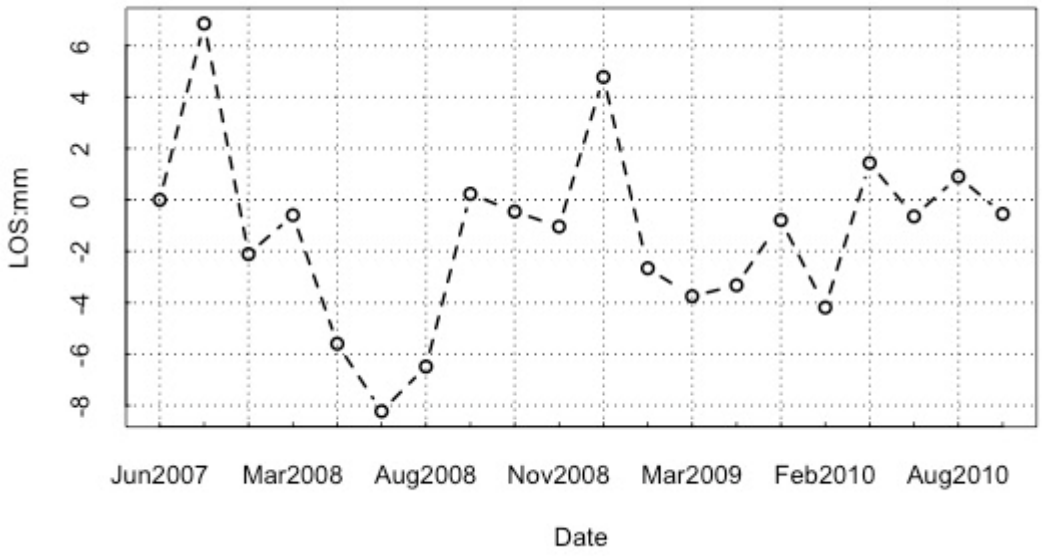

Figure 6.15: Time series deformation analysis of selected PS2

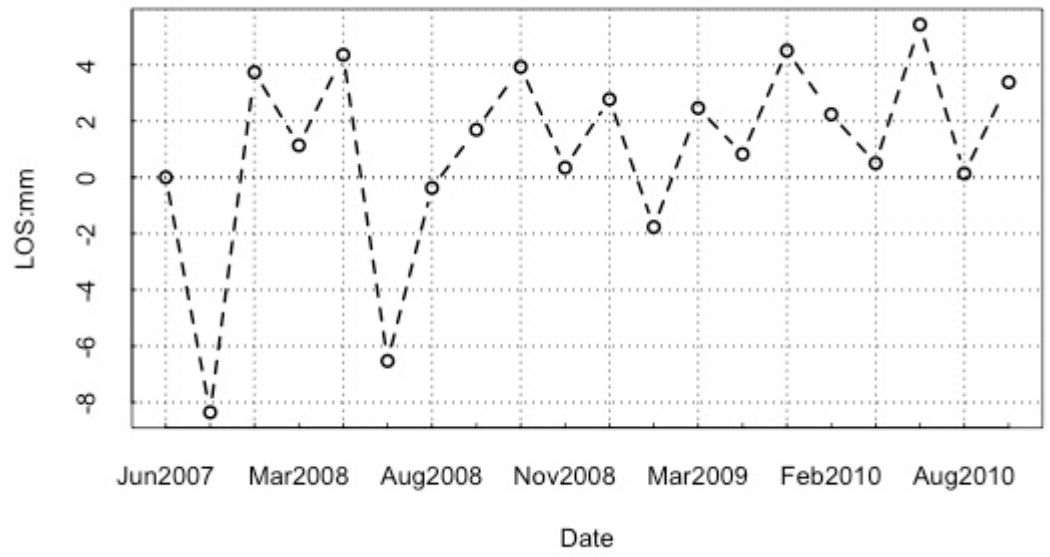

Figure 6.16: Time series deformation analysis of PS3

Figure 6.14, Figure 6.15 and Figure 6.16 for the three PS have revealed three typical deformation trends occurring along the target railway. A common feature among these trends is that the deformation is relatively significant during the beginning period and then becomes to stable at later stages. For the area around the PS1, the general trend is subsiding, while the ground of PS3 is slightly uplifting. Unlike these

two PS, there is no consistent trend for PS2. It has experienced both subsiding and uplifting during the observation period. The deformation levels of the three PS at the end of the selected period were all within the range of -4 mm to 4 mm.

(5) Deformation monitoring results on Google Earth

Deformation monitoring results of the study area can be represented on Google Earth. Figure 6.17 illustrates all the PS within the study area with the information of their annual average deformation velocities and locations. The annual average deformation velocity has the same colour scale as the Figure 6.13.

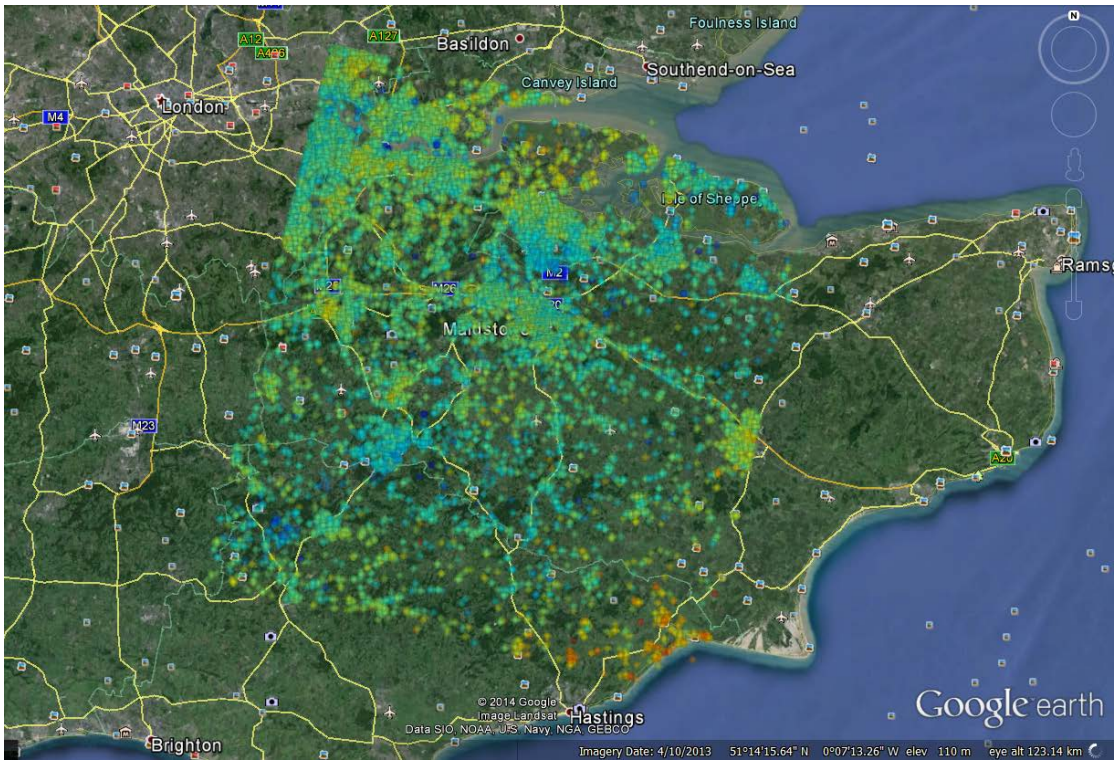

Figure 6.17: Annual average deformation velocity map on Google Earth

PS along HS1 can be easily found by zooming in the map above. In Figure 6.18, several PS along HS1 are represented on a Google Earth image. The annual average deformation velocity of the PS and its coordinates can be obtained by clicking on these PS. For instance, the selected PS subsided 3.3 mm per year during the monitoring period.

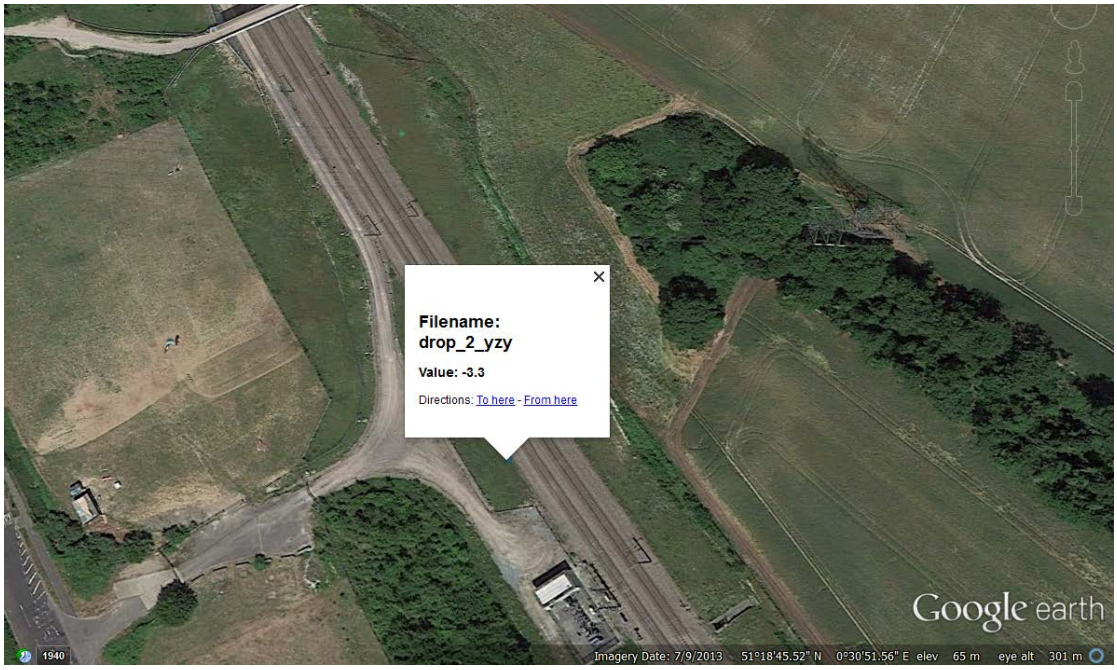

Figure 6.18: Annual average deformation velocity of PS on Google Earth

According to the annual average deformation velocity and coordinates of this PS, deformation records can be extracted from the deformation monitoring result and a time series deformation analysis can be conducted.

6.5.4 Railway Subsidence Monitoring Result

Table B. 1 in Appendix B represents the annual average deformation velocities of the PS along HS1. A positive result means the PS rose while the negative result means the PS fell during the monitoring period. Deformation velocities of HS1 sections shown in red are the areas which have potential subsidence.

Based on the deformation velocity and coordinates of the PS along HS1, a deformation profile of HS1 can be created.

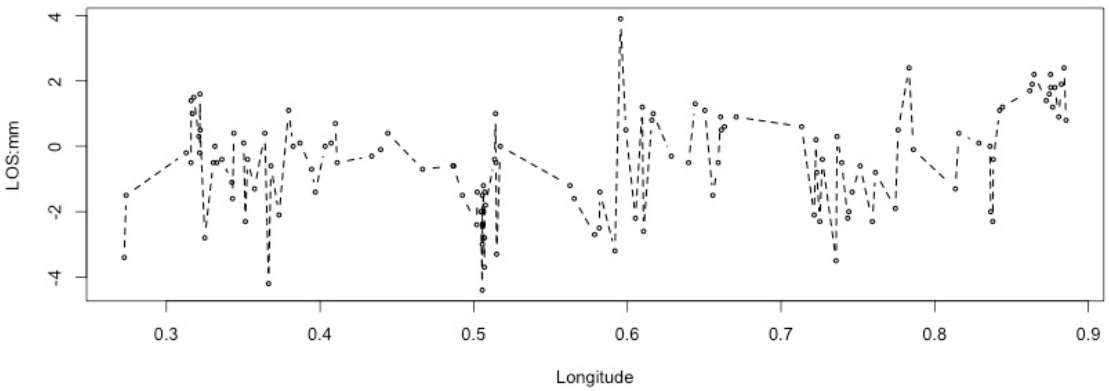

Figure 6.19: Deformation profile of selected sections of HS1

This deformation profile indicates that deformation velocities of the PS along HS1 in LOS direction are between -4.4 mm per year and 3.9 mm per year. This range of deformation identifies that HS1 was generally stable during the monitoring period and that a safe operation of HS1 could be ensured by the stable railway infrastructure. However, potential subsidence should be monitored. For instance, the North Downs tunnel area has a subsidence velocity in LOS of up to 4.4 mm per year (see Table 6.3) while the subsidence velocity in LOS for the railway section between Hockers Lane Overbridge and Water Lane Underbridge is up to 3.2 mm per year (see Table 6.4).

The ground deformation results obtained from PS-InSAR were showed in the LOS direction. In order to obtain ground deformation in vertical direction, the ground deformation value in the LOS direction should be projected on the vertical direction. The look angle of the Envisat ASAR data used in this case study is 23.3°. Based on ground deformation results and the geometry of radar imaging (see Figure 4.2), vertical ground deformation results can be obtained.

PS No.	Deformation velocity (mm/y)		Coordinates	
	LOS	Vertical	North (N)	East (E)
North Downs Tunnel (Entrence)				
44	-2.4	-2.2	51°20'26.01"N	0°30'7.10"E
45	-1.4	-1.3	51°20'18.57"N	0°30'8.31"E
46	-3.7	-3.4	51°20'9.83"N	0°30'25.01"E
47	-2.4	-2.2	51°20'8.80"N	0°30'21.99"E

48	-2.0	-1.8	51°20'3.67"N	0°30'16.59"E
49	-2.0	-1.8	51°20'1.66"N	0°30'23.09"E
50	-4.4	-4.0	51°19'58.75"N	0°30'20.01"E
51	-3.0	-2.8	51°19'56.96"N	0°30'20.27"E
52	-2.8	-2.6	51°19'55.44"N	0°30'25.20"E
53	-1.5	-1.4	51°19'54.30"N	0°30'20.18"E
54	-1.8	-1.7	51°19'50.03"N	0°30'27.37"E
55	-1.2	-1.1	51°19'16.87"N	0°30'22.67"E
56	-1.4	-1.3	51°19'13.45"N	0°30'25.91"E
North Downs Tunnel (Exit)				

Table 6.3: Summary of the railway deformation in North Downs Tunnel area

PS No.	**Deformation velocity (mm/y)**		**Coordinates**	
	LOS	**Vertical**	**North (N)**	**East (E)**
Hockers Lane Overbridge				
64	-2.7	-2.5	51°17'3.95"N	0°34'43.17"E
65	-2.5	-2.3	51°16'58.56"N	0°34'54.30"E
Thurnham Lane Underbridge				
66	-1.4	-1.3	51°16'58.89"N	0°34'55.72"E
67	-3.2	-2.9	51°16'39.89"N	0°35'30.91"E
Water Lane Underbridge				

Table 6.4: Summary of the railway deformation between Hockers Lane Overbridge and Water Lane Underbridge

In addition, as it is an important transportation junction of HS1, the stability of Ashford International Station is critical to the safe operation of HS1. The railway subsidence monitoring result obtained from this case study also indicates some of the ground movement of Ashford International Station. According to Table 6.5, the deformation velocities of all the PS around Ashford International Station are positive and there is no obvious fluctuation in the data. Accordingly, although the ground

movement of Ashford International Station is rising slowly, it is generally stable as indicated by the railway subsidence monitoring result in this case study.

PS No.	Deformation velocity (mm/y)		Coordinates	
	LOS	Vertical	North (N)	East (E)
Ashford International Station (Entrance)				
113	1.7	1.6	51° 8'55.61"N	0°51'42.83"E
114	1.9	1.7	51° 8'52.86"N	0°51'48.56"E
115	2.2	2.0	51° 8'49.95"N	0°51'52.75"E
116	1.4	1.3	51° 8'41.64"N	0°52'21.26"E
117	1.6	1.5	51° 8'38.84"N	0°52'28.30"E
118	2.2	2.0	51° 8'36.89"N	0°52'31.40"E
119	1.8	1.7	51° 8'35.45"N	0°52'32.06"E
120	1.2	1.1	51° 8'32.51"N	0°52'36.40"E
121	1.8	1.7	51° 8'29.07"N	0°52'41.43"E
122	0.9	0.8	51° 8'26.87"N	0°52'50.69"E
123	1.9	1.7	51° 8'20.30"N	0°52'56.81"E
124	2.4	2.2	51° 8'16.80"N	0°53'3.10"E
125	0.8	0.7	51° 8'15.15"N	0°53'7.77"E

Table 6.5: Summary of the railway deformation at Ashford International Station

PS-InSAR is able to detect millimetre vertical ground deformation in both precision and accuracy. However, due to limitations of D-InSAR, precision and accuracy of PS-InSAR will be affected. The main errors of PS-InSAR results come from phase noise of the interferogram, such as flat earth effects, topographic effects, atmospheric delay, orbit error and random phase noises. In addition, temporal and spatial decorrelation also contributes the precision and accuracy of PS-InSAR results.

In addition, historical levelling survey data or GPS data which recorded the deformation of HS1 can be used to assess the accuracy of the subsidence monitoring results conducted by PS-InSAR. However, Network Rail (High Speed) who operates and maintains HS1 on behalf of HS1 Ltd have not maintained any levelling or GPS records for HS1 since the start of its operation. Although the subsidence monitoring

results can not be assessed by historical deformation records, High Speed Two (HS2) Ltd have stated that a larger ground movement occurred in the North Downs Tunnel area based on the ground movement data compared with the movement of the similar rock conductions in Midlands and North of England (High Speed Two (HS2) Limited, 2013). In addition, the Network Rail (High Speed) Outside Parties Development Handbook indicated that except for minor settlement which occurred in the construction period of HS1, there was no settlement throughout the HS1 route (Network Rail (High Speed) Ltd, 2013). These two reports can support the conclusions of the case study.

The results of this case study showed ground subsidence in North Downs tunnel area and railway section between Hockers Lane Overbridge and Water Lane Underbridge, and ground heave at Ashford International Station. Adjacent infrastructures, geology and weather conditions are main contributors to different deformation results in HS1 railway sections. Although no large scale subsidence has occurred on HS1, in order to ensure safe the operation of HS1 in the future and reduce life cycle costs, more frequent subsidence monitoring work and maintenance work should be conducted, especially on the sections of HS1 with potential subsidence. A proper maintenance plan for HS1 can be made based on the prediction results for the subsidence trends of HS1 in the future. A case study which predicts the subsidence trends of HS1 by time series prediction models will be undertaken in Chapter 7.

6.6 Summary

A case study which assessed the subsidence status of the HS1 route was conducted in this chapter. A 53 km long railway section of HS1, which is from Southfleet Junction near Ebbsfleet International Station to Ashford International Station, was chosen as the study railway. Envisat ASAR data obtained between June 2007 and September 2010 were used for railway subsidence monitoring.

After conducting PS-InSAR based on Envisat data, the deformation profile of the selected railway was generated. According to the railway subsidence monitoring result, large scale ground movement did not occur on HS1 and this railway is still stable after over 10 years of operation. Although the infrastructure of HS1 is generally stable, some areas indicated the potential for subsidence compared with the rest of the

HS1 route. For instance, vertical subsidence velocities of the North Downs Tunnel and the railway between Hockers Lane Overbridge and Water Lane Underbridge were up to 4.0 mm per year and 2.9 mm per year respectively. In addition, the results of railway subsidence monitoring also indicate good ground stability around Ashford International Station, although the land is generally rising.

Based on the subsidence monitoring result, frequent monitoring work should be conducted on the railway sections with potential subsidence. In addition, a railway subsidence prediction model which indicates the trend of railway subsidence can be used for subsidence prediction on the HS1 route. Moreover, a maintenance plan should be made for HS1 based on the prediction result to ensure the safe operation of HS1 and to reduce maintenance costs.

Chapter 7 Railway Subsidence Prediction Case Study

7.1 Introduction

In the prediction section, the subsidence data obtained from PS-InSAR will be used as the input data for the time series models discussed previously. The prediction simulation will be divided into two parts. The first part is to model the time series based on equal intervals, while the other is to work on an uneven time series. R is employed as the statistical tool to conduct the simulation. The subsidence data will need to be imported into R, as they are originally stored in a MATLAB data file.

For the subsidence time series with equal intervals, the simulation will be carried out with the Auto-Regressive Integrated Moving Average (ARIMA) model, an artificial neural network (ANN) model and a grey model. The modelling procedure introduced in Chapter 5 will be implemented through specific packages in R. A comparison between the performances of the three models will then be provided after the simulation is finished, where the root mean square error (RMSE) is adopted as the measure to assess the simulation results of these models.

The second part of the simulation only involves a grey model as it is the only model of the three that is capable of handling time series with unequal intervals. The main procedure is similar to that for the equal-interval time series, with one additional step at the beginning to transform the original data from the unequal interval series to an equal interval one with the algorithm mentioned in the Chapter 5.

7.2 Input Data

All the time series prediction models mentioned earlier only work for observations with equal intervals. If the time series has unequal intervals, it will usually need to be transformed into an equal-interval series before being modelled. For this simulation, 125 persistent scatters (PS) were selected and each of them had 19 valid observations

over 3 years. The standard time interval for these observations was 35 days. However, only the time series sequence from the 5th observation to the 12nd observation has a constant interval of 35 days, while the intervals between the other observations are not always 35 days. Therefore, the sub subsidence series, which includes 9 observations ranging from the 5th observation to the 12nd observation plus the benchmark point, was chosen to be the input for the first simulation on the equal interval time series.

In the second simulation, all 19 observations are selected and the whole series will be transformed into a new time series with equal intervals, where the subsidence data are weighted based on the size of their original intervals.

Usually, the best practice in time series prediction is to divide the input data into the training set and the validation set. However, as insufficient observations could be obtained for this research, all the input data are used as the training set and only the performance of the training set is assessed and compared.

7.3 Equal Interval Subsidence Series Simulation

7.3.1 ARIMA Model

The package 'forecast' in R can be used to perform the ARIMA modelling. According to the typical process, the first step is to check the auto correlation function (ACF) and partial auto correlation function (PACF) in order to determine the orders of the ARIMA model. Taking the 25th PS as an example, which exhibits one of the most significant subsidence values, its ACF and PACF plots are shown in Figure 7.1. The dotted line is the 95% confidence interval by default.

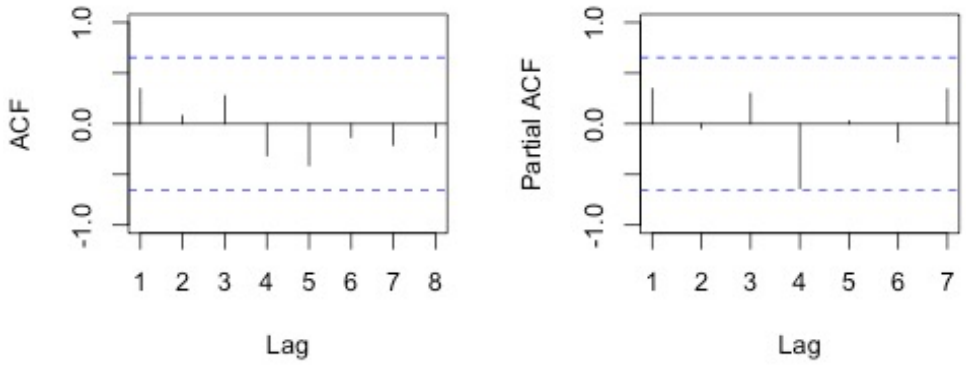

Figure 7.1: ACF and PACF Plots

According to the ACF plot, there are no significant positive autocorrelations within a high number of lags. Therefore, no further differencing needs to be made. Moreover, in both the ACF and PACF plots, there is no spike among the lags, meaning the time series is already quite random and close to white noise. This might be due to the fact that either there are not enough data points available for the model or the series itself is close to white noise. In this case, the ARIMA model is not perfectly suitable for modelling. However, in order to evaluate the suitability among various modelling methods, the ARIMA model is still used and the most applicable type of model is ARIMA (1,0,0). The results of the simulation are shown as follows:

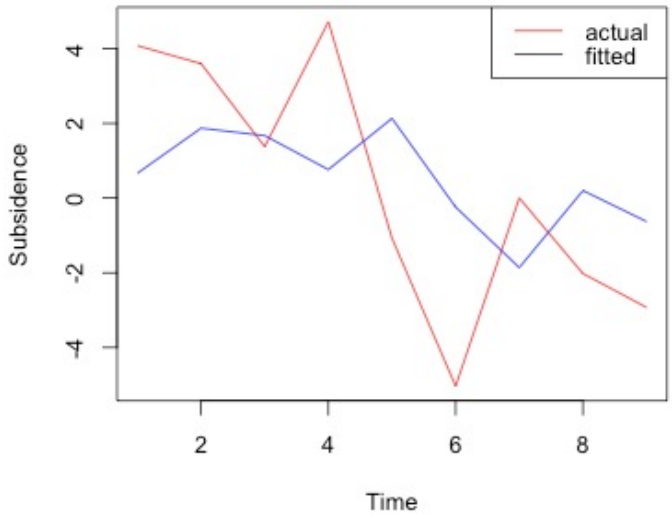

Figure 7.2: Actual subsidence vs. predicted subsidence in ARMA

For some of the time points, the performance of the ARIMA model is not entirely satisfactory, particularly when the subsidence value changes dramatically. The root mean square error (RMSE) is 2.9304.

Ideally, the same process should be applied to each of the PSs. However, when there are too many PSs, it is impossible to undertake the process manually. The Forecast package in R provides an automatic ARIMA function that can determine the order of ARIMA automatically, based on certain criteria. After applying the automated ARIMA modeling for all the remaining PSs, the total RMSE is 454.847.

7.3.2 Neural Network Model

The package ‘nnet’ in R is one of the most widely used tools for artificial neural network modelling. As introduced in Chapter 5, the structure of the ANN is the primary factor that needs to be determined. For the time series, the input neurons are previous observations. Based on the number of available observations, 3 input neurons are chosen. Numerous studies have revealed that the number of hidden neurons will not impact the performance of the model significantly. It should usually be smaller than the total number of input and output neurons. Therefore, 3-hidden neurons are also selected. Sometimes, in order to determine the optimal number of input and hidden neurons, a sensitivity analysis can be undertaken based on the varied number of input and hidden neurons in order to minimise the total prediction errors.

After determining the structure of the ANN model, the ‘nnet’ function is utilised to train the model. The maximum number of iterations is set to 1000. As there are 3 input neurons, the ANN model can produce fitted values for the 4^{th} time point to the 9^{th} time point. The plot below shows both the actual subsidence and the fitted subsidence value produced by the ANN model for the 25^{th} PS.

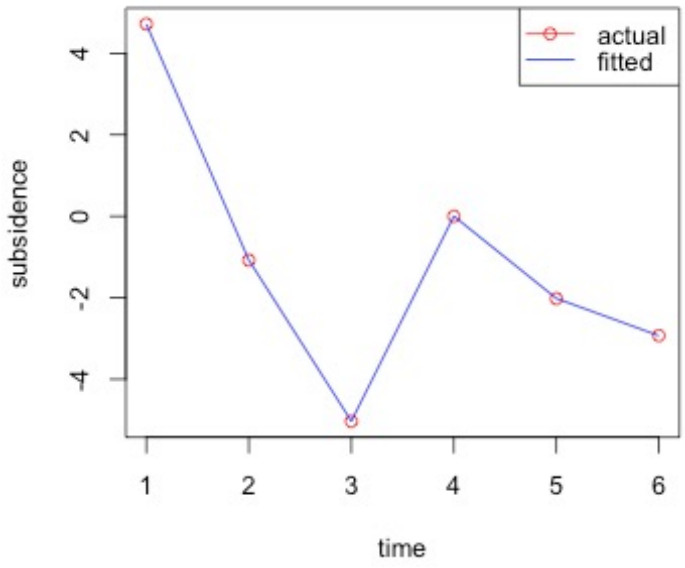

Figure 7.3: Actual subsidence vs. predicted subsidence in neural network

Compared to the ARIMA model, the neural network model fitted much better with its RMSE amounting to 0.0035. The same training process was then applied to the remaining PSs and the total RMSE result was 110.966.

7.3.3 Grey Model

There is no package specifically for grey modelling in R. However, the algorithm can be constructed using basic R codes. A great feature in R is that apart from the basic functions originally embedded in R, users can also define their own functions. In grey modelling, the first step is to create 2 important functions, i.e. the Accumulated Generating Operation (AGO) and the operation to obtain the means between adjacent data points generated by AGO. Then these 2 functions are applied to the subsidence data, which produces the grey data for modelling. For the 25th PS, the performance of the grey model is shown below:

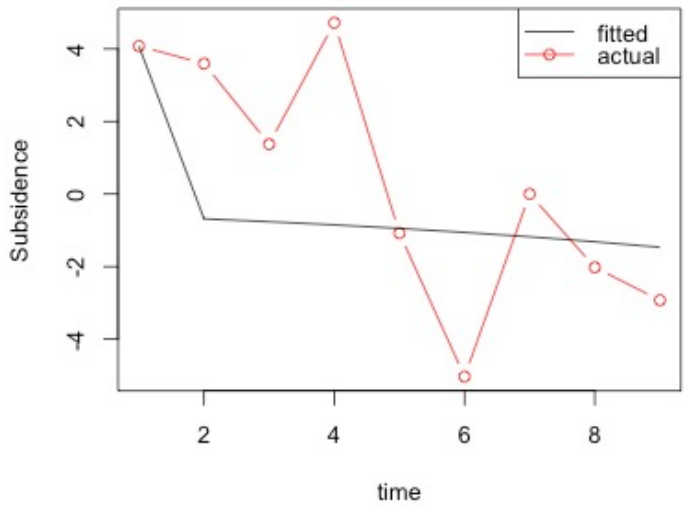

Figure 7.4: Actual subsidence vs. predicted subsidence in grey model

The RMSE is 2.8622. As carried out for the ARIMA and NNS models, the same modelling process is applied to all the PSs and the total RMSE is 531.316.

7.4 Unequal Interval Subsidence Series Simulation

As mentioned earlier, the whole subsidence series is not an equal interval time series. Its intervals are as follows:

Interval	1	2	3	4	5	6	7	8	9	10	11	12	13	14	15	16	17	18	19
Days	70	70	140	70	35	35	35	35	35	35	35	35	70	175	105	35	105	35	35

Table 7.1: Time intervals

According to the transformation technique provided by the grey model, the original series was transformed into a new series with equal intervals as the first step. The average interval over the whole simulation period is 62.6 days. The subsidence data for each PS from the original series was weighted with the ratio of its time interval against the average interval, which created the time series with equal intervals. Taking the 45th PS as an example, the original subsidence data series is as follows:

No.	1	2	3	4	5	6	7	8	9	10
Subsidence (mm)	5.20	5.21	2.89	(1.47)	1.55	2.22	8.93	7.19	(0.85)	2.26
No.	11	12	13	14	15	16	17	18	19	20
Subsidence (mm)	0.00	(1.44)	(1.67)	2.78	1.06	(0.78)	(4.46)	(3.79)	2.29	6.52

Table 7.2: Original subsidence data

After the transformation, the new subsidence data series is as follows:

No.	1	2	3	4	5	6	7	8	9	10
Subsidence (mm)	5.20	5.21	3.14	(0.04)	0.69	2.09	8.22	7.25	(1.03)	2.49
No.	11	12	13	14	15	16	17	18	19	20
Subsidence (mm)	(0.27)	(1.67)	(1.72)	3.51	1.06	(0.70)	(4.41)	(3.82)	2.14	6.52

Table 7.3: New subsidence data

Then the standard grey modelling process was applied to the new series to generate the predictions which were transformed back into the unequal series later. Below are the plots of the simulation results for the 45th PS:

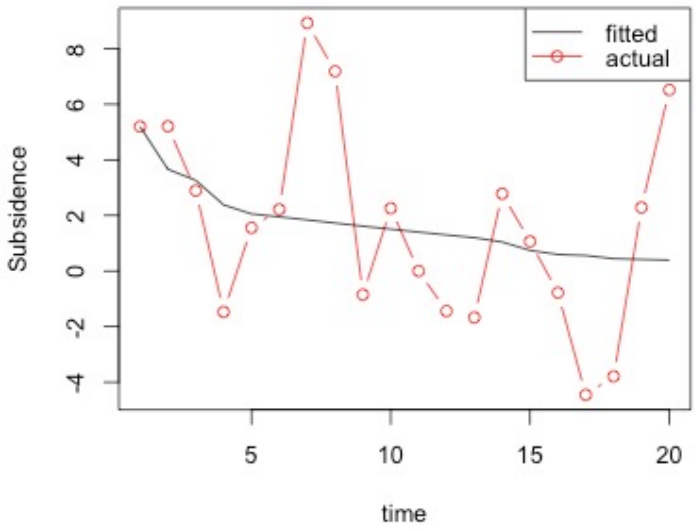

Figure 7.5: Unequal interval actual subsidence vs. unequal interval predicted subsidence

Then the same process was again carried out for all the PSs. The total RMSE was 558.761.

7.5 Simulation Results

A comparison of performance among the three models is listed in Table 7.4.

Model	No. of the Observations	RMSE
ARIMA	9	454.847
Neural Network	9	110.996
Grey Model	9	531.316

Table 7.4: RMSE comparison for equal interval time series

According to the simulation results, the estimated data produced by ARIMA shows a generally similar trend as the actual series. However, due to the regressive nature of ARIMA, the values estimated by ARIMA changed slower than the actual data with time lags between them, which can be clearly seen from the ARIMA plot. In addition, the estimated fluctuation among the data series was also much lower than the actual fluctuation. Therefore, the performance of the ARIMA model was not quite satisfactory. By contrast, the grey model worked better than ARIMA in the aspect of

trend modelling with smaller time lags between the fitted and actual curves. Nevertheless, the grey model is less capable of reflecting the significant changes among the data series, leading to huge prediction errors. Compared to these two models, the ANN model captured both the trend and the fluctuation within the subsidence series through its learning process. As a result, the RMSE of the ANN model is significantly lower than that of the other two models.

However, high performance of models on the training set does not necessary mean that they will achieve the same high performance in future prediction. In order to further check the performance of the three models, the prediction models established previously were used to try to predict the subsidence of the 25th PS at the 14th time point, which was not used in the simulation. The result is shown in Table 7.5.

Actual Subsidence	**ARIMA Predicted**	**Neural Network Predicted**	**Grey Model Predicted**
-4.554	-0.210	-2.928	-6.923

Table 7.5: Subsidence prediction comparison

According to the above results, the ANN model produced the closest prediction result, while the result generated by the grey model is also quite close to the actual value, which shows a huge improvement when compared to its performance on the training set. However, the forecast from the ARIMA model still deviated significantly from the actual subsidence, which to some extent demonstrates that the ARIMA model might not be suitable for subsidence data series modelling and forecasting. Furthermore, as these time series models were established based on the historical data, assuming that the historical trend will continue in the future, if the level of subsidence significantly changed at some point with unexpected changes, the forecast model should always be re-adjusted or re-trained.

In addition, the grey model was also used on a larger set of subsidence series with unequal time intervals. The total RMSE for the test is 558.761 and the RMSE per time point is 27.938. Compared to the RMSE per time point for the grey model built on

equal interval subsidence series which amounts to 59.035, the grey model for the unequal series shows a better simulation performance.

7.6 Summary

In this chapter, ARIMA, ANN and grey models have been used to fit the subsidence series. The first part of the simulation aimed to model the subsidence data with equal time intervals. Among the three models, both the ARIMA model and grey model obtained similar large RMSEs, which means that their performance was not quite satisfactory. Relatively speaking, ARIMA worked better in reflecting fluctuation within the series, while the grey model is able to capture the main trend more accurately with no obvious time lags. The ANN model is the one with the smallest RSME, benefitting from its learning algorithm. This is also justified by the result of an additional prediction test with the data outside the previous data set. However, due to the lack of available data, this simulation can only perform data modelling without the validation step, which limits the quality of the simulation assessment. Additionally, the grey model was also applied to the unequal subsidence series. With the transformation algorithm applied on the series, the simulation result has demonstrated that the grey model is able to generate reliable predictions even on subsidence time series that are not recorded with the same intervals, which sheds light on a broader application of time series for techniques on time series with various characteristics.

Chapter 8 Conclusions and Future Work

8.1 Main Achievements

In order to ensure good performance and to reduce the life cycle cost impact caused by railway subsidence, the author of this thesis has provided an integrated approach to assess railway performance. The main achievements of this research are as follows.

(1) Ability to monitor railway subsidence by using InSAR technique

InSAR is a technique which has been applied in various areas, such as topography mapping, DEM generation, ocean currents mapping and landscape characterization (Lu, et al., 2007). Based on this existing technique, the author of this thesis analysed the feasibility of using InSAR in railway subsidence monitoring and carried out a case study to apply InSAR in the railway subsidence monitoring context.

(2) Ability to predict railway subsidence by using time series prediction models

The author reviewed several prediction models which can be used for time series data and compared the railway subsidence prediction results obtained by using the traditional statistical auto-regressive moving average (ARMA) model, an artificial neural network (ANN) model and the grey model in the case study. The ANN model, which is able to handle the time series data with fewer observations with a non-linear trend, performed best in predicting railway subsidence.

(3) Development of an integrated approach for railway performance assessment

The results of the two case studies conducted in Chapter 6 and 7 provide the foundation for an integrated approach for railway performance assessment. Based on the time series railway deformation data obtained by means of PS-InSAR, a railway subsidence prediction can be carried out based on the three time series prediction models provided in this thesis. This integrated approach ensures better knowledge about the performance of the railway foundation and is able to reduce its life cycle costs, if it is integrated into a robust maintenance strategy.

8.2 Summary of Contents

This thesis is divided into the following three main sections.

(1) Review of railway subsidence monitoring and time series railway subsidence prediction.
(2) Applications of PS-InSAR in railway subsidence monitoring and time series prediction models for railway subsidence.
(3) Case study using PS-InSAR and time series prediction models for performance assessment of HS1.

The first section reviewed three approaches for railway subsidence monitoring and selected InSAR as the most suitable approach to monitor the subsidence of railways in this research. InSAR is a technique which is capable of topography measurement. In order to extract real ground deformation data from the InSAR result, D-InSAR was applied. However, the limitations of D-InSAR reduce the reliability of the ground deformation monitoring result. As an enhanced D-InSAR, PS-InSAR which overcomes the limitations of D-InSAR performance well in ground deformation monitoring, was adopted in this research. This thesis reviewed the development of InSAR and its applications in various research areas. In addition, to prove the feasibility of using PS-InSAR in railway subsidence monitoring, three successful examples were described. For railway subsidence prediction, three time series prediction models were introduced, which were traditional statistical models, an artificial neural network model and a grey model which is able to handle a system with partially known parameters.

The second section consists of the methods of using PS-InSAR in railway subsidence monitoring and time series prediction models for railway subsidence prediction. After presenting the principle for topography measurement by InSAR and ground deformation monitoring by PS-InSAR, detailed procedures for extracting deformation results for the railway were illustrated. Based on the historical deformation records of railway obtained by PS-InSAR, time series subsidence prediction was applied. The methods of the predicting time series subsidence of railway by statistics prediction model ARIMA, a neural network model based on artificial intelligence and a grey model were described.

For assessment of railway performance, two case studies were described in the third section, which were a case study of subsidence monitoring of HS1 and a case study of subsidence prediction of HS1. A 53 km railway which is located on the route of HS1 was selected for the study. Based on subsidence monitoring results of HS1 obtained by PS-InSAR, a time series analysis of selected PS along HS1 was carried out and a deformation profile of HS1 was generated. The subsidence results of HS1 provide the input data for time series prediction models. In the case study of railway subsidence prediction, two simulations for time series with equal interval and unequal interval were conducted. ARIMA, the neural network model and grey model were applied in the first simulation respectively while only the grey model, which is capable of dealing with unequal interval time series, was used in the second simulation.

8.3 Conclusions

The main findings of this thesis are concluded as follows.

8.3.1 Railway Subsidence Monitoring

Rapid development of the railway has brought about better railway capability, which has further led to heavier axle loads and higher speed lines. As a result, unstable railway subgrade has become a threat to good railway performance. In order to ensure good performance, safe operation and to reduce the life cycle costs of the railway, railway subsidence monitoring was carried out in this research. The major findings of the subsidence monitoring are illustrated below.

(1) Railway subsidence monitoring not only requires precise monitoring result but it also requires large monitoring coverage and a long monitoring period. As a result, the InSAR technique is able to monitor the subsidence of the railway.

(2) Based on the principle of InSAR, a ground deformation result can be extracted from the radar interferogram generated from a pair of radar images. If ground deformation occurred during the acquisition of the image pair, topography information should be removed from the ground deformation result by using D-InSAR, then the real ground deformation result can be obtained. In order to overcome the limitations of D-InSAR and obtain a reliable ground deformation result, PS-InSAR was applied to monitor railway subsidence in this research.

(3) The feasibility of applying PS-InSAR for railway subsidence monitoring in this research was proved by the applications of railway subsidence monitoring by SNCF High Speed Rail Network, Jubilee Extension Line in London and Jinshan Railway in China.

8.3.2 Railway Subsidence Prediction

Historical deformation records for the railway obtained by PS-InSAR are considered as a discrete time series. In order to predict trends of the deformation time series and provide maintenance guidance for the railway, time series prediction models were applied. Major findings of railway subsidence prediction are concluded as follows.

(1) A discrete time series is composed by historical railway deformation records. Three main time series prediction models which are traditional statistical model ARMA, ANN model based on artificial intelligence and a grey model were adopted for railway subsidence prediction in this thesis.

(2) All of the three time series prediction models are able to predict the subsidence of the railway and each of them has its own specialist area of expertises. ARMA is suitable for time series with a large data volume and a stable developing trend, whereas the ANN model is capable of the prediction for the time series with fewer observations and an un-linear developing trend. For time series systems with partially unknown parameters and limited observations, the grey model performs well.

8.3.3 Case Study of Railway Performance Assessment

In order to assess railway performance, two case studies, which are subsidence monitoring and subsidence prediction of HS1, were carried out. A deformation profile of HS1 was created based on the deformation monitoring result of HS1 obtained from the subsidence monitoring case study while the time series prediction model which is the most suitable one for prediction of railway subsidence was determined after carrying out the railway subsidence prediction case study. The major findings and conclusions are indicated as follows.

(1) The deformation profile of HS1 indicates that no significant subsidence has occurred on HS1 and HS1 is stable after being in operation for 10 years.

(2) Although HS1 is generally stable, potential subsidence was detected on some sections of HS1 compared with the other railway sections. For example, a vertical subsidence velocity of up to 4.0 mm per year was detected in the North Downs Tunnel. In addition, the railway section between Hockers Lane Overbridge and Water Lane Underbridge had a vertical subsidence velocity of up to 2.9 mm per year. More frequent subsidence monitoring work should be carried out on the sections of HS1 with potential subsidence.

(3) As one of the important railway stations of HS1, ground stability of Ashford International Station is an important criterion for the safe operation of HS1. The subsidence monitoring result of this case study proved the stability of Ashford International Station.

(4) The results of railway subsidence prediction indicated that the ARIMA model and the grey model did not have a satisfactory performance in subsidence prediction of HS1 as both of them obtained similar larger RMSEs. ARIMA was good in reflecting fluctuation within the series while the grey model worked well in capturing the main trend more accurately with no obvious time lags. Compared with the ARIMA model and the grey model, ANN model performed best and obtained the lowest RMSEs. The case study also demonstrated that a reliable prediction result could be generated by the grey model even on subsidence time series that are not recorded at the same interval.

8.4 Future Work

8.4.1 SBAS-InSAR in Railway Subsidence Monitoring

PS-InSAR was adopted in the case study of railway subsidence monitoring. In PS-InSAR data processing, one master image is selected based on the minimization of the temporal baseline and spatial baseline and the mean Doppler centroid frequency difference, while the rest of the images are the slave images. In order to reduce spatial decorrelation of the interferograms, only the image pair with a perpendicular baseline smaller than 800 m should be selected for PS-InSAR processing.

Interferograms with better spatial correlation can be created by applying a shorter critical perpendicular baseline in the selection of the image pairs. In addition,

temporal baselines of some image pairs are long because only one SLC image is selected as the master image in PS-InSAR. As a result, to ensure temporal correlation of the interferogram, less image pairs are identified for interferogram generation. Not only spatial correlation, but also temporal correlation of the interferogram is essential for a robust railway subsidence result. As a result, a shorter perpendicular baseline and temporal baseline are key parameters in railway subsidence monitoring by InSAR.

SBAS-InSAR (Small Baseline Subset InSAR), which is able to select more interferometric image pairs with shorter perpendicular baseline from less SLC images, has been applied for ground deformation monitoring by Berardino et al. in 2002 (Berardino, et al., 2002).

Different from PS-InSAR, any SLC images can be considered as the master image of the image pair if the temporal baseline and perpendicular baseline of the image pair are below a certain hurdle. An image pair with a perpendicular baseline smaller than 400m can be selected for interferogram generation (Li, et al., 2009). As a result, more interferograms with good spatial and temporal correlation are generated for time series subsidence analysis by less SLC images.

Based on the deformation result of HS1 obtained by PS-InSAR, a deformation profile of HS1 was created and the stability of HS1 was demonstrated. For future research, in order to have a more reliable subsidence monitoring result of HS1, a deformation profile of HS1 generated by SBAS-InSAR can be compared with the one obtained by PS-InSAR or historical levelling survey data.

8.4.2 Railway Safety Assessment

In order to ensure good railway performance, not only railway subsidence monitoring and prediction but also a safety assessment of railway infrastructure should be considered in an intergraded railway performance assessment approach in future work. Recently, the stability of railway and highway infrastructure in the UK has been threatened by the wet weather. For instance, a 15 ft-deep sinkhole was found on the M2 motorway near Sittingbourne in Britain due to wet weather. In addition, water extraction resulted in ground subsidence of the London Jubilee Tube Extension Line.

A railway safety assessment should consider all the factors which might threaten the stability of railway infrastructures. The safety factors can be categorised into physical factors, environmental factors and maintenance factors. Physical factors, such as train speed, axle load, subgrade stiffness, track corrugation, welds, joints and defects, and initial construction, are the main contributors to bearing and bending stresses concentrated on the railway. Environmental factors include rain fall, drainage, subgrade soil and over steepened slopes, while railway maintenance work is considered as the maintenance factor.

After identifying the safety factors which are related to railway subsidence, a safety assessment is required to assess the risk level of these factors. The risk level of these safety factors can be assessed through a fuzzy logic model (An, et al., 2013) and neural network (Guler, 2013). Generally, the risk level of a safety factor depends on its frequency of occurrence and consequence severity. However, the frequency and severity of some safety factors are uncertain. In order to overcome the uncertainty, a fuzzy logic model is applied in railway safety assessment through indicating risk level and risk degree of each safety factor. Accordingly, the corresponding weight of each safety factor in the overall degree of risk of railway subsidence is evaluated. Based on the weight and risk degree of each safety factor, the overall degree of risk of railway subsidence can be calculated. In addition, a neural network model based on artificial intelligence has also been demonstrated to be capable of determining the weight of safety factors through various learning algorithms.

Reference

Japan Aerospace Exploration Agence, 2004. *JERS-1*. [Online]
Available at: http://www.eorc.jaxa.jp/JERS-1/en/
[Accessed 18 June 2014].

Adam, N., Kampes, B. & Eineder, M., 2003. The development of a scientific permanent scatterer system. *ISPRS Journal*.

Agustan, 2010. *Ground deformation detection based on ALOS-PALSAR data utilizing DInSAR technique in Indonesia*, Nagoya: Graduate School of Environmental Studies, Nagoya University.

Alstom, 2010. *Channel Tunnel Rail Link Project.* [Online]
Available at:
http://www.alstom.com/Global/Transport/Resources/Documents/Factsheets/References%20-%20Infrastructure%20-%20Union%20Railway%20North%20HS1%20-%20English.pdf
[Accessed 15 July 2014].

Altamira Information, n.d. *Case Study: Monitoring of High Speed Line (SNCF).* [Online]
Available at: http://www.altamira-information.com/html/1-18637-CASE-STUDY-Monitoring-of-high-speed-line-SNCF.php
[Accessed 26 February 2014].

An, M., Lin, W. & Huang, S., 2013. An Intelligent Railway Safety Risk Assessment Support Sytem for Railway Operation and Maintenance Analysis. *The Open Transportation Journal*, 7(1), pp. 27-42.

ASAR Instrument Functionality, 2014. *ESA Earthnet Online.* [Online]
Available at: https://earth.esa.int/handbooks/asar/CNTR3-1-2.htm
[Accessed 19 June 2014].

Aslanargun, A., Mammadov, M., Yazici, B. & Yolacan, S., 2007. Comparison of ARIMA, neural networks and hybrid models in time series: tourist arrival forecasting. *Journal of Statistical Computation and Simulation,* 77(1), pp. 29-53.

Azoff, E., 1994. *Neural Network Time Series Forecasting of Financial Markets.* New York: John Wiley \& Sons, Inc..

Baek, J. et al., 2008. Analysis of ground subsidence in coal mining area using SAR interferometry. *Geosciences,* 12(3), pp. 277-284.

Baek, S. & Shum, C., 2011. *Antarctic ocean tide signal restoration using differential InSAR technique.* Seuol, s.n., pp. 1-4.

Balzter, H., 2001. Forest mapping and monitoring with interferometric synthetic aperture radar (InSAR). *Progress in Physical Geography,* 25(2), pp. 159-177.

Bamler, R. et al., 2003. *SRTM and Beyond: Current Situation and New Developments in Spaceborne InSAR.* Hannover, s.n.

Bamler, R. & Hartl, P., 1998. Synthetic aperture radar interferometry. *Inverse Problems,* 14(4), pp. R1-R54.

Baran, I., 2009. *Airborne InSAR and LiDAR.* [Online]
Available at:
http://www.researchgate.net/publication/265686555_Airborne_InSAR_and_LiDAR_Compared_by_I_Baran_2009
[Accessed 22 July 2015].

Bell, J., Amelung, F., Ramelli, A. & Blewitt, G., 2002. 1935–2000: New geodetic data show evolution, revised spatial patterns, and reduced rates. *Environmental & Engineering Geoscience,* 8(3), pp. 155-174.

Berardino, P., Fornaro, G., Lanari, R. & Sansosti, E., 2002. A new Algorithm for Surface Deformation Monitoring based on Small Baseline Differential SAR Interferograms. *IEEE Transactions on Geoscience and Remote Sensing,* 40(11), pp. 2375-2383.

Box , G. & Jenkins, G., 1970. *Time series analysis, forecasting and control.* San Francisco, CA: Holden Day.

Box, G. & Jenkins, G., 1976. *Time series analysis: Forecasting and control.* San Fransisco, CA: Holden Day.

Brockwell, P. & Davis, R., 2002. *Introduction to time series and forecasting.* s.l.:s.n.

Bürgmann, R., Rosen, P. & Fielding, E., 2000. Sythetic Aperture Radar Interferometry to Measure Earth's Surface Topography and its Deformation. *Annual Review of Earth and Planetary Sciences,* May, Volume 28, pp. 169-209.

Chang, B. R. & Tsai, H. F., 2008. Forecast approach using neural network adaptation to support vector regression grey model and generalized auto-regressive conditional heteroscedasticity. *Expert Systems with Application,* Volume 34, pp. 925-934.

Chen, C. & Zebker, H., 2001. Two-dimensional phase unwrapping with use of statistical models for cost functions in nonlinear optimization. *JOSA,* A 18(2), pp. 228-251.

Chen, L. & Lai, X., 2011. *Comparison between ARIMA and ANN Models Used in Short-Term Wind Speed Forecasting.* Wuhan, s.n., pp. 1-4.

Chen, Y., Zhang, G., Ding, X. & Li, Z., 2000. Monitoring Earth Surface Deformations with InSAR Technology: Principle and Some critical Issues. *Journal of Geospatial Engineering,* 2(1), pp. 3-21.

Chin, K. & Arthur, R., 1996. Neural network vs. conventional methods of forecasting. *Journal of Business Forecasting,* 14(4), pp. 17-22.

Coelho, B. et al., 2011. An assessment of transition zone performance. *Proceedings of the Institution of Mechanical Engineers Part F: Journal of Rail and Rapid Transit,* 225(2), pp. 129-139.

Cumming, I. et al., 1997. *Glacier flow measurements with ERS tandem mission data.* Zurich, s.n., pp. 353-362.

Cutrona, L., Leith, E., Porcello, L. & Vivian, W., 1966. On the Application of Coherent Optical Processing Techniques to Synthetic-Aperture Radar. *Proceedings of the IEEE,* August, 54(8), pp. 1026-1032.

Delft University of Technology, 2014. *ERS and Envisat Precise Orbit Determination.* [Online]

Available at: http://www.deos.tudelft.nl/ers/precorbs/
[Accessed 15 Feb 2014].

Dellepiane, S., De Laurentiis, R. & Giordano, F., 2004. Coastline extraction from SAR images and a method for the evaluation of the coastline precision. *Pattern Recognition Letters,* 25(13), pp. 1461-1470.

Deng, J., 1982. Control problems of grey systems. *Systems & Control Letters,* 1(5), pp. 288-294.

Deng, J., 1989. Introduction to grey system theory. *The Journal of grey system,* Volume 1, pp. 1-24.

Ding, X. et al., 2008. Atmospheric Effects on InSAR Measurements and Their Mitigation. *Sensors,* Volume 8, pp. 5426-5448.

Duke University, n.d. *Identifying the numbers of AR or MA terms in an ARIMA model.* [Online]
Available at: http://people.duke.edu/~rnau/411arim3.htm
[Accessed 28 January 2015].

Duke University, n.d. *Identifying the order of differencing in an ARIMA model.* [Online]
Available at: http://people.duke.edu/~rnau/411arim2.htm
[Accessed 28 January 2015].

Eineder, M. & Adam, N., 2005. A maximum-likelihood estimator to simultaneously unwrap, geocode, and fuse SAR interferograms from different viewing geometries into one digital elevation model. *IEEE Transactions on Geoscience and Remote Sensing,* 43(1), pp. 24-36.

ESA, 2014. *What is ERS?.* [Online]
Available at: https://earth.esa.int/web/guest/missions/esa-operational-eo-missions/ers
[Accessed 18 June 2014].

European Space Agence, 2015. *Radar and SAR glossary.* [Online]
Available at: https://earth.esa.int/handbooks/asar/CNTR5-2.htm
[Accessed 16 January 2015].

Ferretti, A. et al., 2007. *InSAR Principles - Guidelines for SAR Interferometry Processing and Interpretation.* Noordwijk: ESA Publications.

Ferretti, A., Monti-Guarnieri, A., Prati, C. & Rocca, F., 2007. Part B InSAR processing: a practical approach. In: *InSAR Principles:Guidelines for SAR Interferometry Processing and Interpretation.* Frascati: ESA Publications, pp. B3-B67.

Ferretti, A., Prati, C. & Rocca, F., 2000. Nonlinear Subsidence Rate Estimation Using Permanent Scatterers in Differential SAR Interferometry. *IEEE Transactions on Geoscience and Remote Sensing,* 38(5), pp. 2202-2212.

Ferretti, A., Prati, C. & Rocca, F., 2001. Permanent scatterers in SAR interferometry. *IEEE Transactions onGeoscience and Remote Sensing,* 39(1), pp. 8-20.

Ferretti, A. & Rocca, F., 2000. Permanent Scatterers in SAR Interferometry. *IEEE Transactions on Geoscience and Remote Sensing,* 39(1), pp. 8-20.

Fornaro, G., 1999. Trajectory deviations in airborne SAR: analysis and compensation. *IEEE Transactions on Aerospace and Electronic Systems,* 35(3), pp. 997-1009.

Franceschetti, G. & Lanari, R., 1999. *Synthetic Aperture Radar Processing.* New York: CRC Press.

Gabriel, A., Goldstein, R. & Zebker, H., 1989. Mapping small elevation changes over large areas: Differential Radar Interferometry. *Geophysical Research,* 94(B7), pp. 9183-9191.

Ge, D., Wang, Y., Guo, X. & Wang, Y., 2008. *Land Subsidence Investigation Along Railway Using Permanent Scatterers SAR Interferometry.* Boston, s.n.

Ge, D. et al., 2009. *Using Permanent Scatterer InSAR to monitor land subsidence along high speed rail- the first experiment in China.* Frascati, Italy, s.n.

GEOIMAGE, 2012. *TerraSAR-X.* [Online]
Available at: http://www.geoimage.com.au/satellite/TerraSar
[Accessed 19 June 2014].

Gershenson, C., 2003. Artificial Neural Networks for Beginners. *arXiv preprint cs/0308031.*

Ghaffari, A., Abdollahi, H., Khoshayand, M. & Bozchalooi, I. S., 2006. Performance comparison of neural network training algorithms in modeling of bimodal drug delivery. *International Journal of Pharmaceutics,* Volume 327, pp. 126-138.

Goldstein, R. & Werner, C., 1998. Radar Interferogram Filtering for Geophysical Applications. *Geophysical Research Letter,* Volume 25, pp. 4035-4038.

Goldstein, R. & Zebker, H., 1987. Interferometric radar measurements of ocean surface. *Nature,* Volume 328, pp. 707-709.

Goldstein, R., Zebker, H. & Werner, C., 1988. Satellite radar interferometry: Two dimensional phase unwrapping. *Radio Science,* 23(4), pp. 713-720.

Gondwe, B., Hong, S., Wdowinski, S. & Bauer-Gottwein, P., 2010. Hydrologic Dynamics of the Ground-Water-Dependent Sian Ka'an Wetlands, Mexico, Derived from InSAR and SAR Data. *Wetlands,* 30(1), pp. 1-13.

Graham, L., 1974. Synthetic Interferometer Radar for topographic mapping. *Proceedings of the IEEE,* 62(6), pp. 763-768.

GRAS, D., 2014. *Envisat.* [Online]
Available at: http://www.dhi-gras.com/-/media/microsite_gras/files/envisat_asar_brochure.pdf
[Accessed 9 December 2014].

Guler, H., 2013. Prediction of railway track geometry deterioration using artificial neural networks: a case study for Turkish state railways. *Structure and Infrastructure Engineering,* pp. 1-13.

Hagberg, J., Ulander, L. & Askne, J., 1995. Repeat-pass SAR interferometry over forested terrain. *IEEE Transactions on Geoscience and Remote Sensing,* 33(2), pp. 331-340.

Hanssen, R., 2001. Chapter 6. In: *Radar Interferometry: Data Interpretation and Error Analysis.* s.l.:Kluwer, pp. 197-246.

Hanssen, R. & Bamler, R., 1999. Evaluation of interpolation kernels for SAR interferometry. *IEEE Transactions on Geoscience and Remote Sensing,* 37(1), pp. 318-321.

Haykin, S., 1994. *Neural networks: a comprehensive foundation.* Michigan: Macmillan.

Herrera, G. et al., 2009. Advanced interpretation of subsidence in Murcia (SE Spain) using A-DInSAR data-modelling and validation. *Natural Hazards and Earth System Sciences,* Volume 9, pp. 647-661.

High Speed Two (HS2) Limited, 2013. *Impacts of Tunnels in the UK,* London: High Speed Two (HS2) Limited.

Hill, E. & Blewitt, G., 2006. Testing for fault activity at Yucca Mountain, Nevada, using independent GPS results from the BARGEN network. *Geophysical Research Letters,* 33(14).

Hilley, G. E. et al., 2004. Dynamics of Slow-Moving Landslides from Permanent Scatterer Analysis. *Science,* Volume 304, pp. 1952-1955.

Hirsch, O., 2001. *Calibration of an Airborne Along-Track Interferometric SAR System for Accurate Measurement of Velocityes.* Sydney, s.n., pp. 558-560.

Hooper , A., Bekaert, D. & Spaans, K., 2013. *StaMPS/MTI Manual Version 3.3b1,* Leeds: University of Leeds.

Hooper, A., 2006. *Persistent Scatterer Radar Interferometry for Crustal Deformation studies and Modelling of Volcanic Deformation,* Stanford: s.n.

Hooper, A., Bekaert, D., Spaans, K. & Arikan, M., 2012. Recent Advances in SAR Interferometry Time Series Analysis for Measuring Crustal Deformation. *Tectonophysics,* Volume 514, pp. 1-13.

Hooper, A. & Zebker, H., 2007. Phase unwrapping in three dimensions with application to InSAR time series. *JOSA A,* 24(9), pp. 2737-2747.

Hooper, A., Zebker, H., Segall, P. & Kampes, B., 2004. A new method for measuring deformation on volcanoes and other natural terrains using InSAR persistent scatterers. *Geophysical Research Letters,* December.31(23).

HS1, 2013. *High Speed One.* [Online]
Available at: http://www.highspeed1.com/
[Accessed 15 July 2014].

Huang, Y. & Huang, C., 1996. The integration and application of fuzzy and grey modeling methods. *Fuzzy Sets and Systems,* 2, 78(1), pp. 107-119.

Hurley, J., 2010. *Operational Review: RADARSAT - 1&2.* Roma, s.n.

Hwang, C., Hung, W. & Liu, C., 2008. Results of Geodetic and Geotechnical Monitoring of Subsidence for Taiwan High Speed Rail Operation. *Natural Hazards,* 47(1), pp. 1-16.

ISA, 2007. *COSMO-SkyMed System Description & User Guide,* Roma: Italian Space Agency (ISA).

Jensen, J., 2007. *Remote Sensing of the Environment: An Earth Resource Perspective.* Second Edition ed. s.l.:Pearson Education.

Jet Propulsion Laboratory, 2005. *What Part of the Earth was Mapped?.* [Online] Available at: http://www2.jpl.nasa.gov/srtm/coverage.html
[Accessed 24 February 2014].

Jones, R., 1966. Exponential Smoothing for Multivariate Time Series. *Journal of the Royal Statistical Society. Series B (Methodological),* 28(1), pp. 241-251.

Joughin, I., Abdalati, W. & Fahnestock, M., 2004. Large fluctuations in speed on Greenland's Jakobshavn Isbræ glacier. *Nature,* Volume 432, pp. 608-610.

Kampes, B. & Hanssen, R., 2004. Ambiquity resolution for permanent scatterer interferometry. *IEEE Transactions on Geoscience and Remote Sensing,* 42(11), pp. 2446-2453.

Kayacan, E., Ulutas, B. & Kaynak, O., 2010. Grey system theory-based models in time series prediction. *Expert Systems with Applications,* 37(2), pp. 1784-1789.

Kenyi, L. & Kaufmann, V., 2003. Estimation of rock glacier surface deformation using SAR interferometry data. *IEEE Transactions on Geoscience and Remote Sensing,* 41(6), pp. 1512-1515.

Klees, R. & Massonnet, D., 1998. Deformation measurements using SAR interferometry: potential and limitations. *Geologie en Mijnbouw,* 77(2), pp. 161-176.

Kohzadi, N., Boyd, M., Kermanshahi, B. & Kaastra, I., 1996. A comparison of artificial neural network and time series model for forecasting commodity prices. *Neurocomputing,* 10(2), pp. 169-181.

Kwok, R. & Fahnestock, M., 1996. Ice sheet motion and topography from radar interferometry. *IEEE Transactions on Geoscience and remoote Sensing,* 34(1), pp. 189-200.

Lee, J., Miller, A. & Hopper, K., 1994. Statistics of Phase Difference and Product Magnitude of Multi-look processed Gaussian Signals. *Waves in Random Media,* 4(3), pp. 307-320.

Liang, S., Li, X. & Wang, J., 2012. *Advanced Remote Sensing.* Oxford: Academic Press.

Liao, M., Wang, T., Lu, L. & Zhou, W., 2007. Reconstruction of DEMs From ERS-1/2 Tandem Data in Mountainous Area Facilitated by SRTM Data. *IEEE Transactions on Geoscience and Remote Sensing,*, 45(7), pp. 2325-2335.

Liew, S., 2001. *Microwave Remote Sensing.* [Online]
Available at: http://www.crisp.nus.edu.sg/~research/tutorial/mw.htm
[Accessed 2014 March 4].

Lin, A., Ren, Z., Jia, D. & Wu, X., 2009. Co-seismic thrusting rupture and slip distribution produced by the 2008 Mw 7.9 Wenchuan earthquake, China. *Tectonophysics,* 471(3-4), pp. 203-215.

Li, Z. & Bethel, J., 2008. Image Coregistration in SAR Interferometry. *The International Archives of the Photogrammetry, Remote Sensing and Spatial Information Sciences,* XXXVII(Part B1), pp. 433-438.

Li, Z., Fielding, E., Cross, P. & Preusker, R., 2009. Advanced InSAR atmospheric correction: MERIS/MODIS combination and stacked water vapour models. *International Journal of Remote Sensing,* 30(13), pp. 3343-3363.

Li, Z. et al., 2009. Using small baseline interferometric SAR to map nonlinear ground motion: a case study in Northern Tibet. *Journal of Applied Geodesy 3,* pp. 163-170.

Li, Z. et al., 2004. A quantitative measure for the quality of InSAR interferogram based on phase differences. *Photogrammetric engineering and remote sensing,* 70(10), pp. 1131-1138.

Lubis, A. et al., 2011. Ground subsidence in Semarang-Indonesia investigated by ALOS–PALSAR satellite SAR interferometry. *Asian Earth Sciences,* 40(5), pp. 1079-1088.

Lu, Z., Kwoun, O. & Rykhus, R., 2007. Interferometric Synthetic Aperture Radar (InSAR): Its Past, Present and Future. *Photogrammetric Engineering & Remote Sensing,* pp. 217-221.

Lu, Z., Wicks, C., Power, J. & Dzurisin, D., 2002. *Interferometric synthetic aperture radar studies of Alaska volcanoes.* s.l., s.n.

Makridakis, S. & Hibon, M., 1997. ARMA Models and the Box Jenkins Methodology. *Journal of Forecasting,* 5, 16(3), pp. 147-163.

Massonnet, D. & Felgl, K., 1998. Radar Interferometry and its Application to Changes in the Earth's Surface. *Reviews of Geophysics ,* 36(4), pp. 441-500.

Massonnet, D. et al., 1993. The Displacement Field of The Landers Earthquake Mapped By Radar Interferometry. *Nature,* Volume 364, pp. 138-142.

Matias, G., 2006. *Radar Interferometry: 2D Phase Unwarpping via graph cuts,* s.l.: Lisbon Technical University.

Matias, G., 2006. *Radar Interferometry: 2D Phase Warpping via graph cuts,* s.l.: Lisbon Technical University.

McCandless, S. & Jackson, C., 2004. Chapter 1. Principles of Synthetic Aperture Radar. In: *Synthetic Aperture Radar Marine User's Manual.* Washington, DC: U.S Department of Commerce, pp. 1-23.

McCulloch, W. & Pitts, W., 1943. A logical calculus of the ideas immanent in nervous activity. *The bulletin of mathematical biophysics,* 5(4), pp. 115-133.

Mentzer, J. & Moon, M., 2005. *Sales forecasting management: a demand management approach.* s.l.:s.n.

Mikhail, B., 2009. *Radar Imaging of the Ocean Wave.* First ed. Amsterdam: Elsevier.

Moreira, A., 1991. Improved Multilook Techniques Applied to SAR and SCANSAR Imagery. *IEEE Transactions on Geoscience and Remote Sensing,* July, 29(4), pp. 529-534.

NASA, 2014. *Seasat 1.* [Online]
Available at: http://science.nasa.gov/missions/seasat-1/
[Accessed 18 June 2014].

NERC, 2008. *British Geological Survey: The Chalk Aquifer of the North Downs,* Nottingham: Natural Environment Research Council (NERC).

Network Rail (High Speed) Ltd, 2013. *Network Rail (High Speed) Outside Parties Development Handbook,* London: s.n.

Ortiz, A., 2007. *Scansar-to-stipmap Interferometric Observation of Hawaii,* Stanford: Stanford University.

Osmanoğlu, B. et al., 2011. Mexico City subsidence observed with persistent scatterer InSAR. *International Journal of Applied Earth Observation and Geoinformation,* 13(1), pp. 1-12.

Perski, Z., Hanssen, R., Wojcik, A. & Wojciechowski, T., 2009. InSAR analyses of terrain deformation near the Wieliczka Salt Mine, Poland. *Engineering Geology,* May, 106(1-2), pp. 58-67.

Plaut, J., 1996. *Summary of science results from spaceborne imaging radar (SIR-C/X-SAR).* s.l., s.n.

Pritchard, M. et al., 2002. Co-seismic slip from the 1995 July 30 Mw= 8.1 Antofagasta, Chile, earthquake as constrained by InSAR and GPS observations. *Geophysical Journal International,* 150(2), pp. 362-376.

Prybutok, V., Yi, J. & Mitchell, D., 2000. Comparison of neural network models with ARIMA and regression models for prediction of Houston's daily maximum ozone concentrations. *European Journal of Operational Research,* 122(1), pp. 31-40.

Quah, T. & Srinivasan, B., 1999. Improving returns on stock investment through neural network selection. *Expert Systems with Applications,* 17(4), pp. 295-301.

Rabiner, L., 1989. A tutorial on hidden Markov models and selected applications in speech recognition. *Proceedings of the IEEE,* 77(2), pp. 257-286.

Rogers, A. & Ingalls, R., 1969. Venus: Mapping the surface reflectivity by radar interferometry. *Science,* 165(797-799), pp. 797-799.

Romeiser, R., Suchandt, S. & Sprenger, J., 2007. Current Measurements in Rivers by Spaceborne Along-Track InSAR. *IEEE Transactions on Geoscience and Remote Sensing,* 45(12), pp. 4019-4031.

Rosenqvist, A., Shimada, M. & Watanabe, M., 2004. *ALOS PALSAR: Technical Outline and Mission Concepts.* Innsbruck, Austria, s.n.

Rumelhart, D. & McClelland, J., 1986. *Parallel Distributed Processing.* Cambridge: MIT Press.

Samiei-Esfahany, S., 2008. *Improving Persistent Scatterer Interferometry Results for Deformation Monitoring,* Delft: Delft University of Technology.

Schwabisch, M., 1998. *A fast and efficient technique for SAR interferogram geocoding.* Seattle, IEEE, pp. 1100-1102.

Shiskin, J., 1958. Decomposition of Economic Time Series. *Science,* 128(3338), pp. 1539-1546.

Siegmund, R., Bao, M., Lehner, S. & Mayerle, R., 2004. First Demonstration of Surface Currents Imaged by Hybrid Along- and Cross-Track Interferometric SAR. *IEEE Transactions and Geoscience and Remote Sensing,* 42(3), pp. 511-519.

Simons, M., Fialko, Y. & Rivera, L., 2002. Coseismic Deformation from the 1999 Mw 7.1 Hector Mine, California, Earthquake as Inferred from InSAR and GPS Observations. *Bulletin of the Seismological Society of America,* 92(4), pp. 1390-1402.

Slacikova, J. & Potuckova, M., 2011. *Evaluation of Interpolation Methods in InSAR DEM Derivation from ERS Tandem Data.* Prague, s.n., pp. 544-551.

Stepnicka, M. et al., 2009. *Time Series Analysis and Prediction Based on Fuzzy Rules and the Fuzzy Transform.* Lisboa, s.n.

Strozzi, T. et al., 2001. Land Subsidence Monitoring with Differential SAR Interferometry. *Photogrammetric Engineering & Remote Sensing,* 67(11), pp. 1261-1270.

Suksmono, A. & Hirose, A., 2002. Adaptive noise reduction of InSAR images based on a complex-valued MRF model and its application t o phase unwrapping problem. *IEEE Transactions on Geoscience and Remote Sensing,* 40(3), pp. 699-709.

Suwansawat, S. & Einstein, H., 2006. Artificial neural networks for predicting the maximum surface settlement caused by EPB shield tunneling. *Tunnelling and Underground Space Technology,* 21(2), pp. 133-150.

Tang, Y. et al., 2007. Application of grey theory-based model to prediction of land subsidence due to engineering environment in Shanghai. *Environmental Geology,* 55(3), pp. 583-593.

The Committees of Public Accounts, 2012. *The Completion and Sale of High Speed 1- Fourth Report of Session 2012–13,* London: The Stationery Office Limited.

Thissen, U. et al., 2003. Using support vector machines for time series prediction. *Chemometrics and Intelligent Laboratory Systems,* 69(1-2), pp. 35-49.

Tizzani, P. et al., 2007. Surface deformation of Long Valley caldera and Mono Basin, California, investigated with the SBAS-InSAR approach. *Remote Sensing of Environment,* 108(3), pp. 277-289.

Tomás, R. et al., 2005. Mapping ground subsidence induced by aquifer overexploitation using advanced Differential SAR Interferometry: Vega Media of the Segura River (SE Spain) case study. *Remote Sensing of Environment,* October, 98(2-3), pp. 269-283.

TRE, 2011. *SqueeSAR™ measures ground displacement associated with tunneling activities.* [Online]
Available at: http://treuropa.com/transportation/tunnels/
[Accessed 27 February 2014].

Trevett, J., 1986. *Imaging Radar for Resource Surveys.* London: Chapman&Hall.

Ulady, F., Moore, R. & Fung, A., 1986. *Microwave remote sensing active and passive: Volume 2.* Norwood(MA): Artech House Inc.

Usai, 2001. *A new approach for long term monitoring of deformations by differential SAR interferometry,* Delft: s.n.

Van Zyl, J., 2001. The Shuttle Radar Topography Mission (SRTM): a Breakthrough in Remote Sensing of Topography. *Acta Astronautica,* 48(5-12), pp. 559-565.

Vehicle /Track System Interface Committee, 2010. *Best Practice in Wheel-rail Interface Management for Mixed Traffic Railways.* London: University of Birmingham Press.

Wegmuller, U., Walter, D., Spreckels, V. & Werner, C., 2010. Nonuniform Ground Motion Monitoring With TerraSAR-X Persistent Scatterer Interferometry. *IEEE Transactions on Geoscience and Remote Sensing,* 48(2), pp. 895-904.

Wen, K. & Huang, Y., 2004. *The development of grey Verhulst toolbox and the analysis of population saturation state in taiwan–fukien.* The Netherlands, s.n., pp. 5007-5012.

Wold, H., 1938. *A study in the analysis of stationary time series.* Stockholm: Almqvist & Wiksell.

Woodhouse, I., 2006. *Introduction to Microwave Remote Sensing.* Boca Raton(FL): CRC Press.

Xia, Y., 2010. Chapter 11 Synthetic Aperture Radar Interferometry. In: G. Xu, ed. *Sciences of Geodesy - I.* Berlin: Springer Berlin Heidelberg, pp. 415-474.

Yang, W., Peng, L. & Wang, L., 2009. *Method of Ground Settlement Prediction in Urban Tunnel Construction Based on ARMA.* Changsha, s.n., pp. 270-275.

Yan, Y. et al., 2012. Mexico City subsidence measured by InSAR time series: joint analysis using PS and SBAS approaches. *IEEE Journal of Selected Topics in Applied Earth Observations and Remote Sensing,,* 5(4), pp. 1312-1326.

Yun, S., Segall, P. & Zebker, H., 2006. Constraints on magma chamber geometry at Sierra Negra Volcano, Galápagos Islands, based on InSAR observations. *Journal of Volcanology and Geothermal Research,* 150(1-3), pp. 232-243.

Zarembski, A., Grissom, G. & Euston, T., 2013. *Use of Ballast Inspection Technology for the Prioritization, Planning and Management of Ballast Delivery and Placement.* Indianapolis, s.n.

Zebker, H. & Goldstein, R., 1986. Topographic mapping from interferometric synthetic aperture radar observations. *Journal of Geophysical Research,* 91(B5), pp. 4993-4999.

Zebker, H., Werner, C., Rosen, P. & Hensley, S., 1994. Accuracy of Topographic Maps Derived From ERS-1 Interferometric Radar. *IEEE Transactions on Geoscience and Remote Sensing,* 32(4), pp. 823-836.

Zetica, 2015. *Zetica Ltd All Services Brochure.* [Online]
Available at:
http://www.zetica.com/downloads/Zetica%20Ltd_All%20services%20brochure.pdf
[Accessed 20 July 2015].

Zhang, G., 2003. Time series forecasting using a hybrid ARIMA and neural network model. *Neurocomputing,* Volume 50, pp. 159-175.

Zhang, L., Yu, R. & Huang, C., 2011. ARMA prediction model of ground surface movement in mine area. *Journal of China Coal Society.*

Zisk, S., 1972. A new Earth-based radat technique for the measurement of lunar topography. *Moon,* 4(296-300), pp. 296-300.

Appendix A Available Envisat Data Sets

No.	Track	Orbit	Acquisition Date (dd/mm/yy)
1	51	7620	15/08/2003
2	51	8622	24/10/2003
3	51	9123	28/11/2003
4	51	9624	01/02/2004
5	51	11127	16/04/2004
6	51	11628	21/05/2004
7	51	12630	30/07/2004
8	51	13632	08/10/2004
9	51	14133	12/11/2004
10	51	14634	17/12/2004
11	51	15135	21/01/2005
12	51	15636	25/02/2005
13	51	16137	01/04/2005
14	51	16638	06/05/2005
15	51	17139	10/06/2005
16	51	17640	15/07/2005
17	51	18141	19/08/2005
18	51	18642	23/09/2005
19	51	19143	28/10/2005
20	51	19644	02/12/2005
21	51	27159	11/05/2007
22	51	27660	15/06/2007
23	51	28161	20/07/2007
24	51	28662	24/08/2007
25	51	29163	28/09/2007
26	51	29664	02/11/2007

27	51	30165	07/12/2007
28	51	31668	21/03/2008
29	51	32670	30/05/2008
30	51	33171	04/07/2008
31	51	33672	08/08/2008
32	51	34173	12/09/2008
33	51	34674	17/10/2008
34	51	35175	21/11/2008
35	51	35676	16/12/2008
36	51	36177	30/01/2008
37	51	36678	06/03/2009
38	51	37680	15/05/2009
39	51	40185	06/11/2009
40	51	41688	19/02/2010
41	51	42189	26/03/2010
42	51	42690	30/04/2010
43	51	43692	09/07/2010
44	51	44193	13/08/2010
45	51	44694	17/09/2010

Table A. 1: Available Envisat ASAR image mode data sets

Appendix B Deformation Velocities of the PS along HS1

PS No.	Deformation velocity in LOS (mm/y)	Coordinates	
		North (N)	East (E)
M25 QE II Bridge			
1	-3.4	51°28'11.50"N	0°16'21.22"E
2	-1.5	51°28'9.64"N	0°16'25.80"E
Thames Tunnel North Portal			
Thames Tunnel South Portal			
3	-0.2	51°27'7.24"N	0°18'46.35"E
A226 Galley Hill Road			
4	1.4	51°26'58.45"N	0°18'58.03"E
5	-0.5	51°26'56.91"N	0°18'57.56"E
6	1.0	51°26'54.41"N	0°19'1.01"E
North Kent Line Overbridge			
7	1.5	51°26'50.18"N	0°19'4.28"E
Pedestrian Access			
8	0.3	51°26'34.95"N	0°19'15.96"E
9	-0.2	51°26'30.51"N	0°19'18.04"E
10	1.6	51°26'28.94"N	0°19'18.63"E
11	0.5	51°26'24.68"N	0°19'19.31"E
A2260 Lind Road			
12	-2.8	51°25'56.60"N	0°19'29.94"E
Pepper Hill Tunnel (Entrance)			
13	-0.5	51°25'31.59"N	0°19'49.92"E
Pepper Hill Tunnel (Exit)			
14	0.0	51°25'29.17"N	0°19'53.71"E

15	-0.5	51°25'26.64"N	0°19'58.19"E
Southfleet Tunnel (Entrance)			
16	-0.4	51°25'18.12"N	0°20'9.95"E
Southfleet Tunnel (Exit)			
17	-1.1	51°25'9.49"N	0°20'33.51"E
Downs Road Overbridge			
18	-1.6	51°25'7.81"N	0°20'34.98"E
19	0.4	51°25'8.28"N	0°20'38.14"E
20	0.1	51°25'1.07"N	0°21'1.15"E
21	-2.3	51°24'57.85"N	0°21'5.01"E
22	-0.4	51°24'58.03"N	0°21'10.27"E
23	-1.3	51°24'53.67"N	0°21'26.51"E
Wrotham Road Underbridge			
24	0.4	51°24'47.10"N	0°21'50.69"E
Watling Street Footbridge			
25	-4.2	51°24'44.76"N	0°21'59.43"E
26	-0.6	51°24'42.08"N	0°22'4.97"E
27	-2.1	51°24'36.54"N	0°22'23.91"E
Church Road Footbridge			
28	1.1	51°24'29.27"N	0°22'46.37"E
29	0.0	51°24'27.20"N	0°22'57.01"E
30	0.1	51°24'23.68"N	0°23'12.94"E
Henhurst Road Overbridge			
31	-0.7	51°24'13.44"N	0°23'40.20"E
32	-1.4	51°24'11.88"N	0°23'49.05"E
33	0.0	51°24'6.97"N	0°24'11.98"E
Scotland Lane bridge Overline			
34	0.1	51°24'4.81"N	0°24'25.92"E
35	0.7	51°24'3.78"N	0°24'35.82"E
36	-0.5	51°24'3.42"N	0°24'40.18"E
Halfpence Lane Tunnel			

Brewers Road Overbridge			
Park Pale Underbridge			
37	-0.3	51°23'56.81"N	0°26'1.13"E
38	-0.1	51°23'52.03"N	0°26'22.01"E
Knights Place Accomodation Bridge			
39	0.4	51°23'48.13"N	0°26'38.76"E
Knights Place Footbridge			
Temple Wood Lane Bridge			
Great Wood Landridge			
40	-0.7	51°23'4.10"N	0°28'0.18"E
Merral Shaw Pedestrain Subway			
Merral Shaw Underbridge			
A228 Cuxton Road Bridge HS1			
Shakehole Bridge (Intersection Bridge over Network Rail)			
Medway Viaduct			
North Down Way Bridge			
41	-0.6	51°21'48.76"N	0°29'11.48"E
42	-0.6	51°21'46.65"N	0°29'13.08"E
43	-1.5	51°21'26.07"N	0°29'33.55"E
Stoney Lane Bridge			
North Down Tunnel (Entrence)			
44	-2.4	51°20'26.01"N	0°30'7.10"E
45	-1.4	51°20'18.57"N	0°30'8.31"E
46	-3.7	51°20'9.83"N	0°30'25.01"E
47	-2.4	51°20'8.80"N	0°30'21.99"E
48	-2.0	51°20'3.67"N	0°30'16.59"E
49	-2.0	51°20'1.66"N	0°30'23.09"E
50	-4.4	51°19'58.75"N	0°30'20.01"E
51	-3.0	51°19'56.96"N	0°30'20.27"E
52	-2.8	51°19'55.44"N	0°30'25.20"E
53	-1.5	51°19'54.30"N	0°30'20.18"E

54	-1.8	51°19'50.03"N	0°30'27.37"E
55	-1.2	51°19'16.87"N	0°30'22.67"E
56	-1.4	51°19'13.45"N	0°30'25.91"E
North Down Tunnel (Exit)			
57	-0.4	51°18'51.93"N	0°30'49.13"E
Pilgrims Way Bridge			
58	1.0	51°18'51.37"N	0°30'51.17"E
59	-0.5	51°18'49.90"N	0°30'52.07"E
60	-3.3	51°18'46.85"N	0°30'53.59"E
61	0.0	51°18'39.66"N	0°31'2.45"E
Boarley Lane Overbridge			
Boxely Tunnel			
Boxley Valley AccomodationOverbridge			
Workhouse AccomodationOverbridge			
A249 Sittingbourne Road Overbridge			
62	-1.2	51°17'24.36"N	0°33'45.54"E
63	-1.6	51°17'21.42"N	0°33'55.48"E
Hockers Lane Overbridge			
64	-2.7	51°17'3.95"N	0°34'43.17"E
65	-2.5	51°16'58.56"N	0°34'54.30"E
Thurnham Lane Underbridge			
66	-1.4	51°16'58.89"N	0°34'55.72"E
67	-3.2	51°16'39.89"N	0°35'30.91"E
Water Lane Underbridge			
68	3.9	51°16'32.60"N	0°35'43.88"E
69	0.5	51°16'23.77"N	0°35'56.44"E
Longham Wood Underpass			
Crismill Lane Underbridge			
70	-2.2	51°16'13.09"N	0°36'18.89"E
Maidstone Ashford Railway Underbridge			
71	1.2	51°16'4.54"N	0°36'34.96"E

72	-2.6	51°15'59.94"N	0°36'37.96"E
M20 Motorway Service Utilities Underbridge			
M20 Motorway Service Area Overbridge			
73	0.8	51°15'51.03"N	0°36'57.40"E
74	1.0	51°15'49.10"N	0°37'0.56"E
Eyhorne Street Tunnel			
75	-0.3	51°15'27.39"N	0°37'43.03"E
Ash Wood Footbridge			
Hospital Road Overbridge			
A20 Ashford Road Underbridge			
76	-0.5	51°15'3.43"N	0°38'23.44"E
77	1.3	51°14'57.93"N	0°38'38.90"E
Chegworth Lane Underpass			
78	1.1	51°14'49.06"N	0°39'1.68"E
79	-1.5	51°14'42.28"N	0°39'20.20"E
80	-0.5	51°14'37.75"N	0°39'32.77"E
81	0.9	51°14'36.49"N	0°39'38.55"E
82	0.5	51°14'35.19"N	0°39'40.14"E
83	0.6	51°14'33.43"N	0°39'47.48"E
Harrietsham Tunnel			
Fairbourne Lane Overbridge			
84	0.9	51°14'25.34"N	0°40'14.94"E
Bell Farm Access Under bridge			
Runham Lane Overbridge			
Sandway Road Overbridge			
Old Ham Lane Overbridge			
Sandway Tunnel			
Boughton Road Overbridge			
Lenham Heath Road Overbridge			
85	0.6	51°13'26.23"N	0°42'48.23"E
86	-2.1	51°13'10.04"N	0°43'17.63"E

Bowley Lane Overbridge			
87	0.2	51°13'8.32"N	0°43'21.94"E
88	-0.8	51°13'6.33"N	0°43'23.63"E
89	-2.3	51°13'3.38"N	0°43'30.86"E
90	-0.4	51°12'59.95"N	0°43'36.73"E
Hubbards Farm Accomodation Overbridge			
91	-3.5	51°12'46.16"N	0°44'8.98"E
92	0.3	51°12'44.87"N	0°44'11.30"E
93	-0.5	51°12'40.57"N	0°44'22.19"E
94	-2.2	51°12'34.71"N	0°44'36.31"E
95	-2.0	51°12'34.35"N	0°44'38.71"E
Burnt Mills Footbridge			
96	-1.4	51°12'30.48"N	0°44'46.64"E
Egerton Road Overbridge			
97	-0.6	51°12'23.66"N	0°45'5.42"E
98	-2.3	51°12'9.46"N	0°45'34.02"E
99	-0.8	51°12'8.65"N	0°45'41.23"E
Newlands Road Overbridge			
100	-1.9	51°11'49.21"N	0°46'27.92"E
101	0.5	51°11'47.56"N	0°46'34.42"E
Pluckley Road Overbridge			
102	2.4	51°11'40.68"N	0°46'59.87"E
103	-0.1	51°11'39.16"N	0°47'10.15"E
Leacon Lane Underbridge			
Broad Mead Access Bridge Overline			
WestwellLeacon Tunnel			
A20 Maidstone Road West Bridge Overline			
104	-1.3	51°11'25.84"N	0°48'48.48"E
105	0.4	51°11'23.69"N	0°48'56.52"E
M20 Tutt Hill Underbridge			
Westwell Lane Overbridge(Over HS1&Network Rail)			

106	0.1	51°10'58.78"N	0°49'43.49"E
Station Road Underbridge			
107	0.0	51°10'27.18"N	0°50'9.55"E
108	-2.0	51°10'24.38"N	0°50'11.26"E
109	-2.3	51°10'17.60"N	0°50'16.09"E
A20 Maidstone Road East Overbridge			
110	-0.4	51°10'14.19"N	0°50'17.32"E
111	1.1	51° 9'50.85"N	0°50'32.20"E
Godinton Lane Rial Underbridge			
112	1.2	51° 9'41.89"N	0°50'39.00"E
Lodge Wood Foorbridge			
Long Walk Access Road Overbridge			
Ashford International Station (Entrance)			
113	1.7	51° 8'55.61"N	0°51'42.83"E
114	1.9	51° 8'52.86"N	0°51'48.56"E
115	2.2	51° 8'49.95"N	0°51'52.75"E
116	1.4	51° 8'41.64"N	0°52'21.26"E
117	1.6	51° 8'38.84"N	0°52'28.30"E
118	2.2	51° 8'36.89"N	0°52'31.40"E
119	1.8	51° 8'35.45"N	0°52'32.06"E
120	1.2	51° 8'32.51"N	0°52'36.40"E
121	1.8	51° 8'29.07"N	0°52'41.43"E
122	0.9	51° 8'26.87"N	0°52'50.69"E
123	1.9	51° 8'20.30"N	0°52'56.81"E
124	2.4	51° 8'16.80"N	0°53'3.10"E
125	0.8	51° 8'15.15"N	0°53'7.77"E

Table B. 1: Annual average deformation velocities of the PS along HS1

Appendix C MATLAB Script for PS-InSAR Data Processing

1. Data pro-processing

$ cd /media/ HS1/

$ mkdir Envisat

 # Create a folder 'Envisat' for Envisat ASAR data

 # Paste all the Envisat ASAR data to 'Envisat'

$ link_slcs /media/HS1/Envisat

 # Create a folder 'SLC' in '/media/ HS1/'

 # SLC files 'image.slc', which have symbolic links with the Envisat data, are created

$ cd /media/ HS1/SLC/20081226

#In order to minimise spatial baselines, temporal baselines and Doppler centroid frequency difference, data '20081226' are chosen to generate a master image

$ step_read_whole_Envisat

 # Read '20081226' and generate the master image

$ cp $MY_SCR/master_crop.in .

 # Crop the research area by the line and pixel number

$ vi master_crop.in

 # Edit 'master_crop.in' to identify area of interest

 # First_l:7800, last_l:24000, first_p:10 and last_p:2800

$ step_master_read

 # Crop the master image

 # Generate folder'INSAR_20081226'

$ cd /media/ HS1/SLC

$ make_read

 # Crop all SLC images

2. D-InSAR process

```
$ cd /media/HS1/
$ mkdir DEM
  # Create a folder 'DEM' for DEM data
  # Download DEM from SRTM3 for the research area
$ cd /media/HS1/INSAR_20081226
$ vi timing.dorisin
  # Update the following fields based on the downloaded DEM
    The updated information is shown as follows
    ******************************************************************
    SAM_IN_FORMAT   real4
    SAM_IN_DEM      /media/HS1/DEM/HS1/final_HS1.dem
   SAM_IN_SIZE     2401 4801              // rows cols
   SAM_IN_DELTA    0.000833333333333    // in degrees
   SAM_IN_UL       52  -2      // lat and lon of upper left
   SAM_IN_NODATA   -32768
  ********************************************************************
$ step_master_timing
  # Correct DEM offset
$ make_orbits
  # Extract precise orbit data from orbit files
$ make_coarse
  # Coarse coregistration
$ make_coreg
  # Precise coregistration
$make_dems
  # Build topographic phase for each interferogram based on downloaded DEM and
   create the simulated magnitude image of the DEM
$make_resample
  # Resample slave images into master geometry
$make_ifgs
  # Generate a stack of differential interferograms (flat phase and topographic phase
    are removed by orbit files and the simulated magnitude image of the DEM
```

respectively)

$ cd /media/HS1/INSAR_20081226/20081017

 # Choose only one of the slave directories

$ step_geo

 # Calculate the latitude and longitude of each pixel in the interferogram for geocoding

3. PS-InSAR process

$ cd /media/HS1/INSAR_20081226/

$ mt_prep 0.4 3 3 50 200

 # Divide the interferogram into 3 patches in range and 3 patches in azimuth to reduce required data processing memory

 # Amplitude dispersion is 0.4

 # Overlaping pixels between patches in azimuth and range are 200 and 50 (default)

In MATLAB

$ >>cd /media/HS1/INSAR_20081226/

$ >>getparm

 # Check the default values for PS processing

$ >>setparm

 # Modify parameters with the default values

$ >>stamps

 # PS processing (step 1-8) by stamps

 # Step 1: Load input data, such as baselines information, amplitude dispersion, and store the data in workspaces)

 # Step 2: Phase noise estimation for all PSC

 # Step 3: PS selection based on amplitude stability and phase stability

 # Step 4: Drop noisy PS pixels by PS weeding

 # Step 5: Phase correction for spatially-uncorrelated look angle error (DEM error)

 # Step 6: Phase unwrapping

 # Step 7: Estimate spatially-correlated look angle error (atmospheric error and orbit error)

 # Step 8: Estimate other spatially correlated noise and phase filtering

4. PS-InSAR result plotting

$ >>cd /media/HS1/INSAR_20081226/

$ >>help ps_plot

 # View different plotting methods

$ >>plot_all_ifgs

 # Plot all interferograms

$ >>ps_plot ('v',1)

 # Plot mean LOS velocity map

$>>ps_plot (‘v-d’,1)

 # Plot mean LOS velocity map by removing DEM error

$>>ps_plot (‘v-do’,1)

 # Plot mean LOS velocity map by removing DEM error and orbital ramps

$>>ps_plot ('v-do',1,0,0,[],'ts')

 # Plot mean LOS velocity map for PS with time series information

 # A time series analysis result of any PS can be represented by clicking the PS on mean LOS velocity map

5. Visualising PS results on Google Earth

$ >>ps_plot('v-do',-1)

 # Save velocity estimation of PS

$ >>load ps_plot_v-do ph_disp

 # Retrieve velocity estimation of PS as an input to ‘ps_gescatter’

$ >>ps_gescatter('HS1_PS.kml',ph_disp,10,0.4)

 # Generate a kml file for the visualisation on Google Earth

Appendix D R Modules Script for Time Series Prediction

1. Data preparation

```
# Import mat file
library("R.matlab")
library("xlsx")
mat.file <- file.path(getwd(),"Data/ps_plot_ts_v-do.mat")
mat.data <- readMat(mat.file)
# Convert the original phase data to subsidence data
ts.sub <- -mat.data$ph.uw*as.numeric(mat.data$lambda)*1000/(4*pi)
ts.sub <- as.data.frame(ts.sub)
ts.data <- data.frame(mat.data$ref.ps,mat.data$lonlat,ts.sub)
colnames(ts.data) <- c("ref","longitude","latitude",paste("sb_",1:20,sep = ""))
# Import selected PS information
coordinates.file <- file.path(getwd(),"Data/Railway Coordinates.xlsx")
coordinates.data <- read.xlsx(file = coordinates.file,sheetIndex = 1,colIndex = c(1,2,3,4))
colnames(coordinates.data) <- c("no.","annual sb","latitude","longitude")
p.length <- nrow(coordinates.data)
t.length <- nrow(ts.data)
# Obtain subsidence data for the selected PS
target.ref <- vector(length = p.length)
for (x in 1:p.length) {
 target.ref[x] <- ts.data[which((ts.data$latitude=coordinates.data$latitude[x]) & (ts.data$longitude=coordinates.data$longitude[x])),1]
}
coordinates.data <- cbind(coordinates.data,target.ref)
for (y in 1:p.length){
```

```
  if (coordinates.data$target.ref[y] != 0) {
    sb.temp <- ts.data[which(ts.data$ref==coordinates.data$target.ref[y]),4:23]}
  else {sb.temp <- rep(0,20)}
  ifelse(y==1,sb.data <- sb.temp,sb.data <- rbind(sb.data,sb.temp))
}
rownames(sb.data) <- NULL
coordinates.data <- cbind(coordinates.data,sb.data)
# Add the master point data into the data series
ts.interpolation <- rep(0,120)
sb_11.5 <- ts.interpolation
sb_12 <- coordinates.data$sb_12
sb_13 <- coordinates.data$sb_13
ts.valid <-
data.frame(coordinates.data[,1:5],coordinates.data[,11:16],sb_11.5,sb_12,sb_13)
rm(sb_11.5,sb_12,sb_13)
```

2. ARIMA model

```
# Manually select ARIMA model orders
library("forecast")
ts1 <- ts(as.numeric(ts.valid[25,6:14]))
par(mfrow=c(1,2),cex = 0.8)
# Plot ACF and PACF functions
Acf(ts1,main = "")
Pacf(ts1,main = "")
par(mfrow=c(1,1),cex = 0.8)
# Fit data with ARIMA(1,0,0) model
fit1 <- Arima(ts1,c(1,0,0))
plot(fit1$x,col="red",xlab = "Time",ylab = "Subsidence")
lines(fitted(fit1),col="blue")
legend("topright",c("actual","fitted"),col=c("red","black"),lty = c(1,1))
accuracy(fit1)
# Predict the following 2 subsidence data
```

```
forecast(fit1,2)
```

3. Artificial neural network model

```
# Generate lagged time series for modelling
sbs_series <- as.numeric(ts.valid[which(ts.valid[,1]==25),6:14])
len <- length(sbs_series)
twindow <- 3
offsetsbs <- lapply(0:(twindow-1),function(x){
  sbs_series[(twindow-x):(len-x-1)]})
newtm <- Reduce(cbind,offsetsbs)
# Establish and train the neural network model
sample.size <- nrow(newtm)
library("nnet")
nns  <-  nnet(newtm[1:sample.size,],sbs_series[(twindow+1):(length(sbs_series))],size
= 3, maxit = 1000, linout = TRUE)
ts.error <- sbs_series[(twindow+1):(length(sbs_series))]-c(nns$fitted.value)
ts.rmse <- sqrt(sum(ts.error^2)/sample.size)
ts.rmse
# Predict time series
no.of.predict <- 2
predictions <- vector(length = no.of.predict,mode="numeric")
input <- c(sbs_series[length(sbs_series)],newtm[sample.size,1:2])
for (n in 1:no.of.predict){
  predictions[n] <- predict(nns,input)
  input <- c(predictions[n],input[1:(length(input)-1)])}
predictions
```

4. Grey model

```
# Functions used in the module
ago <- function(x){
  len <- length(x)
  x.ago <- vector(length = len)
```

```
  x.ago[1] <- x[1]
  for (n in 2:len){
    x.ago[n] <- x[n] + x.ago[n-1]
  }
  x.ago}
avo <- function(y){
  len <- length(y)
  y.avo <- vector(length=len-1)
  for (n in 2:len){
    y.avo[n-1] <- mean(c(y[n-1],y[n]))
  }
  y.avo}
# Transform the original series to grey series
ts.grey <- ts.valid[which(ts.valid[,1]==25),]
no.of.training <- 9
  sbs_series <- as.numeric(ts.grey[,6:14])
  inputs <- sbs_series[1:no.of.training]
  len.tm <- length(inputs)
  newtm <- ago(inputs)
  z.series <- avo(newtm)
# Solve the grey differential model
  B <- matrix(c(-z.series,rep(1,len.tm-1)),ncol = 2)
  Y <- matrix(inputs[-1])
  a.b <- solve(t(B)%*%B)%*%t(B)%*%Y
  a <- a.b[1,1]
  b<- a.b[2,1]
  newtm.fitted <- vector(length=len.tm)
  newtm.fitted[1]=inputs[1]
  for (i in 2:len.tm){
    newtm.fitted[i] <- (inputs[1]-b/a)*exp(-a*(i-1))*(1-exp(a))
  }
errors <- inputs - newtm.fitted
```

```
rmse <- sqrt(sum((errors)^2)/len.tm)
rmse
```

5. Unequal time series transformation

```
# Obtain the date series for the subsidence data
sub_t <- c(mat.data$day[1:10],mat.data$master.day,mat.data$day[11:19])
# Calculate the average interval for the date series
interval_ave <- (sub_t[length(sub_t)]-sub_t[1])/(length(sub_t)-1)
# Calculate the ratio between the original interval and the average interval
d <- vector(length=length(sub_t)-1)
for (n in 1:(length(sub_t)-1)){
  d[n] <- (n*interval_ave-(sub_t[n+1]-sub_t[1])) / (sub_t[n+1]-sub_t[1])
}
dr <- vector(length=length(sub_t)-1)
for (m in 1:(length(sub_t)-1)){
  dr[m] <- (m*interval_ave-(sub_t[m+1]-sub_t[1])) / interval_ave
}
# Transform the unequal time series into equal interval series
ts.valid <- ts.original[,1:6]
for (k in 1:length(d)){
  ts.temp <- ts.original[,k+6]+d[k]*(ts.original[,k+6]-ts.original[,k+5])
  ts.valid <- data.frame(ts.valid,ts.temp)
  colnames(ts.valid)[k+6] <- paste("sb","_",as.character(k+1),sep = "")
}
```